E.O. Paton Electric Welding Institute of the National Academy of Science of Ukraine
International Association «Welding»

The Paton Welding Journal

10
2022

International Scientific-Technical and Production Journal ◊ Founded in January 2000 (12 Issues Per Year)

Address of Editorial Board
E.O. Paton Electric Welding Institute, 11 Kazymyr Malevych Str. (former Bozhenko), 03150, Kyiv, Ukraine
Tel./Fax: (38044) 205 23 90, E-mail: journal@paton.kiev.ua
https://patonpublishinghouse.com/eng/journals/tpwj

State Registration Certificate 24933-14873 ПР from 13.08.2021
ISSN 0957-798X, DOI: http://dx.doi.org/10.37434/tpwj

Subscriptions, 12 issues per year:
$384 — annual subscription for the printed (hard copy) version, air postage and packaging included;
$312 — annual subscription for the electronic version (sending issues in pdf format or providing access to IP addresses).

Representative Office of «The Paton Welding Journal» in China:
China-Ukraine Institute of Welding, Guangdong Academy of Sciences
Address: Room 210, No. 363 Changxing Road, Tianhe, Guangzhou, 510650, China.
Zhang Yupeng, Tel: +86-20-61086791, E-mail: patonjournal@gwi.gd.cn

The content of the journal includes articles received from authors from around the world in the field of welding, metallurgy, material science and selectively includes translations into English of articles from the following journals, published by PWI in Ukrainian:
- Automatic Welding (https://patonpublishinghouse.com/eng/journals/as);
- Technical Diagnostics & Nondestructive Testing (https://patonpublishinghouse.com/eng/journals/tdnk);
- Electrometallurgy Today (https://patonpublishinghouse.com/eng/journals/sem).

CONTENTS

ORIGINAL ARTICLES

*Translated Article(s) from «Automatic Welding», No. 10, 2022.

**Translated Article(s) from «Electrometallurgy Today», No. 4, 2022.

DOI: https://doi.org/10.37434/tpwj2022.10.01

APPLICATION OF A-TIG WELDING FOR IMPROVING THE TECHNOLOGY OF MANUFACTURING AND REPAIR OF UNITS OF GAS TURBINE ENGINES AND INSTALLATIONS FROM TITANIUM ALLOYS

D.V. Kovalenko, I.V. Kovalenko, B.O. Zaderii, G.V. Zviagintseva

E.O. Paton Electric Welding Institute of the NASU
11 Kazymyr Malevych Str., 03150, Kyiv, Ukraine

ABSTRACT

The advantages of using the technology of A-TIG welding (TIG welding over the layer of activating flux–activator) of structurally complex elements of titanium alloys, including butt and spot overlapped joints of various thicknesses, as well as joints with variable heat removal, are shown. The relationship between the geometry of welds, structure and properties of welded joints produced by TIG and A-TIG welding methods were studied. A-TIG welding technology was tested in industrial conditions during creation and repair of problematic units of aircraft and convertible gas turbine engines. The A-TIG welding method is recommended for industrial implementation when creating welding structures from titanium alloys of a complex geometry.

KEYWORDS: TIG and A-TIG welding, activators, titanium alloys, butt and spot overlapped joints, variable heat removal, weld formation, structure and properties

INTRODUCTION

Improving the quality, reliability and service life of welded structures, reducing weight and costs during their manufacture are constantly the focus of attention in industrial production. The need to solve these issues when creating complex highly-loaded and highly-critical units of aircraft gas turbine engines (GTE) is particularly relevant and even critical. The use of complex alloys and advanced manufacturing technologies does not always allow achieving ever growing requirements and indices. Therefore, the solution of problems is increasingly achieved by improving (with inevitable complication) of the design of GTE units, the creation of which by welding from individual elements in many cases is the most economical and technological way, probably even the only way. An example may be all-welded rotors, impellers, folded blades, etc. In view of the appearance and specifics of the material and designing features of GTE units, the search for technological, less time-consuming, waste-free method of their welding is quite relevant.

The aim of the work is to investigate the capabilities and to develop the technology of A-TIG welding of butt and spot overlapped joints of thin-sheet (thickness $\delta = 1.2–2.0$ mm) VT-20 and OT-4-1 titanium alloys.

This work uses the results of studying the mechanism of welded metal penetration, and progressive approaches towards improvement of the welding technology, based on these results. One of these approaches is the use of A-TIG welding (TIG welding over the activating flux–activator) in manufacturing structures of steels [1–6], nickel [7] and titanium alloys [8–15]. The main positive effects of using activators in A-TIG welding of all the mentioned materials, as compared to the conventional TIG welding, are manifested in an increase in the penetrating capacity of the process (deep penetration), reducing the input energy, decrease in the length of HAZ, as well as the absence of pores in welds (Figures 1 and 2). During A-TIG welding of titanium alloys, this is mainly predetermined by the constriction of the welding arc by the products of thermal dissociation of the melting activator components [8, 10, 11, 15]. At the same time, the kinetics of melting also changes, the width is significantly reduced, the geometry and the shape of the weld penetration is changed. In the case of the constant speed of welding, the use of the activator in A-TIG welding allows 1.5–2.0 times reduction in the value of welding current without changing (with preservation) penetration (Figure 3), and, therefore, overheating of the welded metal, welding voltage and deformations are decreased.

The following variants and benefits of industrial use of the A-TIG welding method in the manufacture of units of gas turbine engines and installations are considered:

a) for butt joints in welding units with uneven heat removal from the place of welding:

- stability of weld formation increases by several times;
- it becomes possible to produce high-quality welds of structures, the thickness of whose joining elements differs by 2–3 times.

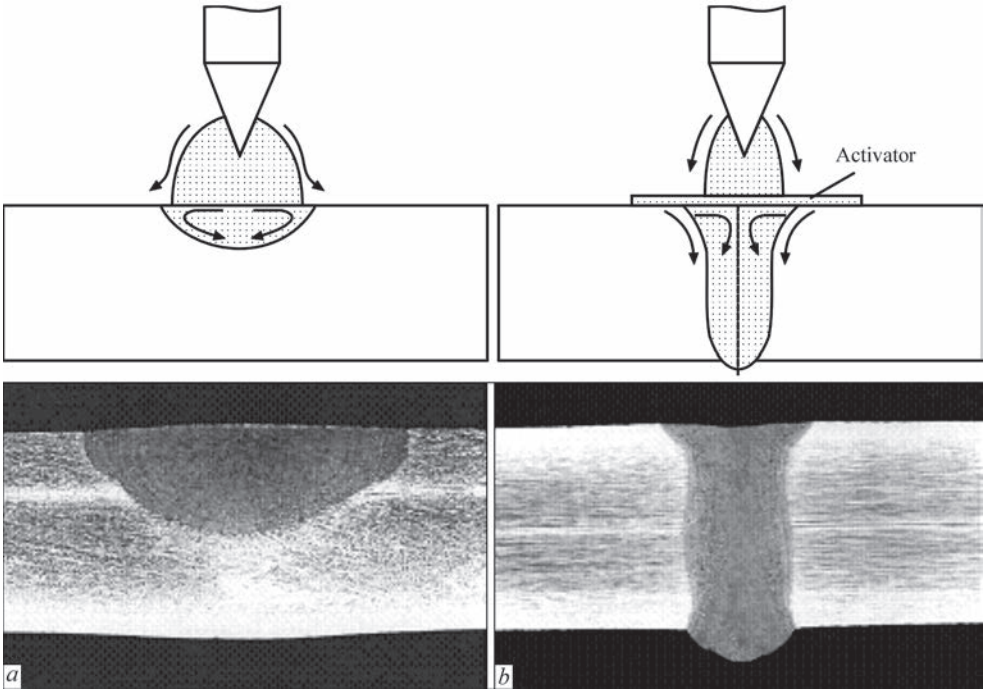

Figure 1. Schematic image and appearance of welds of stainless steel 04Kh18N10T of δ = 6 mm thick, produced by TIG (*a*) and A-TIG (*b*) welding on processes one welding mode: welding current is 200 A; speed of welding is 120 mm/min, arc length is 1.5 mm [1]

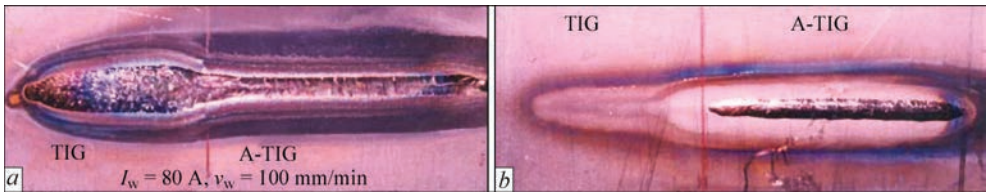

Figure 2. Appearance of welds, produced by TIG (left) and A-TIG (right) welding of VT-20 titanium alloy of δ = 3 mm thick on one welding mode: welding current is 80 A; speed of welding is 100 mm/min: *a* — outer weld surface; *b* — back surface (root) of the weld (results of personal investigations)

b) for overlapped joints:

● drilling of welded elements at the place of joining becomes unnecessary;

● the possibility of producing high-quality welded spots at a gap between the joining elements to 0.5 of the thickness (*H*) of welded metals, and with the use of filler material — to 1.0 N is provided;

A-TIG welding technology can be successfully applied to welding parts of variable cross-section, T- and different thickness joint units. Especially, it is effectively used in welding of high-precision, complex-loaded units and parts of engines and installations from structurally sensitive heat-resistant alloys based on iron, nickel and titanium.

RESEARCH METHODS AND MATERIALS

The main task of the industrial introduction of a new A-TIG welding method consists in adaptation of the proposed methods and realization of their advantages with respect of specific conditions, equipment, units and alloys. The types of welded joints were determined by TS on a product.

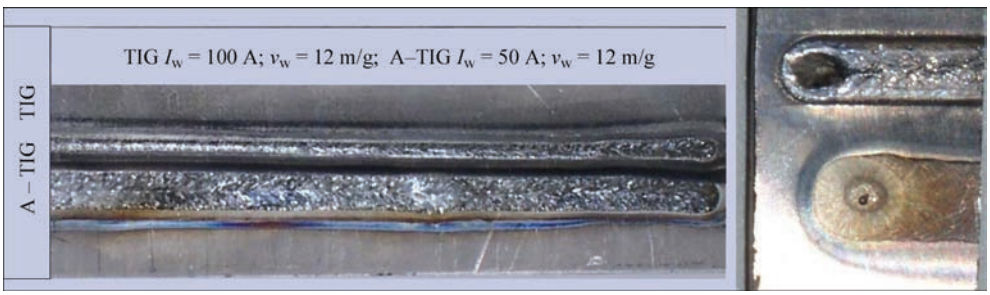

Figure 3. Appearance of weld surface at a full penetration, produced by TIG and A-TIG welding of VT-20 titanium alloy of δ = 2 mm thick at the same speed of welding of 200 mm/min: above — A-TIG, welding current is 50 A; below is TIG weld, welding current is 100 A (results of personal investigations)

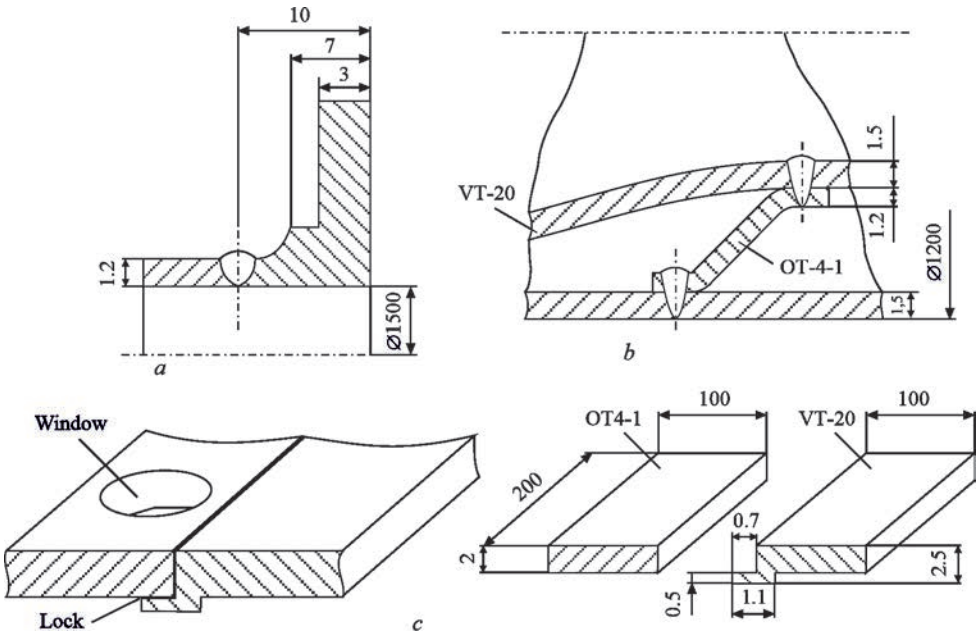

Figure 4. Schemes of fragments of welded units: frame ring-flange (non-symmetric heat removal), butt joint of OT-4 alloy (*a*); frame ring with overlapped spot joints of OT-4 and VT-20 alloys (*b*); frame ring with window, butt lock joint of OT-4 and VT-20 alloys (sketch (left) and elements (right) of welded joint) (*c*)

The structural design represents butt (Figure 4, *a*, *c*) and overlapped spot (Figure 4, *b*) joints. The material is VT-20 and OT-4-1 titanium alloys. The dimensions of units and products are: diameter is 1200–1500 mm, thickness is δ = 1.2; 1.5 and 2.0 mm. Most of the experiments were carried out on flat specimens: butt joints, VT-20 alloy, dimensions of specimens are 150×150×2 mm, 220×80×2 mm and 220×50×1.2 mm; spot overlapped joints, VT-20 and OT-4-1 alloys in a dissimilar combination, dimensions of specimens are 100×60 mm, thickness is 2 + 2 mm, 1.5 + 1.5 mm and 1.5 + 1.2 mm.

Requirements for welds design:

- butt welds: geometry and dimensions of welds are in accordance with GOST 1474–76;
- spot welds: geometry and dimensions of welds are in accordance with GOST 14776–79 (14778–76), diameter of a spot on the facial side of the weld is 6–10 mm, the root is 5–7 mm, the reinforcement (weakening) of the weld is (±0.2 mm).

The mechanical and service characteristics of welded joints should be not lower than 0.9 from the properties of the base metal. The limitations on the deformations of welded joints and stresses in them are specified in the process of mastering edge preparation on specific units, taking into account the existing equipment and a subsequent heat treatment.

The methods, scope and standards of the welds testing are: external inspection is 100 %.

The presence and dimensions of undercuts, cracks on the surface and the presence of splashes are checked. X-ray testing is 100 % of welds. The presence of lacks of penetration, lacks of fusion, cracks, pores and cavities inside the weld is determined.

The preparation, in addition to the fulfillment of the listed technical conditions, had to provide:

- for butt joints: elimination of lacks of fusion, displacement of fusion from the joint; prevention of penetrations caused by nonuniform heat removal; increasing the stability of weld formation;
- for overlapped joints: elimination of the need for drilling before welding; producing high-quality spot joints at increased gaps.

The type of welding equipment, its parameters, welding modes and conditions were selected based on the conditions necessary to obtain high-quality weld formation on the metal of the appropriate thickness and grade, as well as taking into account the equipment and technologies used in production. As a power source for the welding arc, VSVU-315 rectifier was used. Spot overlapped welded joints were produced in the chambers "Atmosfera-6m" and Ob-427 with a controlled shielding atmosphere. The use of such chambers is caused by the need in reliable and stable protection of the welding pool and heat-affected zone from the harmful effect of air, especially in the place where one sheet element overlaps another. Moreover, in such chambers a continuous monitoring of the composition of the shielding atmosphere is possible. The welding of specimens to determine the effect of heat removal was performed in a welding table with a sampling along the joint of 5×10 mm and with clamping of the plates to be welded at a distance of 10 mm from the joint line. For protection against oxidation during welding outside the chamber, inert gas blow-

Table 1. Welding modes and characteristics of butt welds from VT-20 alloy of d = 2 mm thick

Number	Welding method	Welding current I_w, A	Welding speed v_w, mm/min	Weld width B — surface/c — root, mm	Deviation of weld axis from joint line, mm		Deflection along the axis Δ, mm
					Average	Surges*	
1	TIG	85	170	8.0–8.2 4.0–4.8	0.3 0.5	0.6 1.2	12.8
2	A-TIG	80	340	3.4–3.5 2.8–3.4	0.3 0.4	0.4 0.8	7.1

ing was used, through sampling in the table from the root part and "boots" of 50 mm long and 20 mm wide from the weld surface. For welding, the following were used: a standard TIG welding torch with a nozzle of 16 mm diameter, the consumption of shielding gas (argon) in the nozzle — 7–8 l/min, in the "boot" — 4–5 l/min, for blowing 5–6 l/min; welding electrode with a diameter of 2.1 mm of WT20 grade (made of W — 2 % ThO_2 alloy). To carry out welding experiments, oxygen-free halide activator PATIG-T was used. The welding modes (Table 1) were selected based on the need to provide a stable, high-quality penetration of the specimens to be welded.

The activator in the form of a paste was applied with a brush in a thin, uniform layer on the facial surface of a part to be welded. Its width was 8–10 mm on each side from the welded joint or on a diameter of ≈20 mm at the place of making spot in the case of overlapped joining. The thickness of the activator layer was determined based on the need of obtaining the required penetration depth and process stability. At the same time, it was taken into account that for certain ranges of welding current values, there is an optimal thickness of the activator layer, at which the maximum penetration depth with high-quality weld formation is achieved. An excessive thickness of the activator layer, especially at the butt joints, leads to undesirable results — violation of process stability, slagging of the tungsten electrode.

As was already mentioned, in production conditions welded joints of poor quality are often produced as far as it is necessary to change heat input and heat removal along the joint length due to wear of technological assembly and welding equipment, unsuccessful structure of a welded joint, inaccurate manufacture of units to be welded, inaccurate guiding of the arc along the joint, etc. Taking into account the fact that the presence of an activator changes the nature of heat input and penetration of the metal to be welded, which, as a result, stabilizes the process of weld formation, the experiments were conducted to determine the influence of using activators on reduction of the abovementioned negative factors.

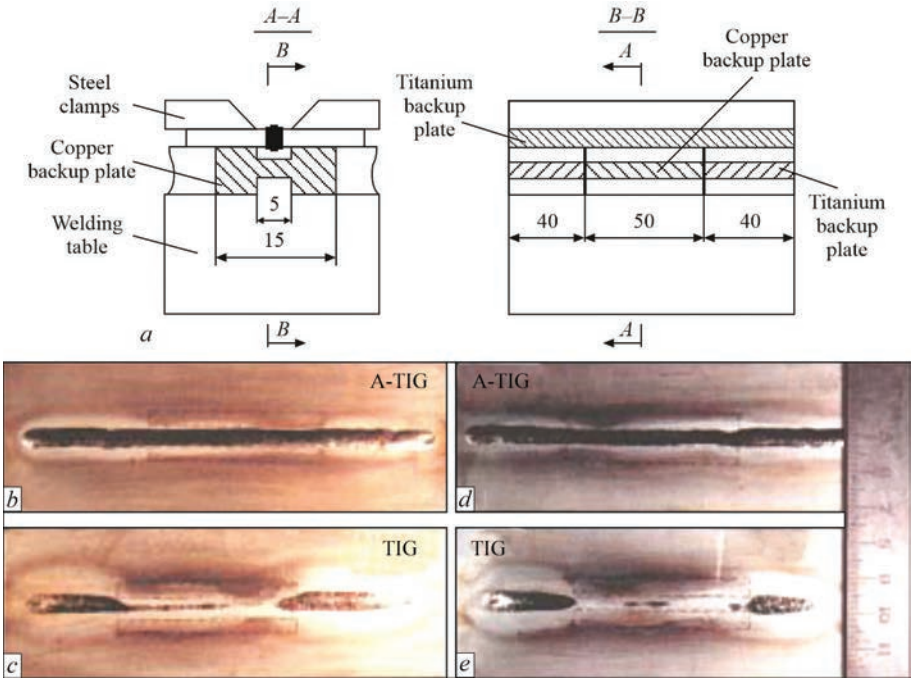

Figure 5. Scheme of assembly (*a*) and outer appearances of specimens after welding of VT-20 alloy of δ = 2 mm thick at a full penetration on the side of the weld root with heat removal, which changes along the length of the specimen: A-TIG welding (*b*, *d*); TIG welding (*c*, *d*); with lower heat removal (*b*, *c*); with greater heat removal (*d*, *e*). The dotted line in Figure 5, *b*–*e* marks the location of copper backup plate

Table 2. Welding modes and results of the stability of weld formation of butt joints from VT-20 alloy of δ = 2 mm thick at a variable heat removal (see Figure 5)

Specimen number	Welding conditions	Arc voltage U_a, V	I_w, A	v_w, mm/min	Weld width, mm surface/root	Changing the weld width surface/root	Note
TIG welding							
1–1	Without heat removal	8.2–8.4	65	100	9.0–8.6 / 5.3–5.7	–	–
1–2	Ti–Cu–Ti with heat removal, distance — 2 mm	–»–	–»–		7.8–7.2 / 0–1.2	1.2–1.4 / 5.3–4.5	Figure 5, *e*
1–3	Ti–Cu–Ti with heat removal, distance — 3 mm	–»–	–»–		7.5–7.6 / 0–1.3	1.5–1.0 / 5.3–4.4	Figure 5, *c*
A-TIG welding							
2–1	Without heat removal	8.2–8.4	40	100	2.8 / 5.5–5.4	–	–
2–2	Ti–Cu–Ti with heat removal, distance — 2 mm	–»–	–»–		2.6 / 5.0–4.9	0.2 / 0.5	Figure 5, *d*
2–3	Ti–Cu–Ti with heat removal, distance — 3 mm	–»–	–»–		2.6 / 5.1	0.2 / 0.4–0.3	Figure 5, *b*

A variable heat removal was created by using assembly backup plates along the length of the specimen, having strongly different thermal conductivity and heat capacity of the materials: titanium-copper-titanium (Figure 5, *a*). The welding modes and conditions were chosen similarly to those described earlier. The speed of welding was slightly reduced (to 100 mm/min), and the current was increased (up to 65 and 45 A in welding at different heat removal) to enhance the impact of heat removal. In addition, to change the conditions of heat removal, heat removing tacks were placed at different (2 and 3 mm) distance from the weld axis. Welding modes and research results are summarized in Table 2 and Figure 5.

In production conditions, when assembling overlapped joints of frame rings of large diameters, often gaps appear between them, which leads to considerable difficulties in producing high-quality joints. Moreover, to carry out the fusion according to the technological process, the upper sheet is drilled, and then the gap is filled by TIG welding in the chamber, which significantly increases the labor, metal and energy consumption of production.

Considering a significant increase in the penetrating capacity of the arc and reducing the overheating of welded metal during A-TIG welding, the experiments were conducted to find out the possibility of eliminating the mentioned difficulties and drawbacks. The main studies were performed in the the plates from VT-20 alloy with 2 mm thickness, as well as of OT-4 alloy with 1 mm thickness, overlapped each other. The testing experiments were performed on the

Table 3. Welding modes and results of studying during welding of specimen-imitator – frame ring with windows from VT-20 alloy of δ = 2 mm thick (see Figure 6)

Specimen number	Welding conditions Type of joint	U_a, V	I_w, A	v_w, mm/min	Weld width, mm surface/root	Note
TIG welding						
1	Plate, 2 welds nearby	8	100	200	7.5–7.9 / 3.2–4.6	Figure 3 below
		A-TIG welding				
2		10.5	50	200	2.2–3.2 / 2.4–3.2	Figure 3 above
A-TIG welding						
1	Butt with a “window”	10.5	60	200	3.5–3.6 / 4.3–4.7	Figure 6, *d*
		A-TIG welding				
2		10.5	50	200	3.6–3.7 / 4.0–4.1	Figure 7, *b*
TIG welding						
1	Butt with a “window”	8	100	200	7.6 / 3.8	Figures 6, *b*,7, *a*
		TIG welding				
2		8	110	12	8.5 / 6.0	Figure 6, *c*

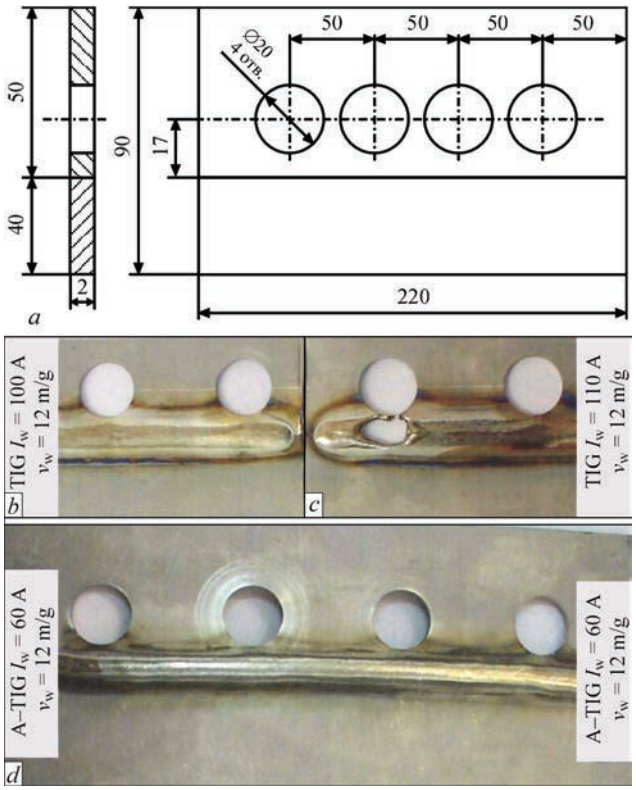

Figure 6. Appearance of fragments of welded specimens-imitators from VT-20 alloy of δ = 2 mm thick at a full penetration: scheme of preparation of specimen-imitator (*a*); TIG welding, welding current is 100 A (*b*) and 110 A (*c*); A-TIG welding, welding current is 60 A (*d*)

specimens that simulate real welded joints: the plate from VT-20 alloy of 1.5 mm thickness overlapped the plate of OT-4-1 alloy of 1.2 mm thickness and vice versa. The gaps between the plates were set by foil strips of 0.2; 0,5; 0.8 and 1 mm thickness between the plates. The specimens were assembled by tacks on the corners of the plates. The current and time of welding were selected from the condition of obtaining a full penetration of the lower sheet with the minimum possible diameter of the spot and upsetting of the metal. Other welding conditions are the same as while producing butt joints.

RESEARCH RESULTS

Analysis of the obtained results allows making a conclusion that in general when applying A-TIG welding of butt joints:

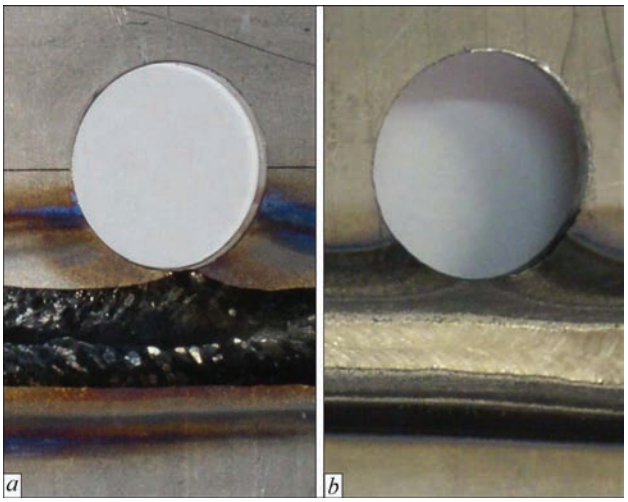

Figure 7. Appearance of fragments of welded specimens-imitators from VT-20 alloy of δ = 2 mm thick at a full penetration: *a* — TIG welding, welding current is 100 A; *b* — A-TIG welding, welding current is 50 A

- the width of the weld is reduced by 2–3 times at a simultaneous decrease in welding current by 30–50 %;
- the impact of heat removal is reduced judging from the width of the weld from its surface by 5–7 times, and by 9–12 times from the root of the weld.

The similar results were obtained in welding of butt joints of the specimen-imitator (δ = 2 mm thick) from VT-20 alloy — the frame rings with windows. Welding modes and research results are summarized in Table 3 and in Figures 6, 7. Application of A-TIG welding allows avoiding partial melting of metal at the window place.

Analysis of the results of metalographic examinations shows that the positive effect of the activator is manifested in reduction of the weld width, a significant reduction in HAZ (Figure 8), as well as in refinement of both primary β-grains and α- and α′-plates (Figure 9).

The positive effect of using the activator in A-TIG welding of butt joints when changing the heat removal along the length of the specimen is clearly seen as compared to Figure 5, *b*, *d* and 5, *c*, *e*. A-TIG weld is stable across the width along the entire length of the specimen, and in TIG of the weld, penetration in the place of the backup plate disappears.

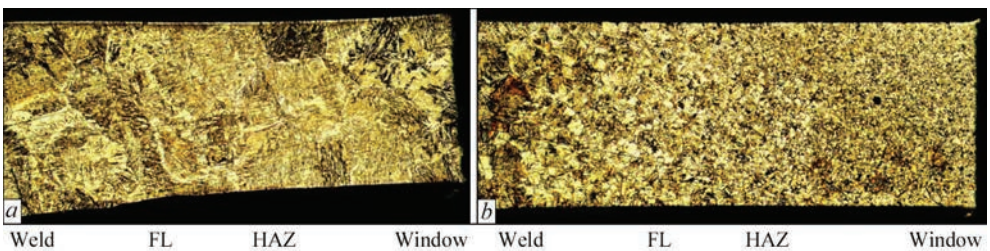

Figure 8. Macrostructure (×25) of welded joints of VT-20 titanium alloy: *a* — TIG welding; *b* — A-TIG welding, FL — fusion line, HAZ — heat-affected zone

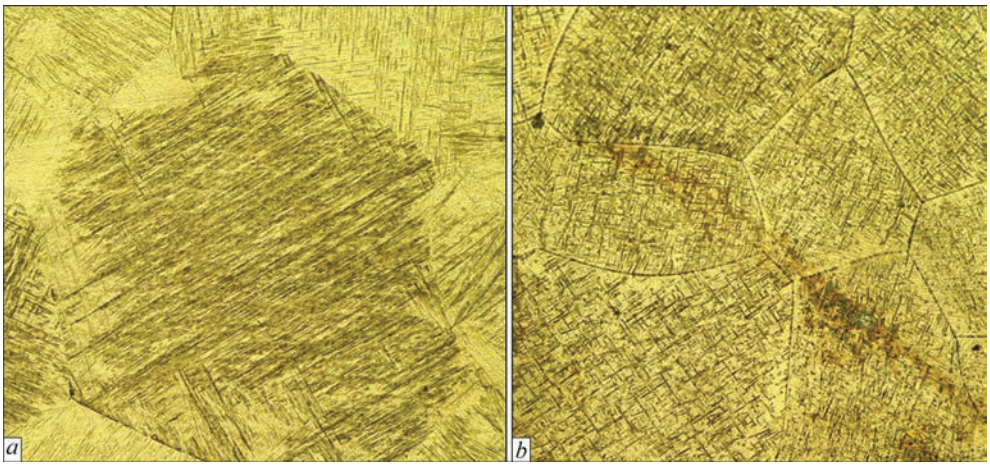

Figure 9. Microstructure (×100) of weld metal (VT-20 alloy): *a* — TIG weld; *b* — A-TIG weld

From the results of the experiments presented in Tables 4, 5, it is seen, that even during assembly, overlapped joints can not be produced without a gap if a welded spot activator with the penetration of the lower sheet is not used — spots of a large diameter without through penetration are formed. A significant increase in the current or time of welding leads to an excessive increase in the diameter of the spot and the burnthrough of both sheets.

The use of A-TIG welding at lower current values allows producing a through penetration at small (within TS) diameters of spots (Tables 4, 5; Figures 10–12) and while complying with all the requirements to similar joints. An increase in the gap causes the need to

Table 4. Welding modes and characteristics of spot overlapped welds on specimens from VT20 (δ = 2 + 2 mm) and OT-4 (δ = 1 + 1 mm), without a gap

Specimen number	Welding conditions	I_w, A	Time of welding t_w, s	Spot diameter, surface/root, mm	Note
1-0	VT20 (2+2 mm) A-TIG welding	80	10	5.0/8.5	Weakening of the weld 0.1 mm
			5	5.0/5.0	Weakening of the weld 0.2 mm
2-0	OT-4 (1+1 mm) TIG welding	40	10	5.5/0	Lack of penetration, weld reinforcement 0.2 mm
			5	5.0/0	Lack of penetration, weld reinforcement 0.1 mm
	A-TIG welding		10	6.0/6.5	Weakening of the weld 0.2 mm
			5	3.6/2.5	Weakening of the weld 0.1 mm

Table 5. Welding modes and characteristics of spot overlapped welds on specimens from VT20, δ = 1.5 mm + OT-4-1, δ = 1.2 mm with different gaps

Specimen number	Welding conditions (gap between the plates to be welded, mm)	I_w, A	t_w, s	Spot diameter, surface/root, mm	Note
TIG welding					
1–1	Without a gap	50	4	7.5/0	Lack of penetration
1–2		50	10	11/0	
1–3		75	5	9.5/0	
A-TIG welding					
1–4	Without a gap	40	4	4.1/2.6	–
1–5		50	4	4.1/6.0	Weakening, 0.2 mm
TIG welding					
2–1	0.25	70	4	12.0/0	Lack of penetration
A-TIG welding					
2–2	0.25	50	3	4.0/5.2	–
3–1	0.5	45	6	5.8/5.8	Weakening, 0.3 mm
3–2		60	6	8.2/6.2	Weakening, 0.4 mm
4–1	1.0	50	4	7.5/0	Lack of penetration
4–2		60	5	6.0/4.7	Weakening, 0.8 mm
4–3		60	6	8.0/8.5	Weakening, 0.1 mm

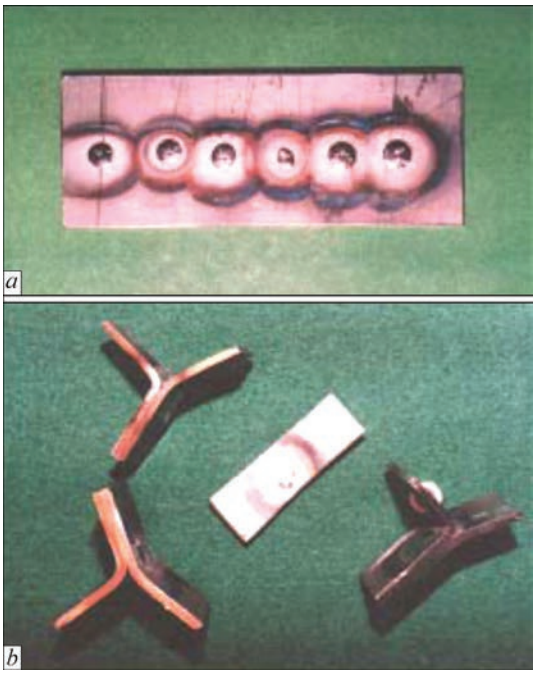

Figure 10. Appearance of spot overlapped welded joints from VT-20 alloy of δ = 2 + 2 mm thick: back side of the joint (weld root) (*a*); specimens after bending test (*b*)

increase current and welding time, use filler material, since at the gaps more than 0.5 mm, weakening of the weld exceeds the admissible (0.2–0.3 mm) values. It

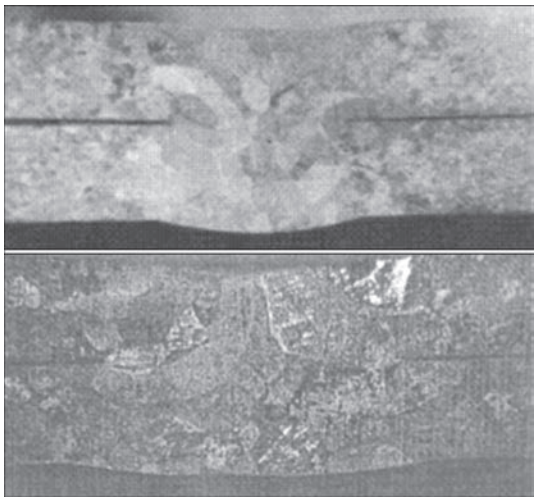

Figure 11. Macrostructures of cross-sections of spot overlapped welded joints from VT-20 alloy of δ = 2 + 2 mm thick, produced by A-TIG welding without a gap

should be noted that a significant increase in welding current leads to an excessive increase in the diameter and to the weakening of the weld in its root part, and an increase in welding time leads to the corresponding change in the facial part of the weld (Figure 12).

The mechanical properties of the butt joints were evaluated by the toughness, since this characteristic is more sensitive to technological and other factors

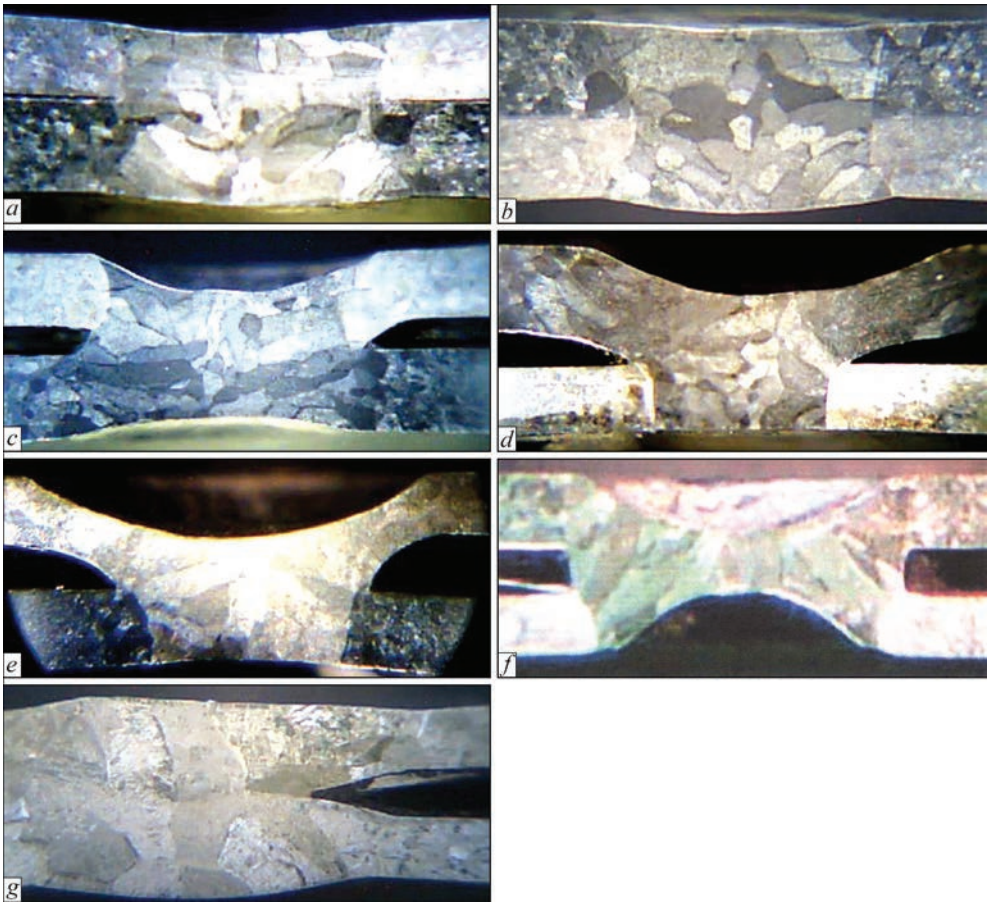

Figure 12. Macrostructures of cross-sections of spot overlapped welded joints of OT-4 and VT-20 alloys, produced by A-TIG welding: without a gap (*a, b*); gap is 0.5 mm (*c, d*); gap is 1.2 mm (*e, f, g*); above is OT-4 alloy, δ = 1.2 mm (*a, c, d*); above is VT-20 alloy, δ = 1.5 mm (*b, d, f*); OT-4 alloy, δ = 1.2 mm (with filler) (*g*)

Table 6. Mechanical properties of butt welded joints from VT-20 alloy (δ = 2 mm)

Number	Area of welded joint	Impact toughness, J/cm^2	Discrepancy of values, %
1	Base metal	54.0–59.5/57.2	10
TIG welding			
2	HAZ	68.7–77.4/72.7	12.5
	FL – Weld	62.9–71.3/66.75	13.5
	Weld	69.9–87.5/78.5	25.0
A-TIG welding			
3	FL – Weld	57.9–63.3/61.0	9.2
	Weld	68.9–73.4/71.0	6.5

Table 7. Properties of spot overlapped welded joints from VT-20 alloy (δ = 2 + 2 mm), produced by A-TIG welding

Number	Assembly quality	Fracture force *P*, kgf	Shear strength τ_{av}^{*}, MPa	Diameter of welded spot in the place of fracture, mm	Angle of bending (tests on impact bending), deg
1	Without a gap	1022.0	507	4.6	85
		1133.2	602	5.2	96
2	Gap is 1 mm	17289	467	6.8	98
		1558.6	541	5.9	95

*The expression is conditional, during fracture a tear-out of spot occurs, not a shear.

and more demonstrative than, let us say, the tensile strength. The flat specimens of type MI-49 GOST 9454–78 of 2 mm thickness with a round notch, made in different areas of the welded joint were tested.

From the results presented in Table 6, it can be concluded that the use of activators in most cases slightly changes the properties of the welded metal.

It should be noted that additional low-temperature annealing (650 °C, 30 min) leads to equalization of properties to the values of the base metal.

The properties of the spot overlappled welded joints were evaluated both by the results of the shear tests of the specimens MI-25 (2 + 2 mm) of type XX according to GOST 6996–66 and technological test on impact bending. The test results are presented in Table 7. The fracture occurs on the base metal (in some cases — across HAZ) at the values of loading and bending angles larger than those caused by TS on products and specified by GOST.

CONCLUSIONS

1. The positive effect of using A-TIG welding of thin-sheet (1–2 mm) titanium alloys consists in reducing dimensions of the weld and HAZ, lower overheating of welded metal and, as a consequence, some decrease in welding stresses and strains, reduction in sensitivity to nonuniform heat removal from the welding zone and different thickness of elements to be welded.

2. Applying A-TIG welding method to produce spot overlapped joints allows providing high-quality joints without drilling the upper element of the welded joint at reduced welding currents, and using TIG welding, such joints can not be produced. In addition, performing A-TIG welding, it becomes possible to produce joints with violations of assembly, i.e. with gaps between the sheets to be welded, which can reach the thickness of the upper element.

3.The results of the perfromed studies allow recommending the A-TIG welding method using the proposed PATIG-T activator in creating complex geometry structures of titanium alloys of small thicknesses.

REFERENCES

1. Yushchenko, K.A., Kovalenko, D.V., Kovalenko, I.V. (2001) Application of activators for TIG welding of steels and alloys. *The Paton Welding J.*, **7**, 37–43.
2. Lucas, W., Howse, D. (1996) Activating flux — increase the performance and productivity of the TIG and plasma processes. *Welding and Metal Fabrication*, **1**, 11–17.
3. Lucas, W. (2000) Activating flux — improving the performance of the TIG process. *Welding and Metal Fabrication*, **2**, 7–10.
4. Dong, C., Katayama, S. (2004) B*asic understanding of A-TIG welding process*. IIW Doc. 1802–04/Doc. 212-1055–04.
5. Paton, B.E., Yushchenko, K.A., Kovalenko, D.V. et al. (2006) *Factors of increased penetrating capacity of A-TIG welding of stainless steel*. IIW Doc. XII-1911–06, 17–29.
6. Yushchenko, K.A., Kovalenko, D.V., Krivtsun, I.V. et al. (2008) *Experimental studies and mathematical modelling of metal penetration in TIG and A-TIG stationary arc welding*. IIW Doc. 212-1117–08.
7. Yushchenko, K.A., Kovalenko, I.V. Kovalenko, D.V. et al. (2000) A-TIG welding of nickel alloy NIMONIC-75. *Svarshchik*, 14(**4**), 26–27 [in Russian].
8. Gurevich, S.M., Zamkov, V.N., Blashchuk, V.E. et al. (1986) *Metallurgy and technology of welding of titanium and its alloys*. Kyiv, Naukova Dumka [in Russian].
9. Perry, N., Marya, S., Soutif, E. (1999) New perspectives of flux assisted GTA welding in titanium structures. *Reactive Metals in Corrosive Applications Conference Proceedings, Jack Tosdale*, Editor, Wah Chang, 55–62.
10. Paton, B.E., Zamkov, V.N., Prilutsky, V.P. et al. (2000) Contraction of the welding arc caused by the flux in tungsten-electrode argon-arc welding. *The Paton Welding J.*, **1**, 1–8.

11. Zamkov, V.N., Prilutsky, V.P. (2004) Theory and practice of TIG-F (A-TIG) welding (Review). *The Paton Welding J.*, **9**, 11–14.
12. Sun, Z., Pan, D. (2004) Welding of titanium alloys with activating flux. *Sci. and Techn. of Welding and Joining*, 9(**4**), 337–344.
13. Leconte, S., Pillard, P., Chaelle, P. et al. (2007) Effect of flux containing fluorides on TIG welding process. *Sci. and Techn. of Welding and Joining*, 12(**2**), 120–126.
14. Niagaj, J. (2012) Perculiarities of A-TIG welding of titanium and its alloys. *Archives of Metallurgy and Materials*, 57(**1**), 39–44.
15. Prilutsky, V.P., Akhonin, S.V. (2014) TIG welding of titanium alloys using fluxes. *Welding in the World*, **58**, 245–251.

ORCID
D.V. Kovalenko: 0000-0002-8544-588X,
B.O. Zaderii: 0000-0001-6695-6986

CONFLICT OF INTEREST
The Authors declare no conflict of interest

CORRESPONDING AUTHOR
D.V. Kovalenko
E.O. Paton Electric Welding Institute of the NASU
11 Kazymyr Malevych Str., 03150, Kyiv, Ukraine.
E-mail: d_v_kovalenko@ukr.net

SUGGESTED CITATION
D.V. Kovalenko, I.V. Kovalenko, B.O. Zaderii, G.V. Zviagintseva (2022) Application of A-TIG welding for improving the technology of manufacturing and repair of units of gas turbine engines and installations from titanium alloys. *The Paton Welding J.*, **10**, 3–12.

JOURNAL HOME PAGE
https://pwj.com.ua/en

Received: 29.07.2022
Accepted: 01.12.2022

DOI: https://doi.org/10.37434/tpwj2022.10.02

EFFECT OF EXTERNAL ELECTROMAGNETIC FIELD CONFIGURATION ON METAL STRUCTURE OF WELDED JOINTS OF STRUCTURAL STEEL

O.D. Razmyshlyaev[1], **S.Yu. Maksymov**[2], **O.M. Berdnikova**[2], **O.O. Prylypko**[2], **O.S. Kushnaryova**[2], **T.O. Alekseyenko**[2]

[1]Pryazovskyi State Technical University
7 Universytetska Str., 87500, Mariupol, Ukraine
[2]E.O. Paton Electric Welding Institute of the NASU
11 Kazymyr Malevych Str., 03150, Kyiv, Ukraine

ABSTRACT

The peculiarities of metal structure of welded joints of structural low-alloy steel after welding using external electromagnetic field were studied. The phase composition, microstructure and microhardness of metal of welded joints produced without and with the use of alternating magnetic fields — longitudinal or transverse were studied. The structural parameters in the metal of the welds and areas of the heat-affected zone were analyzed. The conditions for producing high-quality welded joints during welding of low-alloy steels under the effect of external electromagnetic field, which provide strengthening and crack resistance of the metal, were found.

KEYWORDS: structural low-alloy steel, welded joints, external electromagnetic effect, alternating magnetic fields, heat-affected zone, phase composition, microstructure, microhardness

INTRODUCTION

Requirements to quality and reliability of welded joints are growing continuously. The need to expand the range of steels at welding led to development of the scientific direction of application of the external electromagnetic effect (EEE) on the weld pool melt for intensification of the processes of its degassing, lowering of hydrogen content, structure refining, improvement of the value of weld strength and ductility. Experimental studies allowed demonstrating the validity of theoretical conclusions on EEF effectiveness for lowering the weld metal proneness to pore formation, and the degassing mechanism formed under EEE impact, promotes reaching a high degree of homogeneity of fine porosity. In order to define it more precisely, it is necessary to determine the nature of distribution of the electric current lines in the weld pool, taking into account the conditions of welding. On this base it becomes possible to establish the optimum EEE parameters and to perform inductor calculations. The latter had to be made so as to generate magnetic induction exactly in the active part of the weld pool, i.e. in the region of an effective interaction of electric current and external electromagnetic field that causes melt displacement [1–3].

Solving the urgent problem of improvement of the effectiveness of consumable electrode arc surfacing and welding with the action of controlling magnetic fields, will allow increasing the productivity of the process of electrode wire melting, effectiveness of controlling the depth and width of the deposited beads, effectiveness of stirring of the weld pool liquid metal.

In arc welding longitudinal magnetic (LMF) and transverse magnetic (TMF) fields are used. In the first the induction vector is parallel, and in the second it is normal to the electrode and arc axis [3, 4].

Calculations were used to determine the values of the speed and acceleration reached by the liquid metal under the impact of alternating EEE, as well as optimum values of LMF and TMF induction and frequency that ensure effective stirring of the melt along the entire length of the pool at arc surfacing [5–10]. However, nothing is known about the influence of LMF and TMF on the structure which forms in the metal of the welds and in the HAZ.

The objective of this work is establishing the regularities of the influence of alternating EEE (LMF, TMF) on the structure and phase composition, microhardness and microstructure of welded joints of low-alloy structural 09G2S steel.

MATERIAL AND PROCEDURES

As a result of welding structural low-alloy 09G2S steel (14 mm thick) by Sv-08A filler wire (3 mm diameter) (AN-348 flux) welded joints were obtained with and without EEE application in the following modes: current I = 360 A; arc voltage U = 30–32 V; welding speed v = 30 m/h, reverse polarity, using flux-copper backing. Joint type was S4 (GOST 8713–78).

Table 1. Width (μm) of welded joint HAZ sections

HAZ subzones	Welded joints		
	Without EEE	LMF	TMF
I	1000–1600	1000–1600	1600–2200
II	1000	1200	1600
III	600	1000	1400
IV	600	800	1000

EEE was created by an inductor placed on the holder of the mechanism feeding the flux-cored wire, coaxially with it. Powered by alternating current of industrial frequency, the inductor generated an alternating magnetic field which permeated the liquid metal weld pool. Magnetic induction in the zone of the weld pool was equal to 20–25 mT. Three variants of welded joints were produced: without EEE application; with application of LMF (f = 2 Hz) and TMF (f = 6 Hz).

Microstructural studies were performed by light microscopy methods (Neophot-32 and Versamet-2 microscopes, Japan). Vickers hardness was measured in M-400 hardness meter (Leco Company, USA) at 0.1 kg load.

RESULTS AND THEIR DISCUSSION

In welded joints base metal (BM), weld metal, fusion line (FL), and HAZ were studied in the following regions: I — overheated (coarse grain); II — normalized (total recrystallization); III — incomplete recrystallization; IV — recrystallized. Structures of ferrite F, pearlite P, grain size D_{gr}, crystallite width h_{cr}, ferrite interlayer thickness δ(F) and *HV* microhardness were studied.

It was found that LMF and TMF affect the size of HAZ zones (Table 1). In the studied welded joints at EEE application the width of HAZ subzones becomes larger (Table 1) that is associated with the nature of liquid metal movement in the weld pool under EEE impact and features of metal heating and cooling.

Structure of 09G2S steel BM is ferritic-pearlitic at D_{gr} (F) = 10–20 μm, D_{gr} (P) = 40–80 μm and *HV* = = 1650–1760 (Figure 1, *a*). Structure of weld metal in all the joints is also ferritic-pearlitic (F–P) (Figure 1, *b–d*).

In the center of the metal of the weld without EEE the size (width) of pearlite crystallites is equal to h_{cr} (P) = 140–340 μm (Figure 1, *b*) at *HV* (P) = 2060 MPa, and the width of ferrite grain is h_{cr} (F) = 40–100 μm and *HV*(F) = 1810–1870 MPa. In the weld root h_{cr} (P) and h_{cr} (F) are equal to 60–100 μm. On FL, similar to the weld root, a slight lowering of microhardness was achieved, compared to the weld center — by 130 and 110–170 MPa, respectively.

Studies of the sample with LMF application showed that the width of F–P crystallites in the weld metal structure is equal to: h_{cr} (P) = 100–160 μm (Figure 1, *c*) at *HV*(P) = 1990–2080 MPa; h_{cr} (F) = 40–100 μm at *HV* (F) = 1760–1930 MPa. In the weld = root h_{cr} (P) = 60–140 μm and h_{cr} (F) = 20–40 μm. On FL h_{cr} (P) = 60–140 μm and h_{cr} (F) = 20–40 μm with a slight increase of microhardness, compared with the weld center: *HV*(P) = 1990–2280 MPa, *HV*(F) = = 1680–1990 MPa. Note that in the welded joint with LMF application in FL zone, i.e. at transition from the weld metal to HAZ I, a large cold crack of 1600 μm length formed (Figure 1, *e*).

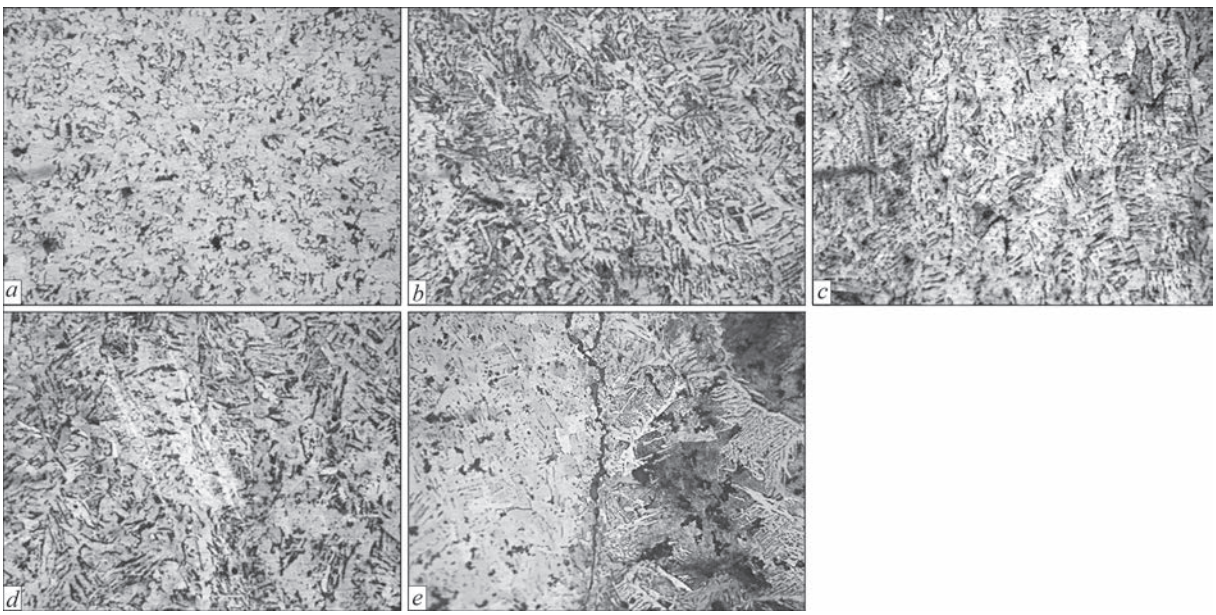

Figure 1. Microstructure (×250) of welded joints of 09G2S steel: *a* — BM; *b–d* — weld metal; *e* — FL, produced without EEE (*b*), with application of LMF (*c*, *e*) and TMF (*d*)

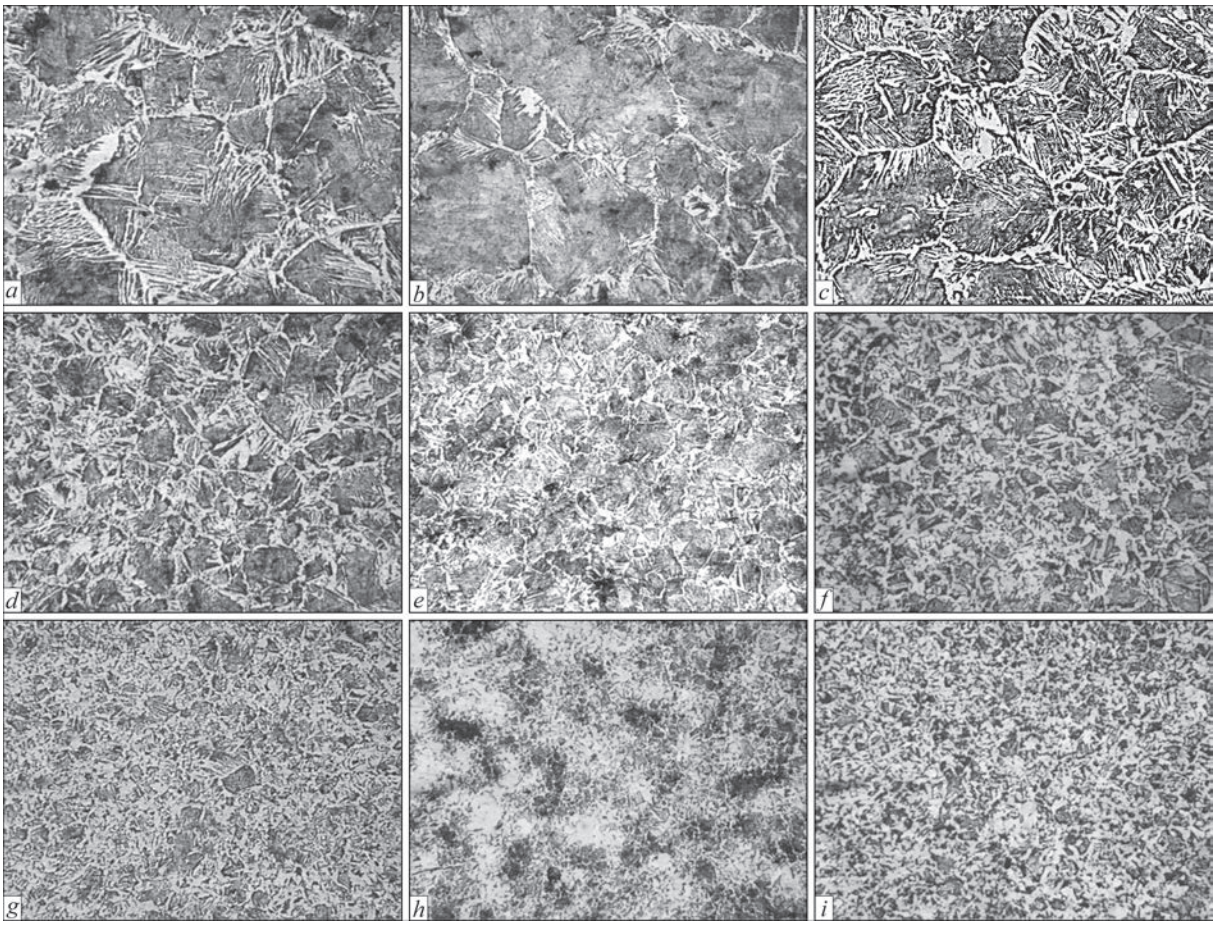

Figure 2. Microstructure (×250) of HAZ metal of 09G2S steel welded joints in subzones: *a–c* — HAZ I; *d–f* — HAZ II; *g–i* — HAZ III, IV obtained without EEE (*a*, *d*, *g*) with application of LMF (*b*, *e*, *h*) and TMF (*c*, *f*, *i*)

Investigations of a sample with TMF application revealed that the width of the crystallites in the weld metal h_{cr} (P) = 100–200 μm (Figure 1, *d*) at *HV* (P) = = 1930 MPa, and the width of ferrite grains — h_{cr} (F) = 20–60 μm at *HV*(F) = 1600–1760 MPa. In the weld root and on FL grain size h_{cr} (P) = 60–220 μm and h_{cr}(F) = 40–140 μm at *HV*(P) = 1930–2060 MPa, *HV*(F) = 1600–1760 MPa.

Investigations of the HAZ metal of welded joints (Figure 2) showed in HAZ I of a sample without EEE a pearlite structure with size D_{gr} (P) = 100–360 μm and interlayers of ferrite δ(F) = 30–70 μm at *HV* (P) = 2130–2210 MPa (Figure 2, *a*), *HV* (F) = 1810–1990 MPa. In HAZ II the structure is refined to D_{gr} (F–P) = 30–80 μm, microhardness is practically unchanged (*HV* (P) = 2060 MPa; *HV* (F) = 1870–1930 MPa) (Figure 2, *d*). In HAZ III, IV D_{gr} (F–P) = 10–50 μm at *HV* (F–P) = = 1810–1930 MPa (Figure 2, *g*).

Investigations of a sample with LMF application revealed formation in HAZ I of P-structure with size D_{gr} (P) = 140–340 μm and interlayers of ferrite δ(F) = = 20–100 μm at *HV* (P) = 2130–2210 MPa (Figure 2, *b*), *HV* (F) = 2060 MPa. In HAZ II–IV the structure is noticeably refined to D_{gr} (F–P) = 30–100 μm (HAZ II, Figure 2, *d*); D_{gr} (F–P) = 10–40 μm (HAZ III, Figure 2, *e*) and D_{gr} (F–P) = 20–80 μm (HAZ IV). In HAZ zone II the microhardness practically corresponds to that in HAZ I at its further lowering in HAZ III, IV to *HV* (F–P) = 1700–1930 MPa.

At TMF application in HAZ I, a pearlite structure forms with D_{gr} (P) = 100–280 μm and interlayers of ferrite δ (F) = 20–50 μm (Figure 2, *c*) at *HV* (P) = 1990–2060 MPa, *HV* (F) = 1760–1930 MPa. In HAZ II a fine-grained structure (D_{gr} (F–P) = 20–70 μm (Figure 2, *f*)) forms, microhardness decreases slightly (*HV* (P) = 1870–1990 MPa; *HV* (F) = 1760–1810 MPa). In HAZ III, IV the structure is refined to D_{gr} (F–P) = 10–70 μm (Figure 2, *i*) at *HV* (F–P) = = 1700–1870 MPa (HAZ III) and *HV* (F–P) = 1760–1930 MPa (HAZ IV) at *HV* (F–P) = 1810–1930 MPa.

Comparison of *HV* (Figure 3) and microstructure (Figure 4) parameters of the studied samples revealed the following. In a sample produced without EEE, a noticeable *HV* increase is observed in HAZ I and II compared to weld metal (Figure 3, *a*). In a sample with LMF application (Figure 3, *b*), an increase of *HV* is observed near FL from the weld side and in HAZ I, compared to a sample without EEE. Here, Δ*HV* gradient is equal to 320 MPa. It can cause cracking with further brittle fracture of the welded joint. The most

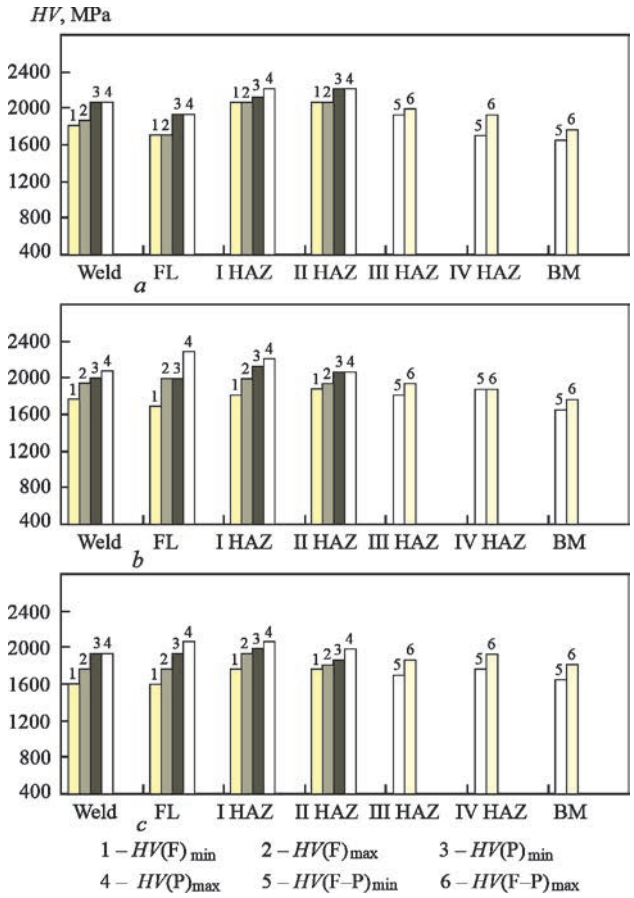

Figure 3. Microhardness (*HV*) of the metal of welded joints of 09G2S steel produced without EEE (*a*), with application of LMF (*b*) and TMF (*c*)

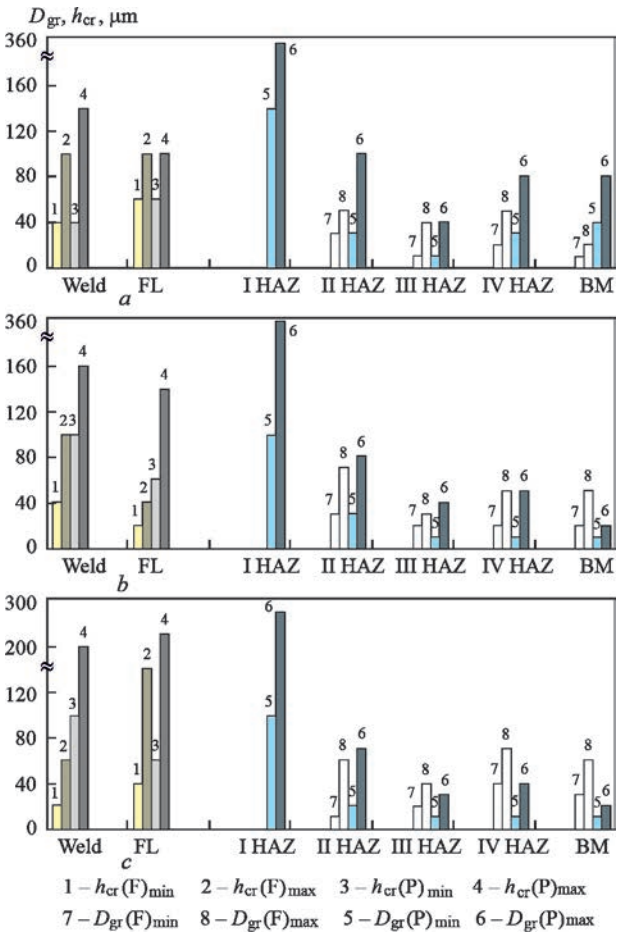

Figure 4. Structural parameters of the metal of 09G2S steel welded joints produced without EEE (*a*), with application of LMF (*b*) and TMF

uniform *HV* level both in the weld metal and in the HAZ, is observed in the welded joint produced with TMF application (Figure 3, *c*).

At application of LMF and TMF the grain structure in the welded joints is slightly coarsened in the weld metal near FL, compared to a sample without EEE (Figure 4). At transition to the HAZ, the structure is refined; slightly at LMF application and to a greater extent at TMF. Here, the width of ferrite interlayers at TMF decreases by 1.4 and 1.7 times on average, compared to samples without EEE or LMF. Moreover, at TMF application in HAZ I and II the grain is refined 1.3 times on average, compared to a sample without EEE. Such a dispersion of the structure will ensure both the strength, and higher fracture toughness of the metal and welded joint crack resistance, respectively. It should be also noted that EEE influence on the structural changes is the most evident in such local areas of welded joints and FL and HAZ I, and II.

Thus, it was established that the impact of EEE, in particular, of LMF and TMF, affects the HAZ dimensions, microstructure and microhardness of the metal of welds and HAZ, and crack formation in welded joints of low-alloy 09G2S steel.

At LMF application a coarse-grained structure forms, microhardness gradients are observed and cracks appear in FL zone. It can cause further brittle fracture of the welded joint.

TMF application ensures grain structure refinement in the overheated (HAZ I) and normalized (HAZ II) subzones, uniform level of microhardness, both in the weld metal, and in the HAZ subzones. Such structural changes will provide the strength, will improve the fracture toughness of the metal and will ensure cracking resistance of the welded joint, respectively.

CONCLUSIONS

1. In arc welding the impact of alternating magnetic fields affects the microhardness, microstructure parameters of welded joint metal and HAZ dimensions.

2. In welding low-alloy steel, the impact of external electromagnetic field is manifested to a greater extent in the zone of FL and HAZ in overheated (coarse-grain) and normalized (complete recrystallization) zones.

3. After application of the longitudinal magnetic field in FL zone, formation of a coarse-grain structure

at microhardness gradients led to cracking. It can be the cause of further brittle fracture of the welded joint.

4. Application of a transverse magnetic field ensured formation of the most favourable structure of welded joint metal at uniform level of microhardness, both in the weld metal, and in the HAZ subzones, and marked refinement of the structure in overheated (HAZ I) and normalized (HAZ II) zones. Such structural changes will both ensure the strength, and improve the fracture toughness of metal and crack resistance of the welded joint, respectively.

5. In welding low-alloy steel under EEE impact, the most effective is application of transverse magnetic fields, in which the induction vector is normal to the electrode and arc axes.

REFERENCES

1. Ryzhov, R.N., Kuznetsov, V.D., Prilipko, E.A. (2005) Calculation procedure of controlling electromagnetic effect parameters in arc welding of structural steels. *Vestnik HTUU KPI*, **45**, 176–177 [in Russian].
2. Ryzhov, R.N., Kuznetsov, V.D. (2006) External electromagnetic effects in the processes of arc welding and surfacing (Review). *The Paton Welding J.*, **10**, 36–44.
3. Ryzhov, R.N., Kuznetsov, V.D. (2005) Choice of optimal parameters of external electromagnetic action in arc methods of welding. *The Paton Welding J.*, **6**, 27–31.
4. Ryzhov, R.N. (2007) Influence of electromagnetic actions on process of formation and solidification of welds. *Svarochn. Proizvodstvo*, **2**, 56–58 [in Russian].
5. Ahieieva, A.D. (2019) Rational using of the controlling longitudinal and transverse magnetic fields at arc welding and surfacing. *IOP Conf. Series: Mater. Sci. and Engin*.
6. Ageeva, M.V., Razmyshlyaev, A.D. (2019) Influence of combined magnetic field on wire melting rate in arc surfacing. *Tekhnichni Nauky ta Tekhnologii*, 18(**4**), 22–27 [in Russian].
7. Boldyrev, A.M., Birzhev, V.A., Chernykh, A.V. (1992) To calculation of hydrodynamic parameters of liquid metal on welding pool bottom in arc welding. *Svarochn. Proizvodstvo*, **2**, 31–33 [in Russian].
8. Boldyrev, A.M., Birzhev, V.A., Martynenko, A.I. (2008) Examination of influence of variable axial magnetic field on process of electrode wire melting. *Svarochn. Proizvodstvo*, **2**(6–8), 63, 64 [in Russian].
9. Mironova, M.V. (2013) To choice of optimal schemes of input devices of transverse magnetic field for processes of arc welding and surfacing. In: *Zbirnyk Nauk. Prats of DSTU, Tekhnichni Nauky*, 21(**1**), 74–78 [in Russian].
10. Lazarenko, M.A., Razmyshlyaev, A.D. (2000) Structure of controlling magnetic fields for welding and surfacing processes using the devices with cylindrical 304 symmetry. *Visnyk PDTU*, **9**, 160–163 [in Russian].

ORCID

S.Yu. Maksymov: 0000-0002-5788-0753,
O.M. Berdnikova: 0000-0001-9754-9478,
O.O. Prylypko: 0000-0001-5244-5624,
O.S. Kushnaryova: 0000-0002-2125-1795,
T.O. Alekseyenko: 0000-0001-8492-753X

CONFLICT OF INTEREST

The Authors declare no conflict of interest

CORRESPONDING AUTHOR

S.Yu. Maksymov
E.O. Paton Electric Welding Institute of the NASU
11 Kazymyr Malevych Str., 03150, Kyiv, Ukraine.
E-mail: maksimov@paton.kiev.ua

SUGGESTED CITATION

O.D. Razmyshlyaev, S.Yu. Maksymov, O.M. Berdnikova, O.O. Prylypko, O.S. Kushnaryova, T.O. Alekseyenko (2022) Effect of external electromagnetic field configuration on metal structure of welded joints of structural steel. *The Paton Welding J.*, **10**, 13–17.

JOURNAL HOME PAGE

https://pwj.com.ua/en

Received: 29.08.2022
Accepted: 01.12.2022

DOI: https://doi.org/10.37434/tpwj2022.10.03

FEATURES OF RESISTANCE PREHEATING IN FLASH-BUTT WELDING OF THICK-WALLED PARTS FROM ALUMINIUM ALLOYS

K.V. Hushchyn[1], **I.V. Zyakhor**[1], **S.M. Samotryasov**[1], **M.S. Zavertannyi**[1], **A.M. Levchuk**[1], **Wang Qichen**[2]

[1]E.O. Paton Electric Welding Institute of the NASU
11 Kazymyr Malevych Str., 03150, Kyiv, Ukraine
[2]CIMC Offshore Engineering Institute Company Limited, Yantai, Shandong, P.R. China

ABSTRACT

The technological concept of flash-butt welding with resistance preheating using a reusable intermediate insert of a material with a high electrical resistance is proposed and substantiated by calculation. Calculation and experimental results indicate a significant effect of using intermediate insert during resistance heating: the temperature at both characteristic spots grows significantly at all investigated values of current density, insert thickness and heating time. The specified effect is achieved by intensifying and localizing the process of heat generation in the contact area of parts and correspondingly by reducing the energy loss for heating the secondary circuit of the welding machine.

KEYWORDS: flash-butt welding, resistance heating, aluminium alloy, mathematical modeling, temperature field

INTRODUCTION

An effective technology for producing permanent joint in the manufacture of load-carrying elements of aircrafts from rectilinear (stringers) and circumferential (shells) billets, pressed profiles of a developed and a compact cross-section (frame rings) is flash-butt welding (FBW). This method provides a high stable quality of joints, combines assembly and welding operations in a single cycle and does not require the use of auxiliary consumables [1–3]. In welding billets of aluminium alloys of up to 12 mm thickness, FBW technology provides high indices of strength and a high-quality (defect-free) joining at a slight width of the heat-affected zone (HAZ).

In FBW of profiles from aluminium alloys of larger thickness it is necessary to carry out a resistance preheating of billets by passing high-density electric current with a subsequent moving of billets apart and performing flashing and upsetting.

FBW technology with resistance preheating is widely used in various industries, in particular for joining parts of different thickness and configuration of steels of different classes [4–7]. In FBW of railway rails, preheating by current pulses [4, 5] (Figure 1, *a*) is used to provide the heat removal from the ends deep into billets. For more efficient resistance heating of billets from aluminium alloys, which have high values of electrical and thermal conductivity, continuous passing of current is used [1–3] (Figure 1, *b*).

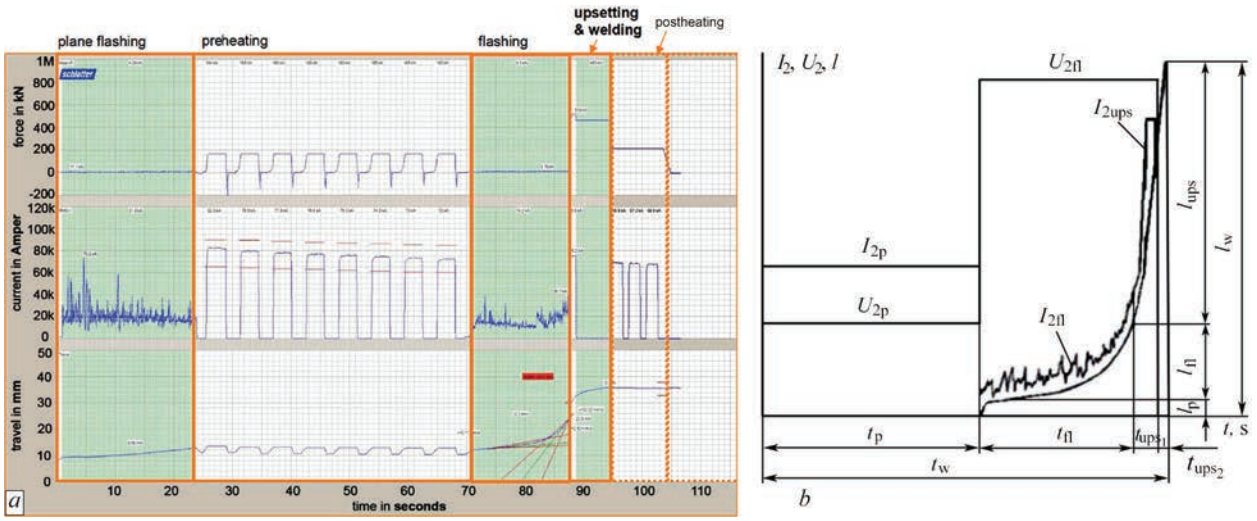

Figure 1. Cyclograms of the FBW process with preheating by current pulses (*a*) [5] and continuous (*b*) current passing [2]

Such heating process has low energy indices, and its duration reaches 80 % of the total welding duration [1]. Moreover, to ensure the formation of defect-free joints with an increase in the thickness of welded billets, the required resistance preheating temperatures grow. In particular, in [2] it is shown that in FBW of 2219 alloy, the optimal conditions of deformation during upsetting are provided during heating of the contact zone at the intensive deformation area to a temperature of about 400 °C. The need in increasing the resistance preheating temperature causes additional energy consumption for heating of the secondary circuit of the welding machine. At this time, the duration of the resistance heating stage grows, which leads to an increase in the width of welded joints HAZ and negatively affects the mechanical and operational properties of welded products from aluminium alloys.

Increasing the efficiency of resistance preheating, reducing its duration and loss of energy for heating of the secondary circuit of the welding machine is an urgent problem, the solution of which will provide significant energy saving and an improvement in the mechanical properties of welded joints of products of high-strength aluminium alloys.

The known technical solutions, where in order to increase the efficiency of heating in FBW, an interlayer in the form of a composite insert is used, in particular in welding of steel fittings [8], as well as in the form of a nanolayered foil (NF), in particular, in welding of titanium aluminides in similar [9] and dissimilar [10] joints.

In [8] in FBW of steel fittings, an interlayer represented a fluxed composite insert of profiled sheet of low carbon steel, which allowed localizing the process of heat generation in the contact zone. It is shown that when the current passes through the joint with an insert, which has a higher specific resistance, its intense heating and melting occurs. At the same time, the localization of heat generation is provided as compared to the traditional way of resistance heating, which contributes to the formation of quality joints at a smaller HAZ width than in welding without using an interlayer.

The authors [9, 10] investigated the features of formation of similar and dissimilar joints of Ti–46Al–2Cr–2Nb alloy based on γ-TiAl titanium aluminide in FBW, in particular, using interlayers in the form of NF. The work indicates that the presence of NF in the contact zone contributes to the formation of a thin layer of liquid phase at the initial stage of the heating process, localization of the heat generation process, the activation of the surfaces of both alloys at a much smaller duration of the heating stage as compared to welding without using an interlayer.

In [8–10] an intermediate insert represented thin foils, which are melted in the welding process and mainly displaced from the contact zone during upsetting, but they can partially remain in welded joints, significantly affecting their mechanical properties.

Unlike the abovementioned schemes of using a disposable insert that remains in the joint, for resistance preheating in FBW, it was suggested to use a reusable insert from a material with high indices of melting point and ohmic resistance. The technological concept of FBW applying a reusable intermediate insert was proposed, which is somewhat similar to butt welding process of polymer materials with heated tool [11]. However, it is significantly different, since the heat generation occurs both in the insert as well as in the welded parts, and the process of the temperature field formation depends on electrical and thermal processes, taking into account their complex interaction.

The aim of the work is to find the possibility of increasing the efficiency of resistance preheating process in FBW of aluminium alloys by intensification and localization process of heat generation in the contact area of the billets using an intermediate insert from a material with a high ohmic resistance.

RESEARCH METHODS, PROCEDURE, MATERIALS, EQUIPMENT

In the work, calculation and experimental research methods were used, in particular, the thermal cycles were calculated and the temperature fields were determined in the contact area of the billets using mathematical modeling of the heating process and by the empirical method while conducting experiments in the laboratory conditions.

The experiments were performed in a modernized K607 machine for FBW with a converted welding circuit, where as a power source, a welding transformer with 75 kV·A power was used, located directly under the current-conducting clamps of the machine.

For conducting experimental welds, the specimens of 2219 aluminium alloy with a cross-section of 32×60 mm were used. An intermediate insert represented plates of austenitic steel 12Kh18N10T of 7 mm thickness. The temperature fields were experimentally investigated using a computerized temperature registration system based on 8-channel USB-module for thermocouples Advantech USB-4718 using the chromelle-alumel thermocouples with a diameter of 0.5 mm.

Figure 2 shows the program for changing FBW mode parameters, which provides a consecutive change of four main stages of heating before forming a welded joint during upsetting. Between I and II stages, moving of the welded parts apart and clamping of the intermediate insert between them is performed, and between II and III stages, respectively, moving of the parts apart and removing of the insert from the gap between them is performed.

The scheme of the intermediate insert arrangement between the welded parts offered in this work is shown in Figure 3. In such a scheme of heating, the amount of heat dQ generated in the parts during resistance heating over the period of time dt according to the law of Joule–Lenz, can be represented as

$$dQ = I_w^2 (R_{in} + R_p + 2R_c)dt, \quad (1)$$

where I_w is the welding current; R_{in} is the electric current of the insert; R_p is the electrical resistance of the welded parts; R_c is the transitional contact resistance between the parts and the insert.

CALCULATION STUDY OF THE RESISTANCE HEATING PROCESS

In FBW with resistance preheating, it is essential to achieve a certain value of temperature in the intensive deformation zone. The optimal conditions for the welded joint formation during upsetting are created when the yield and tensile strength of the material of the billets in the deformation zone are equal [2]. In this case, producing of welded joints is provided with a minimum level of inner stresses with the absence of microcracks and other defects. In FBW with the forced formation, the width of the intensive deformation zone practically coincides with the value of the upsetting tolerance, so the optimal conditions for deformation of the billets from 2219 alloy are created at a temperature of about 400 °C [2].

To optimize the temperature field, during resistance preheating of the billets, it is essential to reach the set temperature at characteristic spots, namely: at the first one – at the ends of the billets (contact zone) and at the second one – at a distance of about 30 mm from the contact zone. This value, which was determined on the basis of a previous practical experience on FBW of thick-walled parts of aluminium alloys, corresponds to half of the set value of the total welding tolerance l_w = 60 mm ($l_w/2$ = 30 mm), i.e., the second characteristic spot after performing the processes of flashing and upsetting will be in the plane of the welded joint.

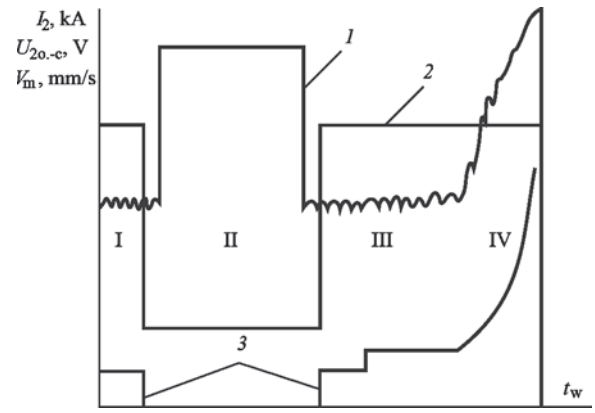

Figure 2. Program for changing parameters of FBW process with resistance preheating using an intermediate insert: I — preliminary flashing; II — resistance heating through an intermediate insert; III — flashing at a constant rate; IV — intensive flashing (forcing) before upsetting; *1* — welding current I_2; *2* — secondary open-circuit voltage of the welding transformer $U_{2o.-c}$; *3* — movement of the moving column of the welding machine V_m

As the criterion of efficiency of resistance heating, reaching a set temperature at the characteristic spots of parts at the least time at a set value of current density was considered. From the point of view of stability of flashing stages at a constant rate and intense flashing (see Figure 2, III and IV stages), the desired result of resistance preheating is the achievement of the highest possible value of temperature at the first of the characteristic spots (contact zone), but not lower than 150–200 °C [1, 12]. As the criterion of sufficient resistance heating of parts, reaching a temperature of 150 °C at the second of the characteristic spots (at a distance of 30 mm from the contact zone) was considered. In this case, in the process of the next stages of FBW, a gradual heating of the parts to a temperature of 400 °C is achieved in the deformation zone between the forming devices of the welding machine and the necessary conditions for the formation of defect-free welded joints are provided during upsetting.

The process of the temperature field formation in FBW is predetermined by the complex distribution of Joule heat sources. Heat transfer which, along with heat generation forms a temperature field in metal, is performed in a conductive way. The thermal conductivity of metal, its specific electrical resistance and other physical properties depend significantly on the temperature. The welding current, which determines the intensity of thermal impact on the metal depends on the open-circuit voltage, resistance of welded parts and inner resistance of the machine for resistance welding. Therefore, an adequate mathematical model of the process of the temperature field formation during resistance heating should include a description of electrical and thermal processes in the welded metal, taking into account their complex interaction. The welding current (current density) should be set on the basis of experimental data. The heat generation is determined by the calculation way, taking into account the electrical resistance of the welding zone, and the properties of the metal at each spot of the calculated

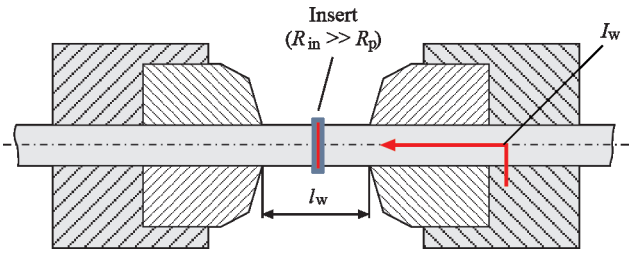

Figure 3. Scheme of the resistance heating process through an intermediate insert in the current-carrying clamps of the machine for FBW (l_w — tolerance for welding)

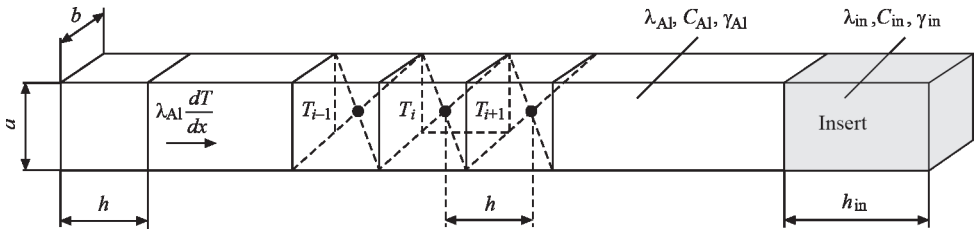

Figure 4. Scheme of the mesh of calculation model

area should be set according to the current distribution of the temperature filed of a part.

Unlike the predominantly volumetric heat generation in the billets between the current-carrying clamps of the welding machine during resistance heating without an insert (transient contact resistance between the parts from aluminium alloys is insignificant), during resistance heating through the insert, an additional source of heat generation appears, which can be linear (at a slight thickness of the insert, in particular, when using thin foil) or volumetric (when using a plate with a thickness of several millimeters). In the latter case, the temperature field in the heated parts will be formed according to a law close to the exponent.

The calculation scheme for the case of a one-dimensional problem is shown in Figure 4.

To simplify the calculation, the temperature distribution in the cross-section of the welded billets can be neglected. Based on this, the problem is solved in a one-dimensional statement. The one-dimensional nonstationary heat conduction equation for the case of a onedimensional problem in Cartesian coordinates has the following form [13]

$$c(T)\gamma(T)\frac{\partial T}{\partial t}=\frac{\partial}{\partial x}\left[\lambda(T)\frac{\partial T}{\partial x}\right]+q_v, \qquad (2)$$

where T is the temperature, K; t is the time, s; q_v is the volumetric density of inner heat sources, W/m^3.

Discretization of the calculation area was carried out, which consists in replacing the continuous determination area and the continuous area of the function value for the corresponding discrete areas. In our nonstationary problem, it is necessary to discretize both the spatial calculation area as well as the time. As the beginning of the countdown, let us choose one of the ends of the parts that is heated.

On the section of the axis x, let us select the spot x_i, $i = 0 – 1, \ldots, n – 1, n$. Let us assume that the distance between two adjacent discretization spots x_i and x_{i+1}, equal to the discretization step h, will be the same, i.e., the discretization of the computational domain is uniform. At the same time, to each discretization spot x_i the value of the temperature t_i corresponds.

The welded specimen has a cross-section with dimensions $a \times b$. Therefore, the volume of one element is determined by the formula $a \times b \times h$. If the nonlinearity of the thermophysical properties of the heated parts is not previously taken into account (dependencies $\lambda(T)$, $c(T)$ and $\gamma(T)$), then the nonlinearity of the problem will consist only in taking into account the dependence of the power density of the Joule heat source q_s:

$$q_J(T)=\frac{I^2\rho(T)h}{abh(ab)}=\frac{I^2\rho(T)}{a^2b^2}, \qquad (3)$$

where ρ(T) is the temperature dependence of the specific electrical resistance of the parts.

Taking the expression (2) into account, let us write down the approximation of the initial differential equation of thermal conductivity (1) for the i-th spatial spot and the j-th moment of time

$$c_i\left(T_i^*\right)\gamma_i\left(T_i^*\right)\frac{T_i-T_i^*}{t-t^*}=\frac{2}{\left(x_{i+1}-x_{i-1}\right)}\times$$
$$\times\left[\lambda_{i+1}\left(T_{i+1}^*\right)\frac{T_{i+1}-T_i}{x_{i+1}-x_i}-\lambda_i\left(T_i^*\right)\frac{T_i-T_{i-1}}{x_i-x_{i-1}}\right]+ \qquad (4)$$
$$+\frac{I^2\rho_i\left(T_i^*\right)}{a^2b^2},$$

Table 1. Thermophysical characteristics of 12Kh18N10T steel and 2219 alloy

T, °C	12Kh18N10T			2219 alloy		
	λ, W/(m·K)	c, J/(kg·K)	ρ·10^{-9}, Ohm·m	λ, W/(m·K)	c, J/(kg·K)	ρ·10^{-9}, Ohm·m
20	15	450	725	130	0.8	55.3
100	16	462	792	142	0.86	62.4
200	18	496	861	155	0.92	72.2
300	19	517	920	163	1.05	77.2
400	21	538	976	167	1.05	85.6
500	23	550	1028	–	–	–
600	25	563	1075	–	–	–
700	27	575	1115	–	–	–

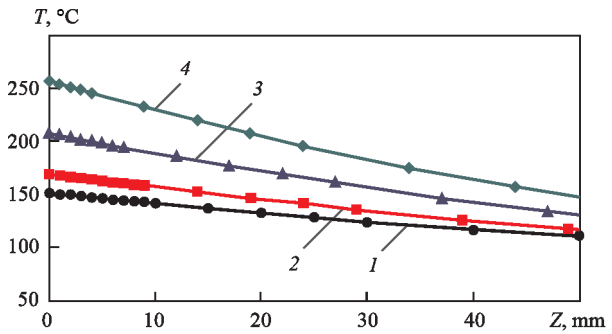

Figure 5. Calculated temperature fields during resistance heating through an intermediate insert of 12Kh18N10T steel of the thickness h_{in} = 2 (*2*), 6 (*3*), 12 (*4*) mm and without an insert (*1*) (h_{in} = = 0 mm) for the current density J = 10 A/mm^2 and t_h = 60 s (Z — distance from the ends of parts)

where T_i^* is the temperature in the calculation node at the previous time step (the step size is Δt); $c_i(T_i^*)$, $\gamma_i(T_i^*)$, $\lambda_i(T_i^*)$ is the temperature dependence of heat capacity, density, and thermal conductivity of the heated parts, respectively.

To calculate the temperature field, the following input data are entered into the mathematical model: geometric dimensions of welded parts and thickness of an intermediate insert; thermophysical characteristics of aluminium alloy and intermediate insert material (Table 1). The basic input parameters of heating mode are current density and heating time.

Using the developed mathematical model, the temperature fields during resistance heating of billets of 2219 aluminium alloy with a cross-section of 32×60 mm was calcualted depending on the thickness of the intermediate insert h_{in} of steel 12Kh18N10T at a heating time t_h = 60 s (Figure 5) and different current density J at t_h = 40 s (Figure 6).

Based on the obtained data, the dependence of the temperature of the characteristic spots of the welded joint on the current density during resistance heating without an insert and with the use of an intermediate insert of steel 12Kh18N10T was plotted (Figure 7).

The analysis of the obtained calculated temperature fields (Figure 5) shows that during resistance heating without inserting the parts of 2219 alloy with a cross-section of 32×60 mm at a time before t_h = 60 s at a current density J = 7.5 and 10 A/mm^2, the achievement of the specified temperature in the characteristic spots of the parts — in the contact zone and at a distance of 30 mm from the ends is not provided. The temperature distribution necessary for the formation of high-quality joints during resistance heating without an insert is achieved at a current density $J \geq$ 12.5 A/mm^2 (Figure 6, *a*), which in practice causes significant energy losses for heating the secondary circuit of the welding machine and the need in using power sources of high capacity.

The results of the calculations shown in Figures 5 and 6, *b*, indicate a significant effect of using an intermediate insert during resistance heating — the temperature at both characteristic spots grows significantly at all the investigated values of current density, insert thickness and heating time. It was found that the efficiency of the resistance heating process through the intermediate insert depends on its thickness: the set temperature distribution in the parts of 2219 alloy at the current density J = 10 A/mm^2 and heating time t_h = 60 s is achieved at $h_{in} \geq$ 6 mm.

For a set thickness of the insert, the efficiency of the heating process increases with a growth in the current density J (Figure 6, *b*), in particular, the set temperature distribution in the parts at h_{in} = 7 mm and heating time t_h = 40 s is achieved for all the investigated values of the current density J, except of J = 7.5 A/mm^2. A significant increase in temperature in the contact zone for all the values of the investigated parameters during heating through the insert should be noted, in particular at J = 12.5–15 A/mm^2 to T = 300–420 °C as compared to T = 180–270 °C during heating without an insert. The last fact is particularly important from the point of view of the stability of the flashing stages

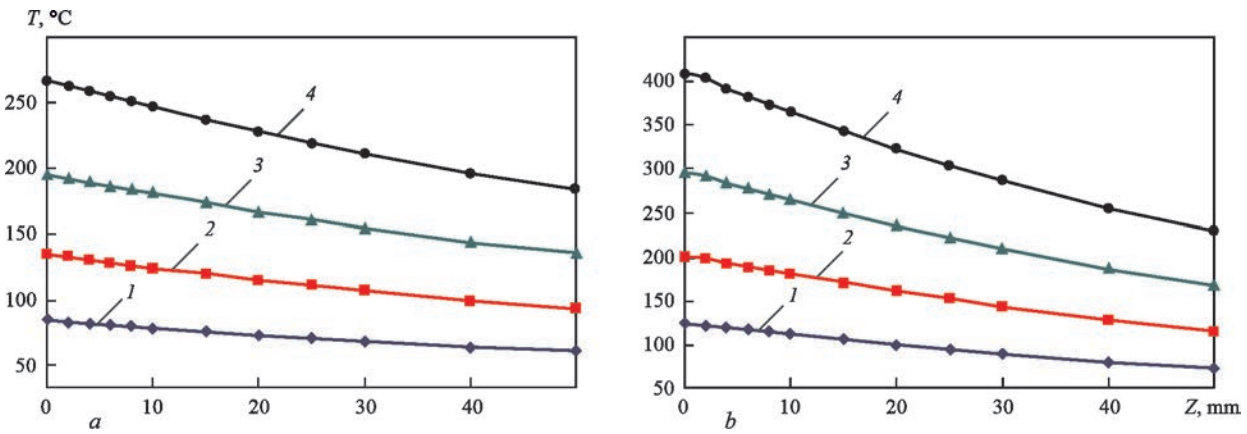

Figure 6. Calculated temperature fields during resistance heating without an insert (*a*) and through an intermediate insert of 12Kh18N10T steel of the thickness h_{in} = 7 mm (*b*) at t_h = 40 s and current density J = 7.5 (*1*), 10 (*2*), 12,5 (*3*), 15 (*4*) A/mm^2

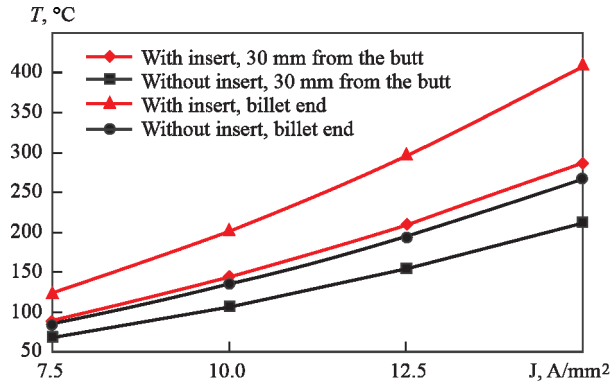

Figure 7. Calculated dependence of temperature of the characteristic spots of the welded joint on current density J in resistance heating using an intermediate insert of 12Kh18N10T steel and without it

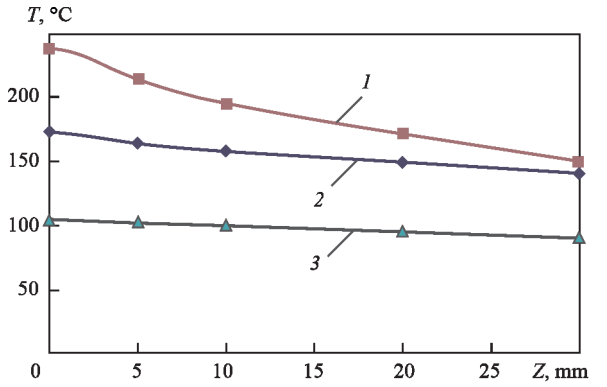

Figure 8. Temperature fields during resistance preheating using an intermediate insert of 12Kh18N10T steel of the thickness h_{in} = = 7 mm (*1*) and without an insert (*2*, *3*) during heating time t_h = 40 (*1*, *3*) and 85 s (*2*)

at a constant rate (see Figure 2, II stage) and intensive flashing before upsetting (IV stage), and from a practical point of view it makes it possible to guarantee the absence of welding defects (lacks of penetration, oxide films, matte spots) at a significantly lower power source of the welding machine.

The obtained results confirm the assumption that during resistance heating through an insert, an additional volume source of heat generation appears, which ensures more rapid heating of the metal at both characteristic spots — in the zone of intense deformation during upsetting and the contact zone of the parts and causes a decrease in energy loss for heating the secondary circuit of the welding machine.

EXPERIMENTAL STUDY OF RESISTANCE HEATING PROCESS

The experiments on studying thermal cycles of resistance heating of the parts with a cross-section of 32×60 mm of 2219 aluminium alloy were carried out at the secondary voltage of the transformer $U_{2o.-c}$ = 3 V. The chromel-alumel thermocouples with a diameter of 0.5 mm were mounted in the parts at a distance of 5, 10, 20 and 30 mm from the ends on the inner side of the secondary circuit of the welding machine. The parts were heated directly (without an insert) and through an intermediate insert of 12Kh18N10T steel at a current density of about 10 A/mm² and heating time t_h = 40 and 85 s. Based on the calculation results, indicating the expediency of using the insert when its thickness is $h_{in} \geq 6$ mm, the experimental study of temperature fields was carried out at h_{in} = 7 mm.

The results of the experiments show that without using an intermediate insert at the set energy parameters of the preheating mode, it was impossible to achieve the required distribution of the temperature field during the time t_h = 40 and 85 s (Figure 8, curves *2*, *3*). At t_h = 85 s the process of heating almost transferred to a quasi-stationary state. The temperature in the contact zone at t_h = 85 s amounts to about 170 °C, and at a distance of 30 mm it was 140 °C. During heating of parts through the insert of 12Kh18N10T steel, the temperature in both characteristic spots is significantly increased and the temperature distribution required for the next stages of flashing is achieved during the time t_h = 40 s (Figure 8, curve *1*).

It is worth noting a significant increase in temperature in the contact zone while heating through the insert at t_h = 40 s, and a much higher gradient of temperature field as compared to heating without the insert at t_h = 85 s. The experimentally established growth of temperature in the contact zone is especially important in terms of stability of flashing stages and preventing the formation of defects in welded joints. In FBW of heat-strengthened alloys, the reduction in the duration of resistance heating contributes to minimizing negative structural and phase transformations in the heat-affected zone and causes maintaining of the values of strength, corrosion resistance and other service properties of welded products at a higher level [12].

Experimental study of temperature fields in the parts from 2219 alloy during their resistance heating using an intermediate insert of 12Kh18N10T steel at t_h = 40–85 s indicates the intensification and localization of the heat generation process in the contact area as compared to the heating process without the insert and confirm the calculation data according to the proposed generalizations.

Therefore, the results of the calculations and the experimental study of the temperature fields indicate an increase in the efficiency of the process of resistance preheating in FBW of aluminium alloys using an intermediate insert from the material with high electrical resistance. The mentioned effect is achieved by intensification and localization of the heat generation process in the contact zone of parts and a corresponding reduction in the «irrational» energy loss on heating of the secondary circuit of the welding machine.

CONCLUSIONS

1. The technological concept of flash-butt welding (FBW) of thick-walled parts from aluminium alloys with resistance preheating applying a reusable intermediate insert. The efficiency of the process of resistance preheating in FBW of 2219 aluminium alloy using an intermediate insert of 12Kh18N10T steel was investigated by calculation. As the criterion of the effectiveness of resistance heating, the achievement of the set temperature in the characteristic spots of the parts — in the contact zone and at a distance of 30 mm from the ends of the parts in the shortest time at the set value of the current density was considered.

2. It was established that as compared to direct resistance heating of parts using an intermediate insert of 12Kh18N10T steel, the temperature rises significantly at both characteristic spots at all investigated values of current density, thickness of the insert and heating time.

3. For the set thickness of the insert h_{in} in the studied range h_{in} = 2–12 mm the efficiency of the heating process increases with a growth in the current density J, and at the set value of J in the range J = 7.5–15 A/mm^2 — at an increase in the thickness of the insert.

4. A significant increase in the gradient of the temperature field in the parts during heating through the insert was established: the temperature in the contact zone at J = 12.5–15 A/mm^2 amounted to T = 300–420 °C as compared to T = 180–270 °C during heating without an insert. The mentioned result is important from the point of view of the stability of the subsequent stages of flashing in FBW and from a practical point of view, it makes it possible to guarantee the absence of welding defects at a significantly lower capacity of the power source of the welding machine.

5. An experimental study of the temperature fields in the parts of 2219 alloy during their resistance heating using an intermediate insert of 12Kh18N10T steel is confirmed by the calculated data and they indicate the intensification and localization of the heat generation process in the contact zone as compared to the heating process without an insert.

REFERENCES

1. Kuchuk-Yatsenko, S.I. (1992) *Flash butt welding.* Kyiv, Naukova Dumka [in Russian].
2. Kuchuk-Yatsenko, S.I., Chvertko, P.N., Semyonov, L.A. et al. (2010) Peculiarities of flash butt welding of high-strength aluminium alloy 2219. *The Paton Welding J.*, **3**, 7–9.
3. Kuchuk-Yatsenko, S.I., Gushchin, K.V. (2018) *Flash butt welding of high-strength aluminium-based alloys: Science of Materials: Achievements and Prospects.* Kyiv, Akademperiodyka [in Russian].
4. Weingrill, L., Krutzler, J., Enzinger, N. (2017) Temperature field evolution during flash-butt welding of railway rails. *Materials Sci. Forum*, 879, 2088–2093. DOI: 10.4028/www.scientific.net/MSF.879.2088.
5. https://www.schlattergroup.com/en/welding-machines/flash-butt-welding-machines-for-rails/
6. (2014) *Preheating burnoff flash butt welding method for welding large-section steel vehicle wheels.* Pat. CN103894717A.
7. Shi, S.-C., Wang, W.-C., Ko, D.-K. (2022) Influence of inclusions on mechanical properties in flash butt welding joint of high-strength low-alloy steel. *Metals*, 242(**12**), 1–13. DOI: 10.3390/met12020242.
8. Kuchuk-Yatsenko, V.S., Nakonechny, A.A., Sakhatsky, A.G. (2010) Resistance welding of steel reinforcement using composite insert. *The Paton Welding J.*, **4**, 34–36.
9. Kuchuk-Yatsenko, S.I., Zyakhor, I.V., Chernobaj, S.V. et al. (2015) Structure of γ-TiAl joints in resistance butt welding with application of interlayers. *The Paton Welding J.*, **9**, 5–12. DOI: 10.15407/tpwj2015.09.01.
10. Kuchuk-Yatsenko, S.I., Zyakhor, I.V., Nakonechny, A.A. et al. (2018) Resistance butt welding of titanium aluminide γ-TiAl with VT5 alloy. *The Paton Welding J.*, **9**, 2–6. DOI: 10.15407/tpwj2018.09.01.
11. Iurzhenko, M.V. (2019) Novel technological approach to butt welding «in closed volume» with heated tool of polymer multilayer composite pipes. *Visnyk KhNTU. Inzhenerni Nauky*, 68(**1**), 65–72 [in Russian].
12. Kuchuk-Yatsenko, S.I., Hushchyn, K.V., Ziakhor, I.V. et al. (2021) Structure and mechanical properties of 2219-T87 aluminium alloy joints produced by flash butt welding. *The Paton Welding J.*, **8**, 27–32. DOI: https://doi.org/10.37434/tpwj2021.08.06
13. Tkachenko, V.N. (2008) *Mathematical modeling, identification and control of technological processes of heat treatment of materials.* Kyiv, Naukova Dumka [in Russian].

ORCID

K.V. Hushchyn: 0000-0003-3298-4537,
I.V. Zyakhor: 0000-0001-7780-0688,
S.M. Samotryasov: 0000-0003-4891-9625,
M.S. Zavertannyi: 0000-0002-8415-8555,
A.M. Levchuk: 0000-0002-0361-7394

CONFLICT OF INTEREST

The Authors declare no conflict of interest

CORRESPONDING AUTHOR

I.V. Zyakhor
E.O. Paton Electric Welding Institute of the NASU
11 Kazymyr Malevych Str., 03150, Kyiv, Ukraine.
E-mail: zyakhor2@ukr.net

SUGGESTED CITATION

K.V. Hushchyn, I.V. Zyakhor, S.M. Samotryasov, M.S. Zavertannyi, A.M. Levchuk, Wang Qichen (2022) Features of resistance preheating in flash-butt welding of thick-walled parts from aluminium alloys. *The Paton Welding J.*, **10**, 18–24.

JOURNAL HOME PAGE

https://pwj.com.ua/en

Received: 22.08.2022
Accepted: 01.12.2022

DOI: https://doi.org/10.37434/tpwj2022.10.04

CHARACTERISTICS OF FORMATION AND PROPERTIES OF BRASS–STEEL JOINT PRODUCED BY AUTOVACUUM CLADDING

I.P. Serebryanyk, M.A. Polieshchuk, T.O. Zuber, A.I. Borodin, A.Yu. Tunik, O.A. Los

E.O. Paton Electric Welding Institute of the NASU
11 Kazymyr Malevych Str., 03150, Kyiv, Ukraine

ABSTRACT

The technological features of producing a brass–steel joint by the method of autovacuum heating are considered. The thickness of the brass layer after machining was 10 mm. Studying the structures and chemical composition of various joint zones confirmed the solution-diffusion nature of interaction of liquid brass with steel. Microhardness measurements showed absence of hard and brittle structures. A high quality of the joint was confirmed by mechanical tests of the two-layer joint for static bending, tear and shear.

KEYWORDS: brass, steel, two-layer joint, autovacuum heating

INTRODUCTION

The joints of brass and carbon steels are used in manufacture of various products. These are two-layer sleeves, supporting components [1], rolled sheets with a cladding layer from copper alloys [2], joints of steel and cast iron parts, where brass is used as filler metal [3]. These joints mostly form under atmospheric pressure. Brazed joints are also produced in vacuum or controlled atmosphere.

Normative documents for manufacture of tube plates for modern tubular heat exchangers envisages a high quality of brass–steel joint at joint area of more than $1.5 \cdot 10^4$ cm^2 and 10 mm thickness of the cladding layer [4].

The objective of the work is development of a cost-effective technology of producing a sound brass–steel joint of a large area with up to 10 mm thickness of the brass. Here, equipment currently available at industrial enterprises should be used.

The experimental part of this work is a continuation of the performed studies of liquid copper interaction with steel [5] and it confirmed their main conclusions.

EXPERIMENTAL MATERIALS AND PROCEDURE

The steel base of the joint was made from St14G2 steel [6], the brass layer — from L59 brass [7]. The assembled package for cladding was sealed by making vacuum-tight welds. 2NVR-5DM vacuum pump was used to pump air out of the package to $2 \cdot 10^{-2}$ Pa. Samples were heated in SNOL-04534 thermal furnace.

Metallographic analysis method was used to study the macro- and microstructure of the longitudinal and transverse sections of the produced joints. Investigations were performed using Neohpot-32 optical microscope, fitted with an attachment for digital filming. The system of image recording was realized using QuickPhoto computer program.

Samples for metallographic investigations were prepared by standard procedures. Microhardness was measured in M-400 hardness meter of LECO Company at 0249 and 0496 N. The reagents for revealing the sample microstructure (Table 1) were selected, based on our developments and recommendations of work [8].

Sample investigations by the methods of scanning electron microscopy (SEM), and X-ray microprobe analysis (XRMA) were conducted in Jamp-9500F instrument of Jeol Company, Japan, fitted with X-ray energy-dispersive spectrometer INCA Penta FET×3 (OXFORD INSTRUMENTS). The energy of the primary electron beam was equal to 10 keV at 0.5 mA current for SEM and XRMA methods and 10 mA current for Auger-electron spectroscopy. Auger spectra were recorded with energy resolution $\Delta E/E = 0.6$ %.

Table 1. Reagents for metallographic etching of the samples

Etching purpose	Reagent composition	Method of application	Note
Revealing the microstructure	HNO_3 — 50 ml H_2O — 50 ml	Chemical etching at intensive stirring of the reagent t = 20 °C, τ = 5–30 s	Oxide film removal: HCl — 20 ml H_2O — 80 ml, τ = 1–3 s, t = 20 °C
Revealing the macrostructure	HNO_3 — 50 ml H_3PO_4 — 25 ml (CH_3COOH) — 25 ml	Chemical etching at intensive stirring and heating of the reagent up to t = 70 °C, τ = 5–30 s	

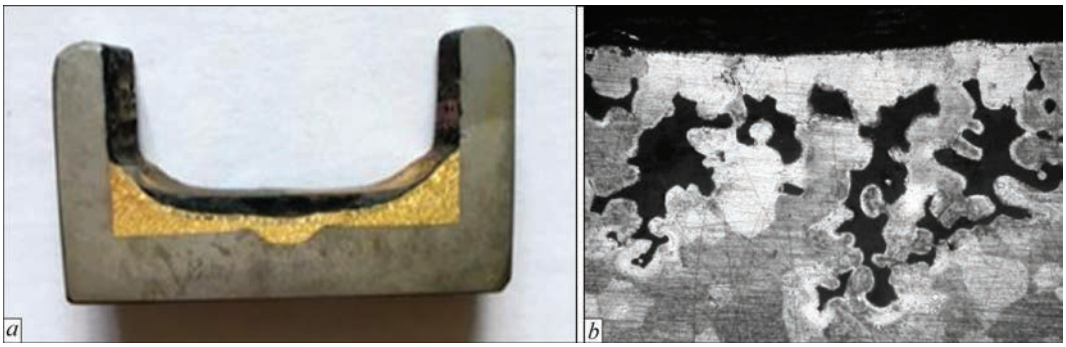

Figure 1. Brass–steel joint produced by open heating: *a* — joint macrosection; ×1.5; *b* — discontinuity in the surface layer of brass, ×100

Prior to investigations, the sample surface was cleaned directly in the instrument analysis chamber by etching by argon ions Ag^+ with 1 keV energy for 10 nm/min. SiO_2 etching rate was nm/min. Vacuum in the analysis chamber was in the range of $5 \cdot 10^{-8}$–$1 \cdot 10^{-5}$ Pa.

EXPERIMENTAL RESULTS

Obtaining a sound brass–steel joint by pouring using open heating in a thermal furnace is impossible, because of formation of pores and discontinuities in brass, provoked by zinc evaporation [9]. Here, the brass layer surface has defects to the depth of down to 500 μm. It leads to high labour consumption for machining of the brass surface and additional brass consumption for technological allowance. Figure 1 shows a brass–steel joint, produced by open heating, and the microstructure of the brass surface layer.

When searching for a replacement for open heating, the following known methods of producing two-layer brass–steel billets were considered: explosion welding [10], submerged-arc surfacing [11], laser welding [12], plasma surfacing [13], etc. Application of these technologies, however, requires designing and manufacturing special equipment.

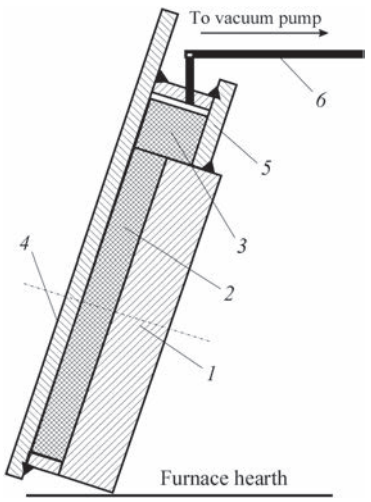

Figure 2. Scheme of cladding the billet by flowing with forced replenishment: *1* — carbon steel base; *2* — brass sheet; *3* — brass for replenishment; *4* — cover; *5* — accumulator; *6* — nozzle for vacuum pump

Current experience of brazing application in autovacuum to produce brass–steel joints [14] showed that this technology ensures a high quality of the joint at 0.5–3.0 mm thickness of the brass layer. Autovacuum application envisages use of available industrial equipment with minor additions. First of all, it was necessary to ensure deposition of a cladding layer of a uniform thickness at minimum allowance for machining, which was achieved by application of a scheme of cladding with forced replenishment (Figure 2).

All the welds were made on the assembled package and checked for tightness. A vacuum pump was used to pump out air from the inner cavity to $2 \cdot 10^{-2}$ Pa. The assembly was heated in a standard thermal furnace at T = 1000 °C and soaking for 15 min. Cooling was performed with the furnace to 400 °C, then — with open door at atmospheric conditions.

A feature of heating the assembly located in the container with a vacuumized cavity, is the fact that heat transfer is performed only by radiation due to absence of gas in the cavity. The time required for the assembly heating is equal to 13 min, for specific dimensions of the clearance between the container walls and assembly surface. Therefore, when designing the heating mode it was necessary to increase the assembly soaking time at brazing temperature by 13(15) min.

At examination of the brass layer (after removal of the cover by machining) it was found that brass melted completely both in the main cavity, and in the replenishment cavity, and good wetting of the steel part is in place. No pores or discontinuities were observed in the brass cross-section (Figure 3).

The strength and reliability of brass–steel joint is directly related to the structure and composition of metal in the contact zone. Metallographic investigations showed that St14G2 steel preserves its ferrite-pearlite structure after heating. The structure of L59 brass is two-phase (α+β), it consists of a light-coloured α-matrix and small areas of β-phase, which etches darker (Figure 4). After performance of analysis, it was found that chemical composition of brass changed after heating, and zinc content dropped from 40 to 37 wt.%.

Table 2. Chemical composition of meal of the studied joint areas, wt.%

Area number	Si	Mn	Fe	Cu	Zn
1	0.10	0.12	18.39	49.66	28.97
2	0.04	0.16	42.72	33.84	20.30
3	0.36	0.16	79.14	10.85	6.95
4	0.22	0.08	76.80	5.68	3.17
5	0.03	0.08	4.34	59.26	33.48
6	0.25	0.00	90.84	3.49	3.09

The questions of liquid brass interaction with solid steel are fundamental at prediction of the joint reliability. These processes were repeatedly studied by different authors. Some of them state that cracks form on the steel surface at its contact with liquid copper and its alloys during deposition, which are filled with liquid [15]. In this case, the composition of the metal filling the "crack" should be close to the initial one, and the "crack" tip cannot be filled completely, in keeping with the law of capillarity [5].

Another approach to interaction of the melt of copper and its alloys with steel is given in detail in [5]. According to it, the interaction of brass melt with solid steel takes place due to dissolution and diffusion of elements, located on the steel grain boundaries, and further separation and movement of these grains into the melt. In the areas of brass penetration, iron and other components of steel should be registered, in addition to initial elements.

At a considerable magnification, brass penetration into steel was recorded in the optical (Figure 5, *a*) and electron (Figure 5, *b*) microscopes to the depth of 1.5–10 μm. The chemical composition of metal in the studied areas is given in Table 2.

After brass penetration into steel to the depth of 10 μm, a considerable amount of iron is registered in it: 18.39–42.72 wt.% (areas 1, 2). In steel grains that separate and go into brass (areas 3, 4), copper is found in the amount of 5.68–10.85 and zinc in the amount of 3.17–6.95 wt.%. In areas 5 and 6, where no interpenetration of metals is observed, the diffusion processes are less significant. In brass 4.34 % of iron, and in steel 3.49 of copper and 3.09 wt.% of zinc were registered.

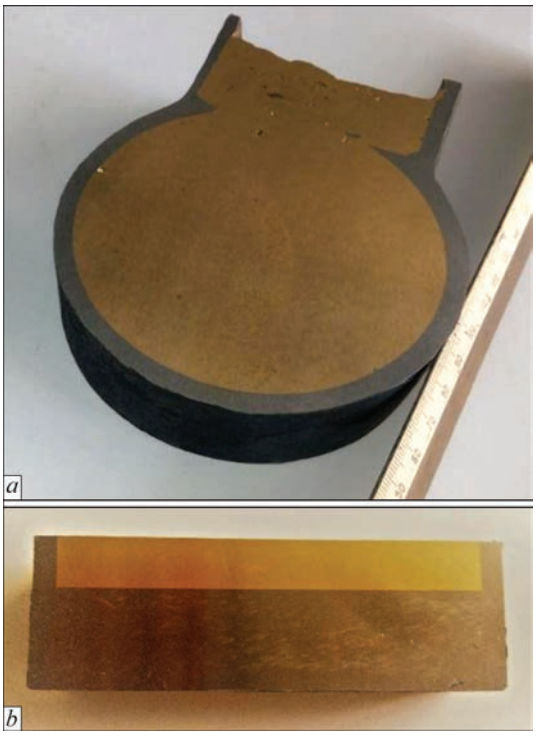

Figure 3. General view (*a*) and diametral cross-section (*b*) of the brass–steel joint produced in autovacuum, ×0.5

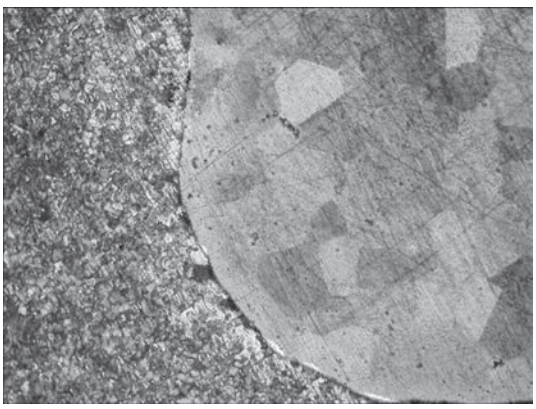

Figure 4. Microstructure of brass–steel joint after etching, ×100

At analysis of microhardness in brass and steel areas located near the contact zone, no formation of solid or

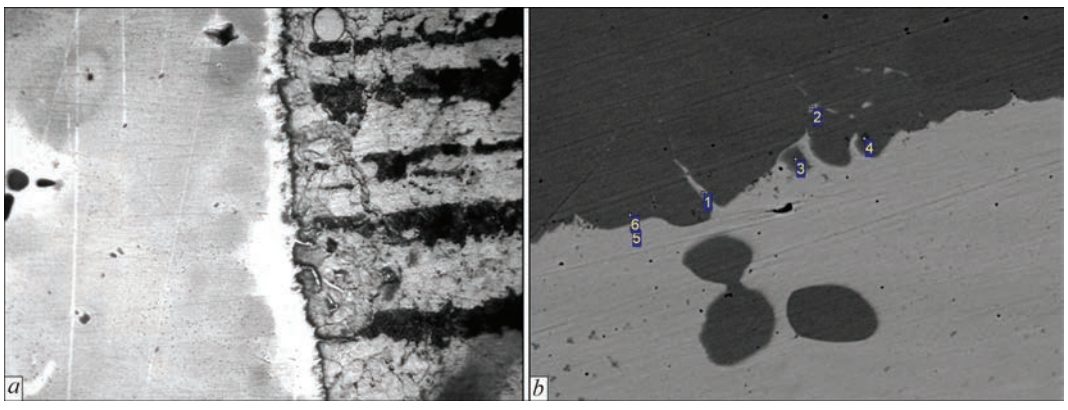

Figure 5. Zone of brass–steel contact: *a* — optical, ×500; *b* — electron microscopic image ×1500 (etched)

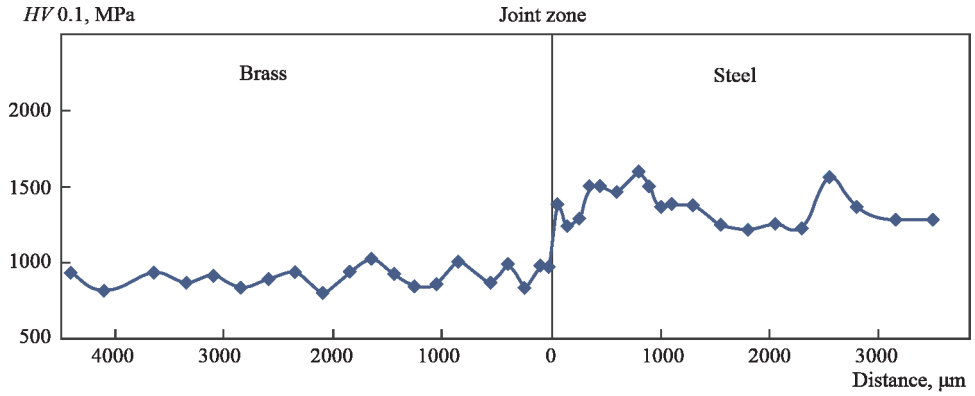

Figure 6. Metal microhardness in brass–steel joint

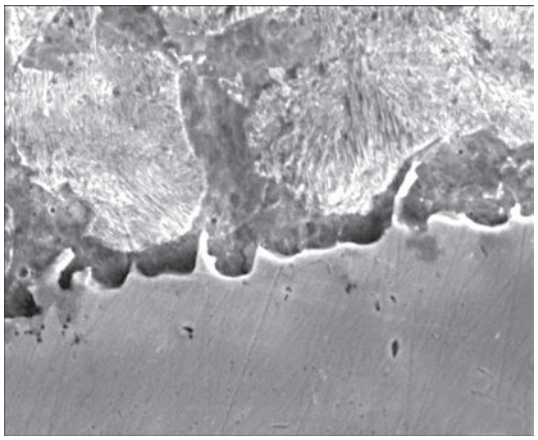

Figure 7. Steel microstructure in brass–steel contact zone, ×1600

brittle structures was found (Figure 6). At the same time, it is necessary to pay attention to the structure of steel in the zone of contact with brass (Figure 7).

The chain of dark grains from the steel side is pearlite grains. Carbon in steel is known not to interact with copper. Its concentration in the contact zone grows which at long-time soaking (more than 30 min) may lead to formation of a chain of brittle grains of pearlite along the contact boundary from the steel side. In this connection, the duration of soaking in the furnace is limited to 15 min. As a result, pearlite accumulations were insignificant which is indicated by microhardness investigations. The same effect was in place, when studying the interaction of liquid copper with steel [5].

Testing for shear of the cladding layer, tearing of the cladding layer and static bending was conducted in order to determine the mechanical characteristics of brass–steel joints. Shear testing of the cladding layer was performed on samples (Figure 8, *a*) which are used for two-layer steels produced by rolling [2]. The thickness of the sample cladding layer was brought to 5 mm by machining. As a result of testing, it was found that the ultimate shear strength of the brass–steel joint produced by heating in autovacuum is equal to 194.2 MPa.

Static tearing tests of the cladding layer were conducted on samples presented in Figure 8, *c*. Here, the die was of such a shape that it ensured tearing deformation in the metal joint zone. The tearing strength limit of the cladding layer was equal to 266.7 MPa.

Static bend testing with cladding layer inside was performed on samples (Figure 8, *b*) of 120×20×8 mm size, die diameter was 16 mm [17]. At 180° bending angle, no cracks visible to the naked eye were found on the sample surfaces.

DISCUSSION OF INVESTIGATION RESULTS

Analysis of the cost of production of a conventional unit of products by arc surfacing, explosion welding and developed technology of heating in autovacuum showed significant cost advantages of the latter. A scheme of the packet positioning at an angle to the vertical with feeding of an additional amount of liquid brass to the cladding layer ensured both obtaining a joint without casting defects or pores, and a high quality of the brass layer surface directly after cladding. Here, the allowance for machining was minimal, metal and labour consumption for machining were also much lower than in other variants.

Metallographic investigations showed that no brittle structures form in the joint zone. The interaction of

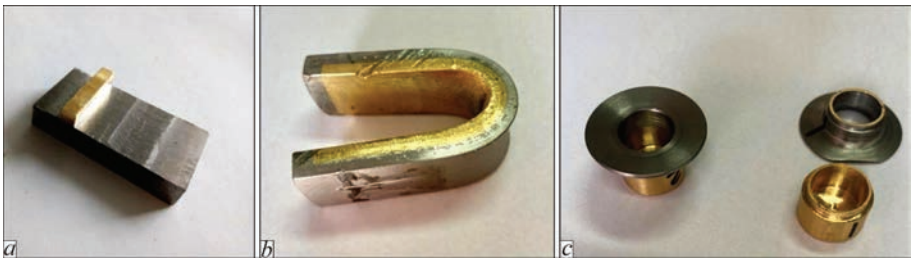

Figure 8. Samples for mechanical testing of brass–steel joints: *a* — shear testing of cladding layer; *b* — two-layer joint after static bend testing with cladding layer inside; *c* — before and after cladding layer tearing tests

liquid brass with steel takes place without cracking in the steel layer. No unfilled tips, or brass penetration into the steel was found, metal composition is close to the initial brass composition with additions of some elements present in the steel. These results correlate well with those of earlier performed studies of liquid copper interaction with steel [5]. No structures with a high hardness form at interaction of steel and brass. The zone of higher hardness of the steel is equal to 3–10 μm. It allows predicting high mechanical properties of the joint and high reliability of the product at operation under the conditions of thermal cycles.

The ultimate shear strength of the brass–steel joint produced by heating in autovacuum was equal to 194.2 MPa, that is by 32 % higher than the normative value (147.1 MPa) [2]. Static bend testing of a two-layer joint with cladding layer inside showed that the joints of metal of the cladding and base layers meet the requirements [6, 2, 16] (out-of-plane bending until sides are parallel, cracks are absent). Tearing strength which was equal to 266.7 MPa, is higher than the normative value by 52 % [10] (177.8 MPa after explosion welding and heat treatment).

CONCLUSIONS

1. A package of engineering works was performed on optimization of the technology of producing a two-layer brass–steel joint by heating in autovacuum. Obtained output data allow developing a production technology with maximal application of the available equipment.

2. Metallographic investigations revealed the high quality of the joint microstructure.

3. Mechanical characteristics of the produced brass–steel joint completely meet the requirements of normative documents for manufacture of tube sheets of shell-and-tube heat exchangers.

4. The performed work is a continuation of investigations of interaction of liquid copper and its alloys with steel at heating in autovacuum. The mechanisms of interaction of the liquid and solid phases published earlier, are completely confirmed in this work.

REFERENCES

1. Kolesov, S.N., Kolesov, I.S. (2007) *Materials science and technology of structural materials*. In: Manual for inst. for higher educ., 2nd Ed., Moscow, Vysshaya Shkola [in Russian].
2. Golovanenko, S.A., Meandrov, L.V. (1966) *Production of bimetals*. Moscow, Metallurgiya [in Russian].
3. (2003) *Handbook on soldering.* Ed. by I.E. Petrunin, 3rd Ed., Moscow, Mashinostroenie [in Russian].
4. GOST 31842–2012. *Shell-and-tube heat exchangers. Technical requirements* [in Russian].
5. Serebryanik, I.P. (2011) *Autovacuum noncapillary structural brazing.* Kyiv, Alfa-Reclama [in Russian].
6. GOST 19281–89. *Rolled steel with increased strength. General specifications* [in Russian].
7. GOST 15527–2004. *Pressure treated copper zinc alloys (brasses). Grades* [in Russian].
8. Bogomolova, N.A. (1978) *Practical metallography*. Moscow, Vysshaya Shkola [in Russian].
9. Perevezentsev, B.N., Krasnopevtsev, A.Yu., Fedorov, A.L. (1991) Study of zinc evaporation in brazing by copper-zinc braze alloys. In: *Abstr. of Pap. of All-Union Sci.-Tech. Conf. on Brazing in Mechanical Engineering, Tolyatti* [in Russian].
10. OST 5.9311–78. *Explosion welding of metals. Bimetallic billets for tube plates of heat exchange apparatuses. General specifications* [in Russian].
11. (1971) *Welding of steel structures.* In: Production of large structures, Issue 20. Ed. by A.I. Volkonsky. Trudy NPI TyaZhMash, Uralmashzavod [in Russian].
12. Shmidt, M., Kuryntsev, S.V. (2014) Producing of bimetal joints by laser welding with full penetration. *The Paton Welding J.*, **4**, 45–48.
13. Suvorin, A.V. (2011) *Electrotechnological installations.* Krasnoyarsk, SFU [in Russian].
14. Poleshchuk, M.A., Atroshenko, M.G., Puzrin, A.L., Shevtsov, V.L. (2014) Estimation of possibility for producing full-strength joint of large steel parts using the method of autovacuum brazing of threaded profile. *The Paton Welding J.*, **10**, 35–37.
15. Vajnerman, A.E. (1981) Mechanism of intercrystalline penetration in surfacing of copper alloys on steel. Avtomatich. Svarka, **6**, 22–29 [in Russian].
16. Serebryanik, I.P., Atroshenko, M.G., Poleshchuk, M.A. et al. (2018) Properties of steel-copper bimetal produced by brazing in autonomous vacuum. *The Paton Welding J.*, **5**, 12–16. DOI: http://dx.doi.org/10.15407/tpwj2018.05.03
17. GOST 14019–2003. *Metallic materials. Method of bending tests.*

ORCID

I.P. Serebryanyk: 0000-0001-8654-1331,
M.A. Polieshchuk: 0000-0020-5992-4641,
T.O. Zuber: 0000-0003-0789-1128,
A.Yu. Tunik: 0000-0001-6801-6461

CONFLICT OF INTEREST

The Authors declare no conflict of interest

CORRESPONDING AUTHOR

M.A. Polieshchuk
E.O. Paton Electric Welding Institute of the NASU
11 Kazymyr Malevych Str., 03150, Kyiv, Ukraine.
E-mail: dep_6@paton.kiev.ua

SUGGESTED CITATION

I.P. Serebryanyk, M.A. Polieshchuk, T.O. Zuber, A.I. Borodin, A.Yu. Tunik, O.A. Los (2022) Characteristics of formation and properties of brass–steel joint produced by autovacuum cladding. *The Paton Welding J.*, **10**, 25–29.

JOURNAL HOME PAGE

https://pwj.com.ua/en

Received: 11.07.2022
Accepted: 01.12.2022

DOI: https://doi.org/10.37434/tpwj2022.10.05

HIGHER CURRENT HARMONICS IN TRANSFORMER POWER SOURCES WITH PULSED DEVICES OF WELDING ARC STABILIZATION

A.M. Zhernosekov[1], **O.A. Andrianov**[2], **S.V. Rymar**[1], **O.F. Shatan**[1], **A.O. Mukha**[1]

[1]E.O. Paton Electric Welding Institute of the NASU
11 Kazymyr Malevych Str., 03150, Kyiv, Ukraine
[2]Ukrainian National Committee of International Chamber of Commerce (ICC Ukraine)
19B Reitarska Str. 01034, Kyiv, Ukraine

ABSTRACT

Transformer power sources of welding arc of industrial frequency alternating current generate into the mains the level of higher current harmonics, which is by an order of magnitude lower by the value of the coefficient of general harmonic distortion, than that of the inverter power sources. Here, their high electromagnetic compatibility with other equipment of the mains is achieved. Moreover, they are much easier to maintain and more reliable. Harmonic composition of current during AC welding was calculated at application of pulsed devices of arc stabilization. It is shown that application of stabilizing pulses with the polarity opposite to that of arc current, is more advantageous that the use of pulses with the polarity coinciding with that of arc current. Advantages as to welding process effectiveness and smaller generation of higher current harmonics are also observed.

KEYWORDS: welding power sources, transformers, welding arc, stabilizing pulses, higher current harmonics

INTRODUCTION

Over the last decades great success has been achieved in development and wide introduction of inverter-type welding arc power sources with digital systems of control and regulation of welding current curve shape. However, application of the welding arc of industrial frequency alternating current is still is demand [1–3]. Alternating current arc is supplied from traditional welding power sources, in which the welding transformer is the main power electromagnetic component. Such modern power sources, fitted with additional block of control of the welding arc and impact on it are widely used in industry.

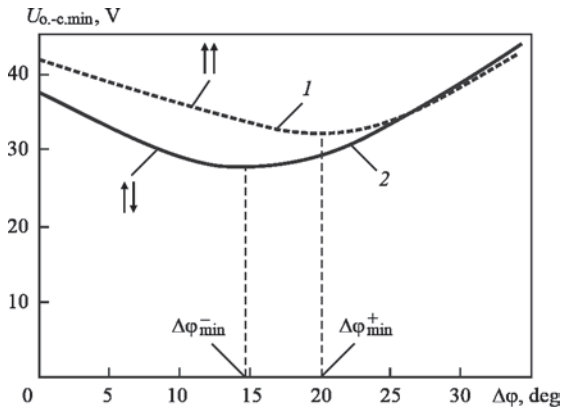

Figure 1. Dependencies of minimal open-circuit voltage of the welding transformer, at which the arc burns, on the difference of phase shift between the welding current and stabilizing pulse: *1* — stabilizing pulse polarity coincides with welding current polarity; *2* — stabilizing pulse polarity is opposite to welding current polarity [3, 6]

Use of pulsed stabilization devices (SD) of arc burning, combined with the traditional AC power sources is a promising direction of applying pulsed impact in AC welding [4, 5]. Application of these devices allows lowering the transformer open-circuit voltage and reducing the consumption of their active materials.

So far there is no single solution on the nature of stabilizing pulse parameters, such as pulse energy, its feeding (injection) time as to the moment of welding current zero crossing, and current polarity. This problem was partially formulated and solved in works [3, 6]. The optimization criterion was selected to be the minimum of power source open-circuit voltage, at which the arc is still stable, and the phase shift difference between the welding current and the stabilizing pulse was the variable parameter. Figure 1 shows the determined dependencies of welding transformer minimal open-circuit voltage, at which the arc is burning, on the difference in phase shift between the welding current and the stabilizing pulse, when the stabilizing pulse polarity coincides with the welding current polarity and it is opposite to welding current polarity. Analysis of the derived curves shows that the dependencies have pronounced minima, and the optimization problem can be solved. One can also see that application of stabilizing pulses of polarity opposite to arc current polarity has an advantage, as the curve of minimum open-circuit voltage $U_{o.-c\,min}$ in this case is located lower than at application of pulses of polarity coinciding with that of the welding current. The following explanation of this fact is given: the

stabilizing pulse is directed opposite to the welding current, it does not interfere with the power source operation and promotes the power source operating as a stabilizing device after the pulse is over.

STATEMENT OF THE RESEARCH PROBLEM

Inverter sources for arc welding have flexible adjustment parameters, and open up wide prospects for their application. However, as shown by experience of industrial application of electric welding equipment, the traditional power sources based on welding transformers still remain in demand [1, 4]. This is attributed, primarily to the reliability of their main power electromagnetic component — the transformer, and to the fact that inverter sources generate a considerable level of higher current harmonics into the mains, have low electromagnetic compatibility [7] and are not as reliable. The traditional power sources generate a much smaller harmonic spectrum into the mains [7, 8]. Moreover, the traditional equipment of AC welding arc is much easier to maintain than the welding inverter power sources, which often supply DC current to the arc. In DC welding the interaction of the arc own magnetic field and the welding circuit field deflects the arc due to magnetic blowing, having extremely negative consequences.

However, the questions of higher current harmonics generation by the traditional AC welding power sources fitted with arc stabilization devices, are still insufficiently studied. Investigations described in this paper address this issue.

The objective of this work is calculation of the current harmonic composition during AC welding by traditional transformer power sources at application of pulsed devices of arc stabilization and analysis of higher current harmonic generation by them.

INVESTIGATION RESULTS

Improvement of the traditional welding power sources follows the path of reduction of welding transformer weight. In these sources stable arc ignition, its burning and welding process stability are associated with high levels of open-circuit voltage. If this is ensured by welding transformer voltage, it leads to an essential increase of its weight. At PWI this problem was solved, in particular, by application of voltage multipliers [9], or arc stabilization devices [10, 11], which allow lowering the transformer secondary voltage.

Investigations of the influence of circuit design solution and regulation methods on external characteristics of the traditional transformer power sources, analysis of the influence of these characteristics on the stability of welding arc burning, as well as investigations of the dynamic processes in AC electric circuits at application of stabilizing pulses is rather fully described in works [3, 6, 12]. Let us focus here on determination and analysis of the harmonic composition of alternating welding current at different circuit solutions and methods of regulation of the characteristics of the traditional welding arc sources.

PWI has accumulated extensive experience of development of different types of pulsed devices of AC arc stabilization. Application of such devices in practice allows improvement of the quality of weld formation, raising the welding process efficiency, promoting power saving and also using more efficient modes and inexpensive electrode for DC welding [5].

TYPICAL POWER COMPONENTS OF AC WELDING POWER SOURCE WITH A PULSED ARC STABILIZATION DEVICE

When designing the traditional power sources, it is rational to select welding transformers with developed magnetic scattering fields. Welding current regulation can be ensured by the design of welding transformer proper, or it can be performed by electric methods, for instance, application of an additional reactor, switched by electronic keys. The advantage of such an electric regulation method consists in that the welding arc powering by current without zero pauses is provided.

Figure 2 gives the electric circuit of welding power source with thyristor regulation of welding current. The source consists of welding transformer Tr, choke L, two back-to-back thyristors VS_1 and VS_2, connected in parallel to it, arc stabilization device (SD), the output of which is connected to arc gap A. Welding transformer Tr includes three windings with turn number w_1, w_2, w_3. Secondary winding w_2 is connect-

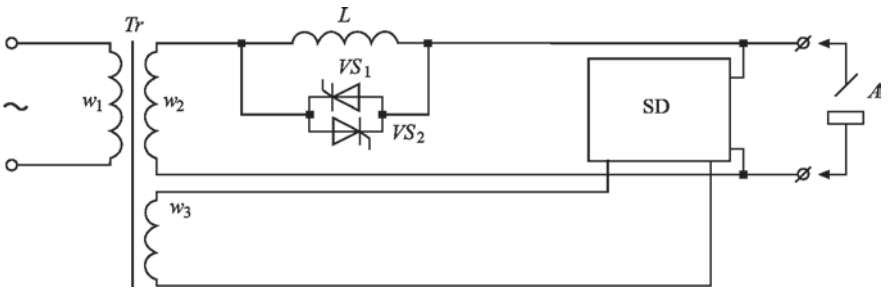

Figure 2. Electric circuit of welding power source with thyristor regulation of welding current

ed in series with choke L and welding arc A. Winding w_3 powers SD.

Each of thyristors VS_1 and VS_2 is connected with a phase shift by angle ψ relative to voltage on winding with turn number w_2. Regulation of the power source welding current is performed by changing angle ψ. The value of the angle remains unchanged ψ = const during the welding process.

At welding current crossing zero, SD generates a current pulse which is fed to the electric arc facilitating its reignition. SD allows lowering the open-circuit voltage in the secondary winding with turn number w_2 of welding transformer Tr, due to lowering of arc ignition voltage.

INVESTIGATIONS OF ELECTROMAGNETIC PROCESSES IN AC POWER SOURCES WITH THYRISTOR REGULATION

Analysis of transient processes in the power source (Figure 2) at welding arc modeling as anti-EMF with arc voltage U_A, is shown in work [6]. We will use these results to calculate the harmonics spectrum.

Figure 3 [6] shows the oscillogram of arc current, its voltage and open-circuit voltage.

The law of welding current variation at the first stage, taking into account the fact that in the initial phase $\varphi_0 = \varphi$ the initial current is equal to zero, $I_0 = 0$:

$$i_1(t) = \frac{U_m}{\omega(L_s + L)}(\cos\varphi - \cos\omega t) - \frac{U_A}{\omega(L_s + L)}(\omega t - \varphi), \quad (1)$$

where U_m is the amplitude value of voltage in the winding with turn number w_2; ω is the angular frequency; t is the time; L_s is the transformer scattering intensity.

From formula (1) not only the law of welding current variation i_1 in the section from φ to ψ, but also the initial effective value of current I_1 for the second switching stage can be determined:

$$I_1 = \frac{U_m}{\omega(L_s + L)}(\cos\varphi - \cos\psi) - \frac{U_A}{\omega(L_s + L)}(\psi - \varphi). \quad (2)$$

The law of welding current variation in the section from ψ up to ψ + α is found from the following expression:

$$i_2(t) = \frac{U_m}{\omega L_s}(\cos\psi - \cos\omega t) - \frac{U_A}{\omega L_s}(\omega t - \psi) + I_1. \quad (3)$$

It is obvious that at the moment of time, when current i_2 becomes equal to I_1, the section with duration $\omega t = \alpha$ ends. Equating the expression for current i_2 at moment of time ψ + α to value I_1 (formulas (2) and (3)), we obtain an equation for determination of switching duration α

$$\frac{U_A}{U_m}\alpha = \cos\psi - \cos(\psi + \alpha). \quad (4)$$

After blanking the respective thyrisor (VS_1 and VS_2), starting from moment of time ψ + α, the law of welding current variation is described by the following expression

$$i_3(t) = \frac{U_m}{\omega(L_s + L)}\left[\cos(\psi + \alpha) - \cos\omega t\right] - \frac{U_A}{\omega(L_s + L)}\left[\omega t - (\alpha + \psi)\right] + I_1. \quad (5)$$

One can see that the right sides of formulas (1) and (5) are identical, so we will use the latter to facilitate further calculations.

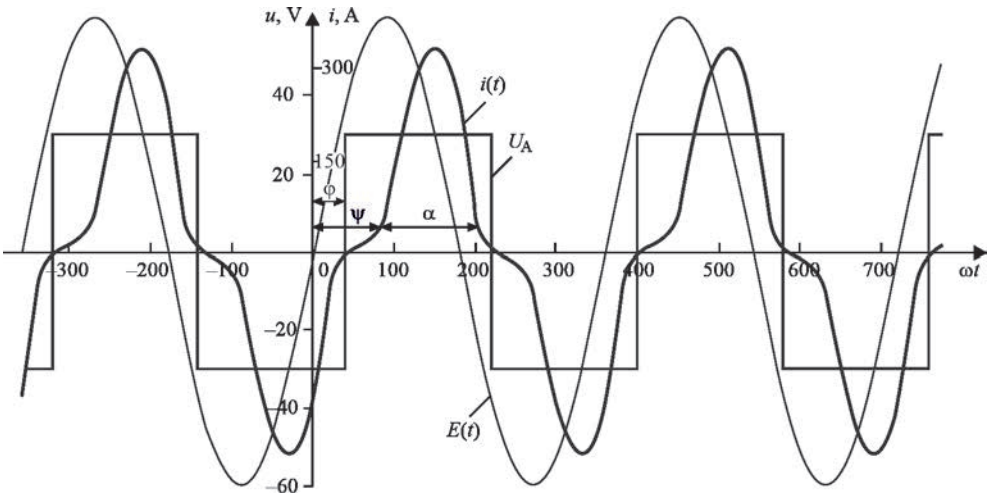

Figure 3. Time dependencies of arc current I_A, arc voltage U_A and open-circuit voltage E

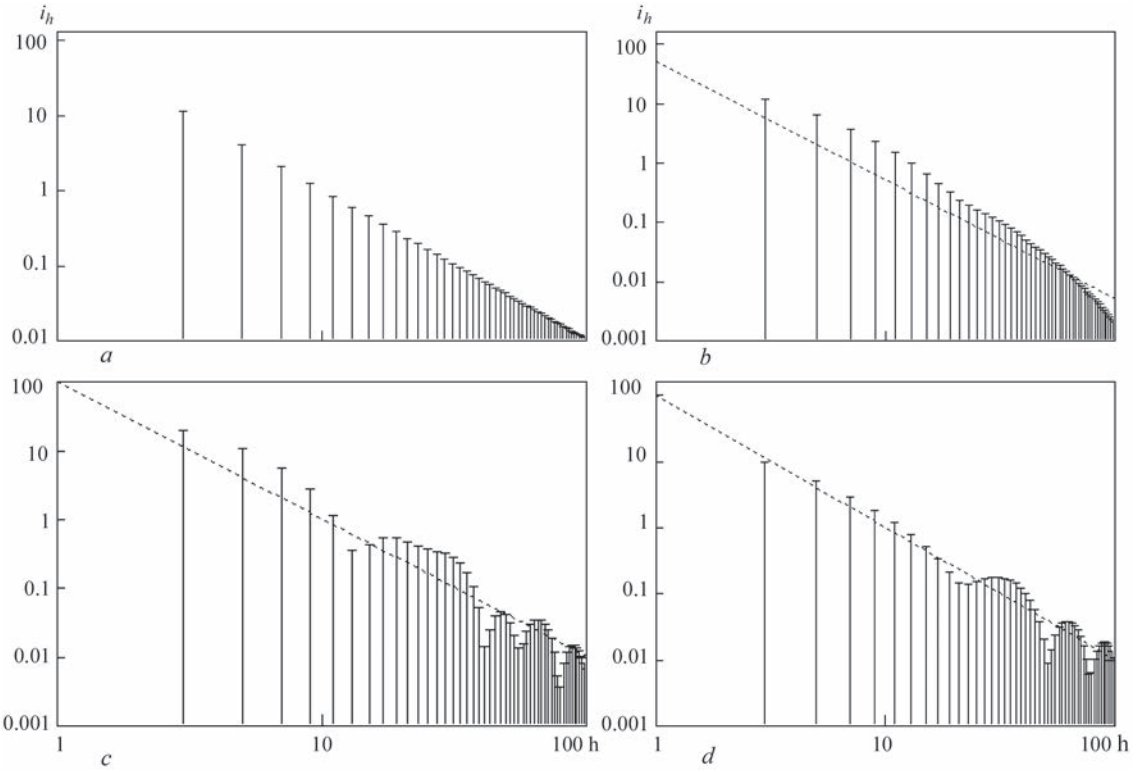

Figure 4. Harmonics composition of welding current $|i_h|$ at arc powering by AC: arc as anti-EMF (*a*): dynamic model of welding arc (*b*); arc with stabilizing pulses, when pulse polarity coincides with arc current polarity (*c*); pulse polarity is opposite to arc current polarity (*d*): *a* — THD_i = 9.1 %; *b* — 9.2; *c* — 15.7; *d* — 7.4

Knowing currents i_1, i_2, i_3, as well as the time intervals of their flowing and setting the angle of switching of thyristors VS_1 and VS_2, we will determine the expression for welding current in the half-period:

$$i(t)=\begin{cases} i_1(t), & \varphi<\omega t<\psi; \\ i_2(t), & \psi<\omega t<\psi+\alpha; \\ i_1(t), & \psi+\alpha<\omega t<\pi. \end{cases} \qquad (6)$$

Having determined the time dependencies of currents at three commutation stages (Figure 3), we can find the harmonics composition of welding current:

$$i(t)=\sum_h^{\infty}\left[a_h\cos(h\omega t)+b_h\sin(h\omega t)\right], \qquad (7)$$

where h is the harmonic number; coefficients

$$a_h=\left[1+(-1)^h\right]\frac{\omega}{\pi}\int_0^{\frac{\pi}{\omega}} i(t)\cos(h\omega t)\,dt;$$
$$b_h=\left[1+(-1)^h\right]\frac{\omega}{\pi}\int_0^{\frac{\pi}{\omega}} i(t)\sin(h\omega t)\,dt, \qquad (8)$$

and current module

$$|i_h|=\sqrt{a_h^2+b_h^2}. \qquad (9)$$

Figure 4 shows the harmonics composition of welding current $[i_h]$ at arc powering by alternating current (arc as anti-EMF). One can see from the figure that even current harmonics are absent.

The coefficient of Total Harmonics Current Distortion (THD) [13] is found by the following formula:

$$THD_i=\frac{\sqrt{\sum_{h=2}^{\infty}|i_h|^2}}{|i_1|}. \qquad (10)$$

The result coincides with harmonics balance method earlier obtained in work [14].

ANALYSIS OF AC ARC STABILITY AND MODELING ITS DYNAMICS

We will study the influence of stabilizing pulses on the welding arc. A peculiarity of this study, based on mathematical modeling method, consists in selection of the dynamic model of the welding arc. The welding arc model in the form of anti-EMF used above for studying the dynamic processes in electric circuits with an arc is unsuitable, as it is essentially static.

The generalized mathematical model of a dynamic arc [15, 16] developed at PWI, provides the most adequate description of electric arc dynamics as an electric circuit element. It takes into account not only the nonlinearity of volt-ampere characteristic, but also the thermal inertia of the arc column. These are exactly the thermal processes, and, primarily, the ionization-deionization process, which affect the con-

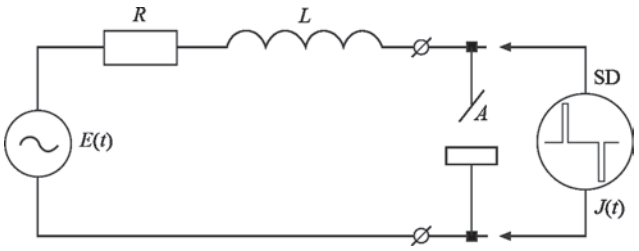

Figure 5. Simplified scheme of power components of the traditional AC welding power sources

ductivity of arc column plasma. The column of 50 Hz AC arc has enough time to deionise at each change of polarity that requires higher voltage to maintain the discharge. If the power source cannot provide the required voltage, the arc is extinguished.

Let us consider an electric circuit (without connection of a pulsed stabilizer) which is shown in Figure 5, and which is a simplified schematic of the power part of traditional AC welding sources connected to arc *A*. A system of differential equations describing this circuit, consists of Kirchhoff's equation and equation of the generalized mathematical model of a dynamic arc

$$L\frac{di}{dt} + Ri + u_A = E(t);\ \theta\frac{di_\theta^2}{dt} + i_\theta^2 = i_A^2, \qquad (11)$$

where i is the current of reactor L and resistor R; $E(t)$ is the power source voltage, having the form of $E(t) = U_m \sin(\omega t - \varphi)$ in the general case; U_m is the open-circuit voltage amplitude; φ is the phase shift angle; i_θ is the current of the arc static state; θ is the characteristic time (time constant of the arc); i_A is the arc current.

In order to find the harmonics composition of the welding current, we will use the results of work [6] and sequence of actions to solve the system of equations (1).

Figure 6, *a* [6] presents modeling results, from which one can see that the shape of arc voltage has pronounced ignition peaks in each half-wave, which exceed the arc voltage. Increased voltage is ensured both by presence of inductance and by phase shifting between arc current and power source voltage.

Knowing the time dependencies of current, we can determine its harmonics composition (see Figure 4, *b*). Although this harmonics composition is different from the spectrum obtained at arc modeling as anti-EMF (compared to Figure 4, *a*) THD_i distortion coefficient practically does not differ.

One of the variants of arc stabilization by current pulses fed from an additional power source, is shown in Figure 5 with connected SD pulsed current source. The system of differential equations which describes transient processes at the pulse stage, follows from system (11), if arc current [3, 6].

$$i_A = i + J(t) = i + J_m \sin \Omega t, \qquad (12)$$

where J_m and Ω are the amplitude and frequency of current pulses.

As one can see from Figure 6, *b* [6] additional pulses lower the arc voltage, which almost does not change during the AC half-wave.

The system stability can be studied, when changing the parameters of the current pulses and the parameters of the main power source. The computer software packages include procedures for integration of systems of regular differential equations. These procedures, however, ensure continuous integration and they are not suitable for integrating systems, where the right parts are different in different time intervals. Their direct application is impossible. Their upgrading, modification and adaptation for this class of problems are required. We will describe a procedure, which was used in these studies.

There is a modified method of shooting and method of multiple shooting to derive periodic solutions in autonomous electric circuits with an arc [17], which can be applied for nonautonomous circuits with an arc. Operation experience [6] showed that reduction of the Cauchy problem to a boundary value problem

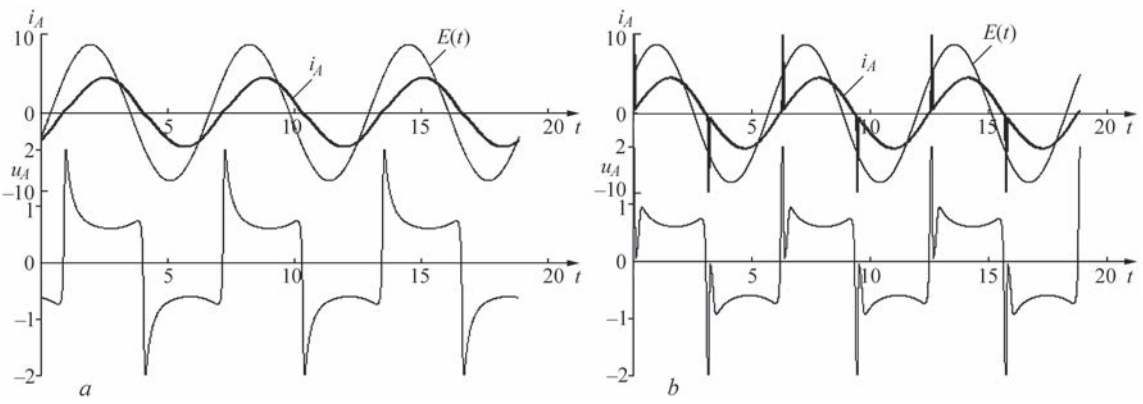

Figure 6. Time dependencies of arc current i_A, arc voltage U_A and open-circuit voltage E obtained as a result of modeling: *a* — without current pulses; *b* — with current pulses

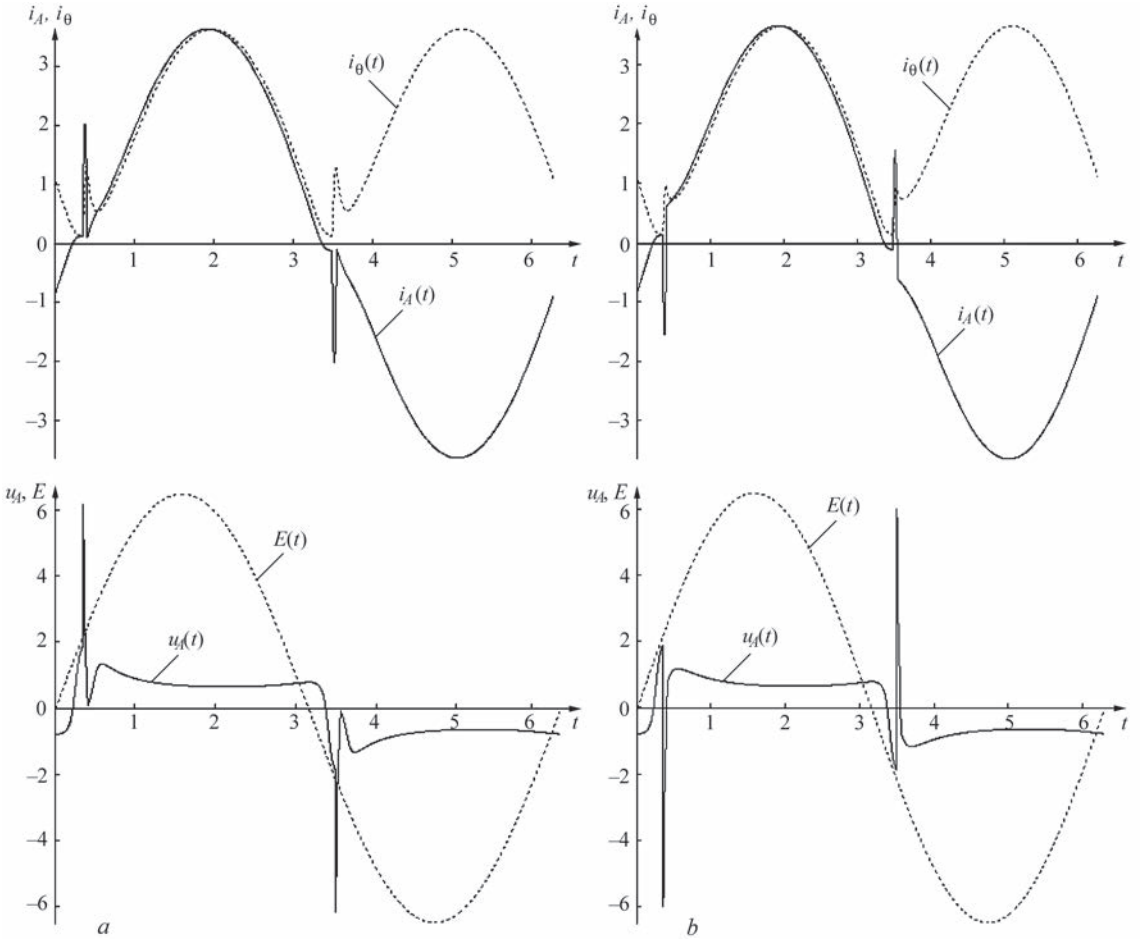

Figure 7. Time dependencies of currents and voltages in a power source with stabilizing pulses: pulse polarity coincides with arc current polarity (*a*); pulse polarity is opposite to arc current polarity (*b*)

with the conditions of half-wave matching at the level of I and I_θ

$$i\left(0,\frac{\pi}{\omega},I,I_\theta\right)=-I;\ \theta\frac{di_\theta^2}{dt}+i_\theta^2=i_A^2, \qquad (13)$$

is unjustifiably cumbersome and requires powerful computing devices (here, $i(t_0, t, I, I_\theta)$ and $i_\theta(t_0, t, I, I_\theta)$ are formal designation of the solution of the system studied by us). This is explained by the need for an additional solution of the variation problem.

Some computer math packages, for instance, MathCAD, allow formally writing the conditions of matching in the half-wave and solving these equations without involving the variational methods. The matching solutions at zero current have the following form:

$$i\left(\varphi,\frac{\pi}{\omega},0,I_\theta\right)=0;\left(\varphi,\frac{\pi}{\omega},0,I_\theta\right)=I_\theta. \qquad (14)$$

here, I_θ and φ are the unknowns to be determined.

This is exactly the path, which is promising due to its simplicity at application of its results for harmonics analysis.

HARMONICS ANALYSIS OF STABILIZATION MODES

Figure 7 shows time dependencies of currents and voltage in the power source with stabilizing pulses [3, 6], derived by the above-given formulas, which coincide quite well with experimentally obtained oscillograms [5]. Figure 7, *a* presents a case when the pulse polarity coincides with arc current polarity, and Figure 7, *b* — when pulse polarity is opposite to arc current polarity.

These time dependencies of current were used to derive by formulas (8) and (9) its harmonics composition, shown in Figure 4, *c*, *d*. Figure 4, *c* gives the harmonics composition of current in the power source with stabilizing pulses, when the pulse polarity coincides with that of arc current, and Fig, *d* shows the case when pulse polarity is opposite to that of arc current.

As was mentioned above, the best is the mode, when the stabilizing pulse polarity is opposite to that of welding current [3, 6]. Its technological effectiveness is confirmed in work [18]. Comparison of Figure 4, *a*, *b*, *d* demonstrates that application of such a mode is more promising also in terms of electromag-

netic compatibility. The level of higher harmonics with THD_i = 7.4 % is lower than of those with THD_i = = 9.1 and 9.2 % for power sources without welding arc stabilizers.

CONCLUSIONS

1. One of the promising directions of application of pulsed impact in AC welding is use of pulsed devices of arc stabilization in combination with AC transformer power sources.

2. Application of stabilizing pulses with polarity opposite to that of arc current prevails. Here, it is possible to obtain minimum weight and size parameters of the power source and achieve high electromagnetic compatibility due to a low level of higher harmonics generated into the mains.

3. Obtained value of the total coefficient of nonlinear distortions of current is lower than the existing standards for power quality. It opens up a prospect for upgrading the currently available and development of new competitive power sources based on welding transformers with pulsed stabilization of the welding arc.

References

1. Zaruba, I.I., Andreev, V.V., Dymenko, V.V. (2001) Improvement of transformers for manual arc welding. *The Paton Welding J.*, **3**, 43–46.
2. Kiji, N., Kobayashi, K., Ishii, J., Yamaoka, H. (2003) Development of high efficiency arc welding methods. *The Paton Welding J.*, **10–11**, 56–60.
3. Andrianov, A.A., Sidorets, V.N. (2009) Optimization of modes for stabilization of alternating-current welding arc. *Elektrotekhnika i Elektromechanika*, **2**, 5–12 [in Ukrainian].
4. Paton, B.E., Zaruba, I.I., Dymenko, V.V., Shatan, A.F. (2006) Lowering of material content of power sources and power consumption in welding. *The Paton Welding J.*, **10**, 15–23.
5. Paton, B.E., Zaruba, I.I., Dymenko, V.V., Shatan, A.F. (2007) *Welding power sources with pulse stabilization of arc burning*. Kyiv, Ekotekhnologiya [in Russian].
6. Andrianov, O.A. (2010) *Optimization of welding stabilization process of corrosion-resistant steels by alternating current*: Syn. of Thesis for Cand. of Tech. Sci. Degree. Kyiv, NTUU KPI [in Ukrainian].
7. Rymar, S.V., Zhernosekov, A.M., Sidorets, V.N. (2011) Effect of single-phase power sources of welding arc on electric mains. *The Paton Welding J.*, **12**, 7–12.
8. Rymar, S.V., Zhernosekov, A.M., Sydorets, V.N. (2011) Influence of welding power sources on three-phase mains. *The Paton Welding J.*, **10**, 40–45.
9. Pentegov, I.V., Latansky, V.P., Sklifos, V.V. (1992) *Small-sized power sources with improved power indices*. Kyiv, PWI, 66–71 [in Russian].
10. Zaruba, I.I., Dymenko, V.V., Kukharsky, V.Ya. (1991) Application of multioperator alternating-current power sources for arc welding. *Avtomatich. Svarka*, **2**, 59–63 [in Russian].
11. Pentegov, I.V., Dymenko, V.V. Sklifos, V.V. (1994) Welding power sources with pulse arc ignition. *Avtomatich. Svarka*, **7–8**, 36–39 [in Russian].
12. Sidorets, V.N., Andrianov, A.A. (2007) Methods of analysis of stabilization modes of alternating-current welding arc. Tekhnichna Elektrodynamika. *Sylova Elektronika ta Energoefektyvnist*, **5**, 71–74 [in Russian].
13. Paice, D.A. (1995) Power electronic converter harmonics. *Multipulse Methods for Clean Power*. NY, IEEE PRESS.
14. Sidorets, V.N., Kunkin, D.D., Moskovith, G.N. (2011) Harmonic analysis of alternating current of electric welding arc. Tekhnichna Elektrodynamika. *Sylova Elektronika ta Energoefektyvnist*, **1**, 219–222, [in Russian].
15. Pentegov, I.V., Sidorets, V.N. (1988) Energy parameters in mathematical model of dynamic welding arc. *Avtomatich. Svarka*, **11**, 36–40 [in Russian].
16. Sidorets, V.N., Pentegov, I.V. (2013) Deterministic chaos in nonlinear circuits with electric arc. Kyiv, IAW [in Russian].
17. Sidorets, V.N. (2006) Method of multiple shooting for the study of bifurcations of dynamical systems. *Elektronnoe Modelirovanie*, 28(**4**), 3–13 [in Russian].
18. Shatan, A.F., Andrianov, A.A., Sidorets, V.N., Zhernosekov, A.M. (2009) Efficiency of stabilisation of the alternating-current arc in covered-electrode welding. *The Paton Welding J.*, **3**, 21–23.

ORCID

A.M. Zhernosekov: 0000-0002-6404-2221,
O.A. Andrianov: 0000-0003-4767-3205,
S.V. Rymar: 0000-0003-0490-4608,
O.F. Shatan: 0000-0001-6553-7421,
A.O. Mukha: 0000-0001-9810-4569

CONFLICT OF INTEREST

The Authors declare no conflict of interest

CORRESPONDING AUTHOR

A.M. Zhernosekov
E.O. Paton Electric Welding Institute of the NASU
11 Kazymyr Malevych Str., 03150, Kyiv, Ukraine.
E-mail: zhernosekov@paton.kiev.ua

SUGGESTED CITATION

A.M. Zhernosekov, O.A. Andrianov, S.V. Rymar, O.F. Shatan, A.O. Mukha (2022) Higher current harmonics in transformer power sources with pulsed devices of welding arc stabilization. *The Paton Welding J.*, **10**, 30–36.

JOURNAL HOME PAGE

https://pwj.com.ua/en

Received: 10.07.2022
Accepted: 01.12.2022

DOI: https://doi.org/10.37434/tpwj2022.10.06

DEPOSITION OF CERAMIC COATING ON THE SURFACE OF A POROUS MATRIX OF INFRARED GAS BURNER

O.V. Kolisnichenko, Yu.M. Tyurin, M.A. Polieshchuk

E.O. Paton Electric Welding Institute of the NASU
11 Kazymyr Malevych Str., 03150, Kyiv, Ukraine

ABSTRACT

A technology is proposed for deposition of a ceramic coating on the surface of Fechral porous matrix to improve the performance of infrared burners. Multichannel detonation device allows forming coatings on the working surface without any significant changes of its surface permeability. Presence of Al_2O_3 ceramic coating on the pore walls changes the burning mode. The flame front moves into the matrix to a small depth behind the coating that leads to reduction of harmful emissions at fuel mixture combustion: carbon monoxide by 50 % maximum, nitrogen oxide by 10–15 %. The effectiveness of matrix radiation increases up to two times in the spectral infrared range of wave length from 5 up to 14 μm.

KEYWORDS: porous metal matrices, infrared radiation, detonation spraying, ceramic coating, harmful emissions, radiation intensity

INTRODUCTION

Application of porous materials in everyday life and in engineering is due to their unique properties. For instance, porous metal matrices have a small weight, combined with a high strength, which allows using them in light structural elements, acoustic insulation, energy absorption system and vibroextinguishers [1]. They also have a large area of inner surface and high heat conductivity, and, thus, are ideally suitable for application as heat exchangers, heat sinks, boilers, burners and reactors for synthesis gas production. High penetrability of porous materials for the gas flow and their huge surface area ensure the high speed of heat transfer at low pressure gradients. At present, manufacture and application of infrared (IR) gas burners is developing intensively due to their high effectiveness. They are used in many technological and household appliances. In them a considerable part of energy from the heater is transferred to the heated object due to radiation. The operation of IR burner is based on complete oxidation of earlier prepared gas-air mixture on a permeable matrix, which radiates thermal energy in IR range at heating. Burning of gas mixtures on the porous matrix surface takes place at a lower temperature, compared to gas flaring due to intensive heat removal from the zone of chemical transformation into the matrix body. The main characteristics of this type of burners are radiation flow density and, which is particularly important for household appliances, low quantity of toxic gases in the combustion products. In order to increase the effectiveness of IR burners, it is very important to ensure complete combustion of the gas mixture and respective lowering of carbon oxide due to longer time of combustion products staying in the high-temperature zone. It can be achieved by application of radiation screens in the form of net or perforated plates over the matrix surface, as well as by the method of gas combustion in the deep cavity of the matrix, or by transition from the topography of a flat to a bulk matrix [2]. Heat-conducting elements are also used in the form of plates, lying on the surface, as well as those penetrating into the matrix body [3]. Such a design of IR burner allows increasing the gas mixture preheating during its movement through the permeable matrix and matrix surface temperature. Heat-conducting plates (recuperators) separate from the combustion products and transfer to the surface and into the matrix body an additional heat flow due to heat conductivity, and also ensure additional heating by radiation from the surfaces of heat-conducting elements, located in the area of the combustion products. Coating of the matrix surface by material with different thermophysical properties also changes the energy and ecological characteristics of the burner device. Moreover, it can be used as an additional measure as to the structural methods of increasing the effectiveness of IR burners. The objective of this work was optimization of deposition technology and studying the structure and properties of a dense ceramic layer on the surface of a porous matrix of a gas burner, as well as testing gas burners with a ceramic coating, determination of the effectiveness of reducing the harmful additive emission and increasing the efficiency.

EQUIPMENT, MATERIALS AND PROCEDURES OF INVESTIGATION

The object of study was a porous matrix of 250×250×10 mm size from Fechral alloy with bulk

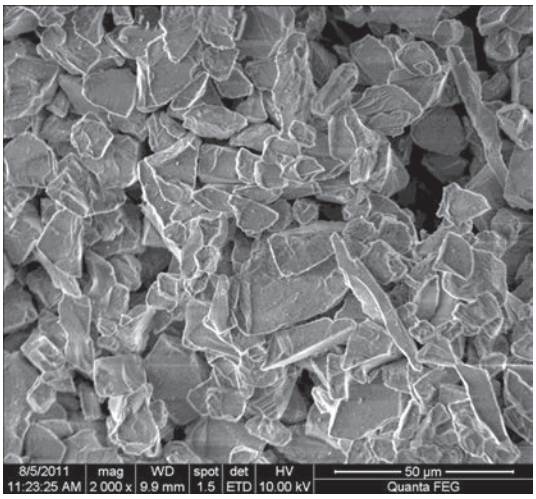

Figure 1. Appearance of AMPERIT® 740.0 Al_2O_3 powder in REM Quanta600 FEG, 10 kV accelerating voltage

porosity $\eta_v \approx 0.9$, surface permeability $\eta = 0.4$ and average pore diameter of 0.5–0.8 mm. Aluminium oxide was selected as the coating material with maximum application temperature of 1650 °C, that is higher than the porous matrix heating temperature during operation. The coating on the working surface and in the matrix pores was formed from AMPERIT® 740.0 Al_2O_3 powder (Figure 1) of H.C. Starck Company (5.6–22.5 μm fraction) by detonation spraying method. Used for this purpose was a multichamber detonation sprayer (MCDS) developed at PWI [4]. Investigations of optimization of the ceramic coating deposition modes were conducted in automated equipment (Figure 2), consisting of MCDS, manipulator, standard low-pressure gas panel (up to 3 atm) for feeding oxygen, propane and air, scraper powder feeder of SX-03-2 type of Guangzhou Sanxin Metal S&T Co., Ltd. (China), and automated system of technological process control.

One of the key parameters, determining the physicochemical processes of material interaction and the actual possibility of high-quality coating formation, is the speed and temperature of the powder particles at the moment of collision with the substrate. With this purpose, the mode of compressed detonation combustion of the gas mixture in specially profiled chambers is realized. The accumulated combustion energy from two chambers in the cylindrical barrel ensures formation of a high-speed jet of detonation products, which accelerates and heats the sprayed powder. Here, the speed of powder, for instance Al_2O_3, reaches 1000 ± 200 m/s [5]. Coating deposition by thermal methods on thin-walled parts is a complicated task, because of the strong thermal impact on the surface. It may lead to intensive overheating, sprayed surfaces oxidation and, consequently, deterioration of adhesion, and usually also destruction of the product proper. The process cyclicity is one of the advantages of the detonation method that allows lowering the spraying zone temperature. Air blowing (6 m^3/h) through the entire back surface of the porous matrix was realized for additional cooling of the product. Gas and powder feeding was continuous. The detonation sequence frequency was 16 Hz, powder consumption was 0.6 kg/h, speed of MCDS longitudinal movement relative to the product was 50 mm/s. The composition and flow rate of the combustible gas mixture components are given in Table 1.

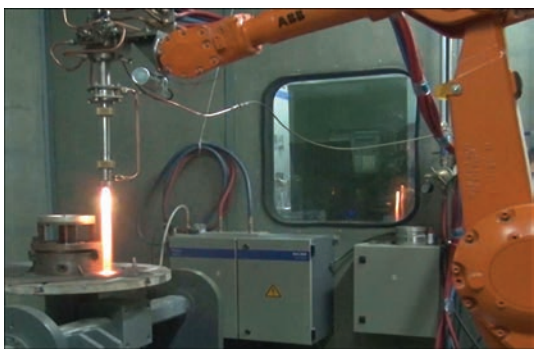

Figure 2. Device for coating deposition using MCDS

Table 1. Composition and flow rate of combustible gas mixture components

Combustible mixture components	Gas flow rate, m^3/h
1st chamber	
O_2	3.9
Air	0.1
C_3H_8	0.71
2nd chamber	
O_2	3.6
Air	0.11
C_3H_8	0.66

Investigations of the microstructure and elemental composition of the layer of Al_2O_3 ceramics were conducted using scanning electron-ion microscopes Quanta 200 3D and Quanta 600 (REM), fitted with energy-dispersive X-ray spectrometer of PEGASUS system of EDAX Company. Porosity was determined by metallographic method with elements of qualitative and quantitative analyses of pore geometry with application of optical inverted microscope Olympus GX51. Investigations of the ceramic layer and substrate hardness were conducted using automated system DM-8 of microhardness analysis by microVickers method at 25 g loading on the indenter.

RESULTS AND THEIR DISCUSSION

Thermal spraying methods are effectively applied to create an impermeable surface layer on porous ma-

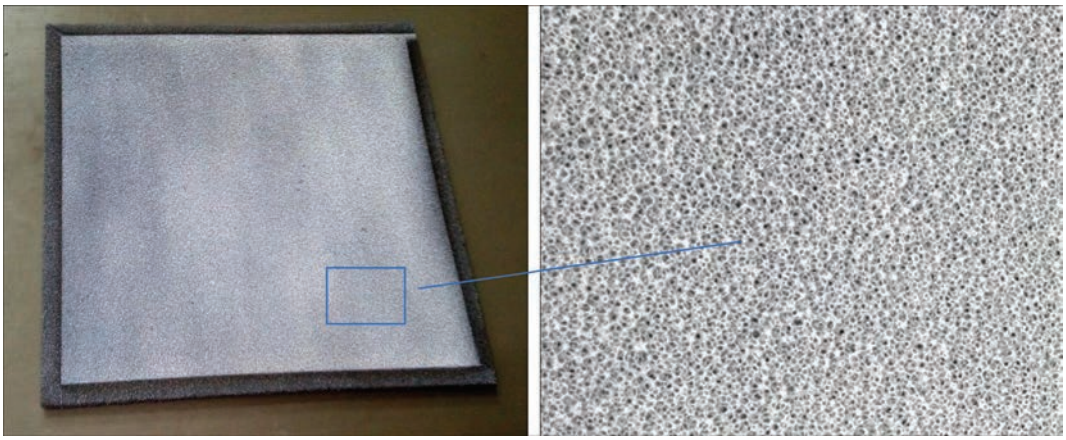

Figure 3. Porous matrix with a coating

trices of heat exchangers [6, 7]. Unlike heat exchangers, the coatings on IR burners must preserve open porosity. As was noted above, one more problems, which comes up during thermal spraying of coatings on thin-walled and laced products is the large heat flow, leading to product overheating. A series of experiments were conducted on determination of the influence of spraying distance on the process of ceramic coating deposition on porous matrices. The distance was varied in the range of 100–200 mm at other technological parameters remaining constant. At 200 mm distance, the powder speed reaches the maximum value at a slight reduction of the maximum temperature of powder particle heating [8]. At large distances, the combustion product temperature and speed also decrease, leading to reduction of gas-dynamic and thermal impact on the thin walls of matrix pores. As a result of the conducted experiments, it was established that at the set technological parameters of spraying with MCDS and additional air cooling the minimal distance from the nozzle edge to the surface, at which no matrix destruction or overheating occurs, is 180 mm. Deposition of the ceramic coating on porous matrices was performed with sixfold overlapping of spraying tracks. Appearance of the coated product is shown in Figure 3.

At spraying the coating follows the surface relief and does not lower the surface permeability of the matrix (Figure 4, *a*). The thickness of the coating on the matrix surface is equal to 100 μm on average. On the matrix transverse fracture one can see that due to reflection from the membranes the coating forms not only on the surface, but also on the walls of the matrix subsurface pores and reaches a thicknesses of 20 μm.

The ceramic layer microhardness is equal to 1320 ± 25 $HV_{0.025}$, porosity is below 2 %. Values of microhardness measurements cross the layer have little discrepancy that is indicative of the homogeneity of the layer of deformed powder particles which closely adhere to each other and also of its phase and structural homogeneity. The coating adheres to the matrix without defects or delaminations. Considering the high-temperature conditions (higher than 1400–1450 °C) of formation of Al_2O_3 coating on the thin walls of the pores, we can state that its phase composition is represented predominantly by α-Al_2O_3 modification [9]. Elemental composition of the matrix and coating material determined by the method of anal-

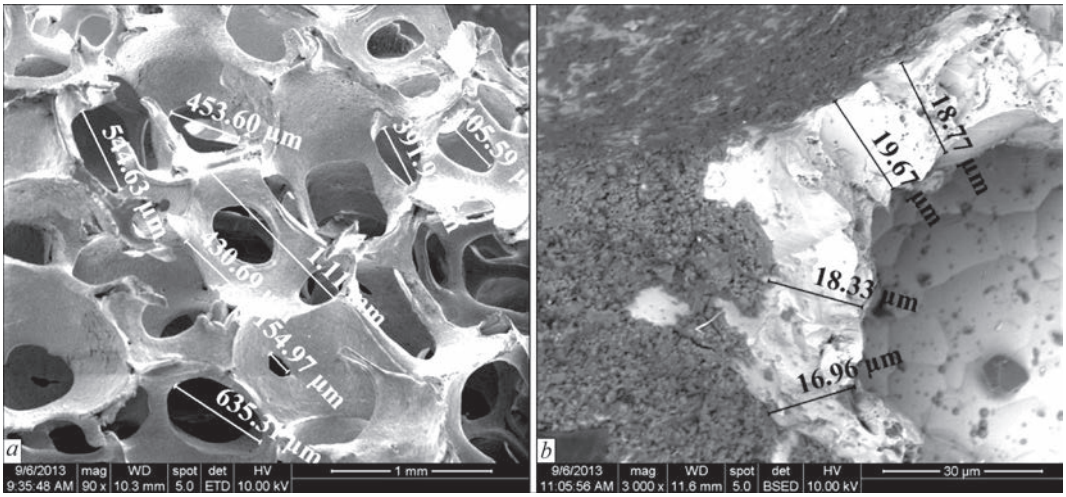

Figure 4. Matrix after spraying: *a* — appearance of surface pores; *b* — coatings on pore walls at 2 mm depth from the matrix surface

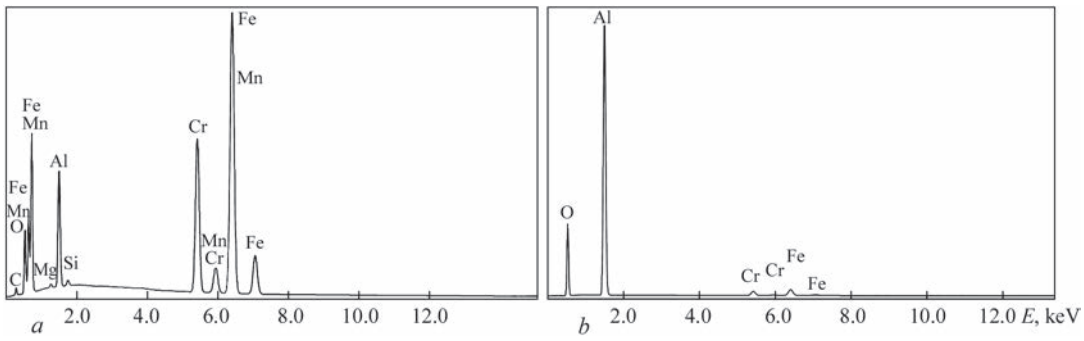

Figure 5. Spectrum of characteristic X-ray radiation of the material of matrix (*a*) and coating (*b*)

Table 2. Elemental composition of a porous matrix and coating, wt.%

Element	Porous matrix	Coating
O	3.57	33.53
Al	9.25	59.27
Cr	20.69	2.43
Fe	64.11	4.78
Mn	1.28	–
Mg	0.34	–
C	0.37	–
Si	0.39	–

ysis of the spectra of characteristic X-ray radiation (Figure 5) is given in Table 2. Heat conductivity of Al_2O_3 coating in the working temperature range of IR burner (up to 1300 °C) is equal to 6 W/(m·K) on average, and that of Fechral material of the porous matrix is 16 W/(m·K). Difference in heat conductivity as shown below, influences the process of combustible mixture burning proper.

Testing porous matrices with and without coating was conducted in work [10]. Combustion of mixtures of natural gas with air on the surface of porous matrices with a ceramic coating was tested at variation of specific thermal load. Radiation temperature of the surface of uncoated and coated areas and the respective temperatures on the matrix reverse side were measured. Visible glow of the surface of initial matrix area without coating was brighter than that of an area with a ceramic coating. However, the area surface temperatures measured by a pyrometer, turned out to be exactly the opposite. The temperature of a surface with a ceramic coating was approximately 200 K higher. Such a significant temperature difference can be explained by that in the coated matrix area the flame front penetrates deeper into the matrix pores as a result of reduction of the coefficient of surface heat conductivity, and the area of contact of the reaction zone with the pore surface becomes larger. The temperature of the matrix subsurface layer rises. The radiation pyrometer records increased temperature, as the ceramic coating is transparent in a broad spectrum of IF radiation. In matrices with a ceramic coating, the flame zone moves into the pores below the matrix surface, and redistribution of energy evolving at gas mixture combustion takes place. The energy radiated by the surface becomes greater. The combustion product temperature and energy carried out by the combustion products, decrease.

Energy redistribution results in increase of the coefficient of radiation efficiency of the burner at ceramic coating deposition. The effectiveness of radiation of a matrix with a ceramic coating is up to 2 times higher in the spectral range of wave lengths from 5 to 14 μm. The amount of harmful emissions in the combustion products is also reduced (carbon monoxide — 2 times, nitrogen oxide — by 10–15 %).

At mixture depletion (increase of excess air coefficient), the temperatures of the surface layer and reverse side of both the matrix areas decrease monotonically that is related to reduction of the mixture calorie content. Here also the temperatures of a matrix with the ceramic coating are higher in the entire range of excess air parameter variation. Thus, unlike the surface burning on a porous metal matrix, a change of burning mode occurs at deposition of a thin ceramics layer on its surface. The flame front penetrates into the matrix to a small depth beyond the coating film, and its temperature grows significantly. Distribution of energy generated due to the combustible mixture burning, takes place. As the temperature of the matrix surface layer becomes higher, it results in enhancement of the radiation flow, and simultaneous lowering of the temperature of the combustion products that should lead to lowering of the rate of formation of nitrogen oxides and carbon monoxide.

In the matrix area with a ceramic coating at a high thermal load, nitrogen oxide formation is reduced 2 times. At the mixture dilution by air the content of carbon monoxide and nitrogen oxides drops monotonically. Close to the boundary of surface combustion at power density of 33 W/cm^2, carbon monoxide concentration is just ~10 ppm, and nitrogen oxide concentration is close to 3 ppm. Experiments showed that owing to ceramic coating, the thermal strength of the matrix increased, the concentration limits of surface combustion became wider that allows extending

the service life of porous metal matrices and reducing the material content of burner devices.

CONCLUSIONS

1. Detonation method with application of MCDS was used for deposition of an aluminium oxide coating on the surface of a porous matrix with preservation of its surface permeability.

2. Presence of a ceramic coating with a smaller coefficient of heat conductivity than that of the matrix material, changes the modes of burning of the combustible gas mixture. The flame front penetrates into the matrix to a small depth beyond the coating layer, improving the performance of IR burners.

3. Application of a porous matrix with a ceramic coating in IR burners allows increasing the burner efficiency and reducing the amount of harmful emissions in the combustion products (carbon monoxide — 2 times, nitrogen oxide — by 10–15 %), and significantly extending the burner operating life.

REFERENCES

1. Srivastava, V.S., Sahoo, K.L. (2006) Metallic foams: Current status and future prospects. *Materials Sci.*, 9(**4**), 9–13.
2. Shmelev, V. (2013) Limiting conditions for the combustion of a rich gas mixture on the surface of a permeable matrix. *Russian J. of Physical Chemistry B*, 7(**1**), 23–34. DOI: https://doi.org/10.1134/S1990793113010120
3. Xiao-Hong Han, Qin Wang, Young-Gil Park et al. (2012) A review of metal foam and metal matrix composites for heat exchangers and heat sinks. *Heat Transfer Engineering*, 33(**12**), 991–1009. DOI: https://doi.org/10.1080/01457632.2012.659613
4. Tyurin, Yu.M., Kolisnichenko, O.V. (2008) *Method of detonation spraying of coatings and device for its realization*. Pat. 83831, Ukraine [in Ukrainian].
5. Kolisnichenko, O.V., Tyurin, Yu.N., Tovbin, R. Efficiency of process of coating spraying using multichamber detonation unit. *The Paton Welding J.*, **10**, 18–23. DOI: https://doi.org/10.15407/tpwj2017.10.03
6. *Salimi* Jazi, H.R., Mostaghimi, J., Chandra, S. et al. (2009) Spray-formed, metal-foam heat exchangers for high temperature applications. *J. of Thermal Sci. and Eng. Applications*, 1(**3**), 031008.
7. Hafeez, P., Yugeswaran, S., Chandra, S. et al. (2016) Fabrication of high-temperature heat exchangers by plasma spraying exterior skins on nickel foams. *J. of Thermal Spray Technology*, 25(**5**), 1056–1067. DOI: https://doi.org/10.1007/s11666-016-0413-9
8. Sun, B., Fukanuma, H., Ohno, N. (2009) The influence of spray parameters on the characteristics of Al_2O_3 particles and coatings sprayed by detonation spray. ITSC 2009. *Proc. of Inter. Conf. on Thermal Spray, May 4–7, 2009, Las Vegas, Nevada*, 830–835.
9. Kovaleva, M., Tyurin, Yu., Vasilik, N. et al. (2013) Deposition and characterization of Al_2O_3 coatings by multi-chamber gas-dynamic accelerator. *Surf. & Coat. Technol.*, **232**, 719–725. DOI: https://doi.org/10.1016/j.surfcoat.2013.06.086
10. Shmelev, V. (2014) Surface burning on a foam metal matrix with the ceramic coating. *Combustion Sci. and Technology*, 186(**7**), 943–952. DOI: https://doi.org/10.1080/00102202.2014.890601

ORCID

O.V. Kolisnichenko: 0000-0003-4507-9050,
Yu.M. Tyurin: 0000-0002-7901-7395,
M.A. Polieshchuk: 0000-0002-5992-4641

CONFLICT OF INTEREST

The Authors declare no conflict of interest

CORRESPONDING AUTHOR

M.A. Polieshchuk
E.O. Paton Electric Welding Institute of the NASU
11 Kazymyr Malevych Str., 03150, Kyiv, Ukraine.
E-mail: dep_6@paton.kiev.ua

SUGGESTED CITATION

O.V. Kolisnichenko, Yu.M. Tyurin,
M.A. Polieshchuk (2022) Deposition of ceramic coating on the surface of a porous matrix of infrared gas burner. *The Paton Welding J.*, **10**, 37–41.

JOURNAL HOME PAGE

https://pwj.com.ua/en

Received: 26.07.2022
Accepted: 01.12.2022

DOI: https://doi.org/10.37434/tpwj2022.10.07

SPECIALIZED PLASMA DEVICES FOR PRODUCING GRADIENT COATINGS BY PLASMA-POWDER SPRAYING

V.M. Pashchenko

National Technical University of Ukraine "Igor Sikorsky Kyiv Polytechnic Institute"
37 Peremohy Prosp., 03056, Kyiv, Ukraine

ABSTRACT

A plasma device for plasma-powder spraying of multilayer, composite and gradient coatings was studied. Experimental studies of energy characteristics of plasma arc generator with curvilinear arc channel were performed during operation in plasma-generating air with the purpose of proving the principal possibility of its long-term service with acceptable energy and life characteristics. It is shown that losses into the plasmatron design elements depend on arc current and plasma gas flow rate, and the nature of this dependence does not differ in principle from regular plasmatrons: the losses increase with a rise in current and somewhat decrease at an increase of gas flow rate. Volt-ampere characteristics of the plasma generator are falling. However, the presence of the arc channel bend as a factor stabilizing the arc length, leads to appearance of a neutral region of VACh with a certain tendency to growth at a current rise. Here, the stable range by arc current operation is limited. A variant of improvement of the studied plasmatron design with widening of its functional capabilities of multicomponent coatings deposition is given.

KEYWORDS: plasma-powder spraying, gradient coatings, multilayer coatings, plasma arc generator with a curvilinear channel, plasma-generating air, volt-ampere characteristics, efficiency, specialized plasma device

INTRODUCTION

A considerable number of parts with coatings of metallurgical, chemical, aircraft and other equipment operate under high loads and sharp fluctuations of ambient temperature. In this case, artificially created functional surface layers of products should retain their properties throughout the entire service life. The chemical composition and structure of coatings and, accordingly, physical and mechanical properties of the material, from which they are created, can differ sharply from the properties of the base material (for example, ceramic coatings on metal bases). Often, there is a problem of violation of the mechanical integrity of the "coating-base" system caused by a sharp difference in the coefficients of thermal expansion (CTE) of materials of the base and the coating. Composite coatings of different functional purpose with metal and ceramic components are also widely used. Moreover, the formation of such coatings occurs from components that are separately fed into the zone of a composite coating formation.

For today, the most widespread methods for creating surface layers of such a type are thermal powder spraying (in particular, plasma) and plasma-powder surfacing [1, 2].

Also, the idea of creating an "adiabate" internal combustion engine has not lost its relevance for today [3]. Creating a ceramic diesel with a heat-insulated combustion chamber (called adiabate) will provide an increase in the efficiency of the engine by 1.5 times and reaching the specific mass (per a unit of power) by almost 30 % less than in the conventional design. Such engines can operate on fuels of broad fractional and deteriorated composition, i.e., they are multifuel, since a high temperature of the combustion chamber's walls contributes to inflammation of hard-flammable fuels. In the course of creating an adiabate engine, along with the use of monolithic parts of ceramics, the use of metal parts with thermal barrier ceramic coatings is provided.

Most often, as a material of thermal barrier coatings (TBC), zirconium and aluminium oxides are used, which is predetermined, first of all, by their low heat conductivity [4]. The working temperature of zirconium oxide coating, which is stabilized by Y_2O_3, is close to 1090 °C. TBC of the new generation based on lantan phosphate and lantan hexoluminate are considered challenging. These materials can operate at temperatures of 1100–1600 °C.

Thermal barrier coatings usually consist of two layers, that perform different functions. The upper layer (ceramic) perceives thermal and erosion effects of gas flow and, having a low thermal conductivity, reduces the temperature of a part, that is protected. Under the ceramic layer, a heat-resistant layer is located, which protects the base from oxidation and helps to increase the adhesion strength of the ceramic layer with the base metal. An additional decrease in heat conductivity of ceramic coatings can be reached by their multilayered deposition.

The use of an intermediate layer of a metal material partially solves the problem of harmonization of CTE materials of the base and a functional coating, but a complete solution is possible only in case of gradual transition from CTE of the base material to CTE of the upper coating layer material. The transition can be realized in a step way by increasing a number of transition layers with a variable value of CTE [4, 5], or in the form of a coating with a smooth change in physical properties of the coating material in the direction from the base to the surface of a product. Such coatings are positioned as gradient.

Creating a gradient coating is possible by using already prepared mixtures of the base functional coating (ceramic) and the underlayer material [4, 5]. Such ready mixtures have a variable proportion between components. First, a coating layer, consisting of only a metal component is deposited, and then subsequent layers are deposited of ready mixtures, in which the content of a ceramic component gradually increases. The most upper functional coating layer contains only a ceramic component. Such a method guarantees the necessary ratio between components in each layer, but it requires the presence of several feeding dispensers (according to a number of layers), which are switched on in series, or refilling the powder with a new ratio of components of a one dispenser (with mandatory cleaning from the previous powder).

The more challenging way is the use of a complex of the equipment, containing a such number of dispensers, that is equal to a number of components of the composition in the future coating (in the simplest case there are two of them) [6].

The operation of such feeding dispensers is realized at the same time according to a certain algorithm, which determines the efficiency of operation of each one. The control (changing the ratio between components in a gas-powder flow) can be carried out in the function of time, if it is possible to accurately determine the thickness of the layer being deposited by the efficiency of the dispenser and the coefficient of using the material, or in the function of a number of passes, if the thickness of a coating produced in a one pass is known. The control is also possible if hardware devices for in-process determination of the coating layer thickness are used. The implementation of the algorithm requires a microprocessor control unit that has a feedback from the coarse of the coating formation process.

Another problem in the realization of technology of depositing gradient coatings is to organize the process of heating the source material, which contains components with sharply different physical properties. Taken into account a significant spatial heterogeneity of temperature, concentration and high-velocity fields of high-temperature gas flow, it is almost impossible to determine one place of introducing components of the source material that would provide optimal conditions for heating and accelerating of both metal as well as ceramic component (needless to say about protection of the material from the undesired effect of active gases from the environment). The ceramic component of the source material requires high temperature and comparatively long-term stay in the active area of the plasma jet. The metal component provides protection against oxidation and restriction of the intensive evaporation process by minimizing the time of staying in the region of ultra-high temperatures.

Considering that the most common way to introduce the source material into the plasma jet is introducing it outside the plasma generator design, the wide opportunities for optimizing the conditions of heating and accelerating the powder are not provided by the designs of modern sprayers. The introduction of the source material (for the ceramic component) at an angle directly into the arc channel significantly reduces the reliability of the process because of the high probability of sticking the material on the walls of the arc channel and the emergency operating modes of the plasmatron. In addition, the reliability of the design decreases due to the need to pass the water jackets for cooling the heat stressed elements of the plasma generator design [6].

It is impossible to feed the source material coaxially with the plasma jet due to the presence of the central water-cooled electrode in the arc generators of a linear circuit [7].

The aim of the work is to prove a fundamental possibility of creating a new generation of plasma devices for deposition of coatings of a complicated structure — multilayered and gradient from materials with substantially different physical and mechanical properties on the base experimental results of arc burning.

PROCEDURE OF EXPERIMENTS

The studies were conducted in a two-electrode plasmatron with the arc channel, consisting of several sections placed at an angle to each other. The spatial stabilization of the arc is of eddy type.

As a plasma-generating substance, air and a mixture of air with propane-butane was used. The gas mixture was preliminary prepared and supplied into the plasma generator already with a known components ratio.

The electric parameters of the device (arc voltage and arc current) were measured by electron and pointer instruments.

The losses into the plasma generator design elements were determined by measuring the flow rate of cooling liquid and its temperature at the inlet and outlet of cooling circuits of the corresponding units. The temperature was measured by mercury laboratory thermometers with a division value of 0.1 °C.

RESEARCH RESULTS AND DISCUSSION

The known direct methods for deflection of the flow from the axis of the arc channel by applying angular nozzles [7] allow deflecting the jet to a certain angle by changing the direction of leakage of an already formed jet. Such a method has a significant drawback — deflection of the plasma jet at the stage of a developed turbulent flow causes a sharp increase in thermal losses into the nozzle wall at the place of rotation of the plasma jet, which deteriorates the energy parameters of the plasmatron and significantly shortens the life of an initial electrode.

This disadvantage can be eliminated if the plasma jet can be turned at the stage of its formation. For this purpose, the arc channel is produced of two parts joined between each other at some angle. Under these conditions, most of the main region of the arc is placed on the inlet, and the smaller part of the main region of the arc and its near-electrode region is on the outler region of the arc channel, at an angle to the initial and main regions of the arc [8].

Such a burning organization of the arc allows protecting the walls of the arc channel to some extent at the point of changing the direction of movement of the gas flow from the heat of the heated part of the gas by means of the cold layer of gas between the channel wall and the electric arc, stored at the mentioned stage of a plasma jet formation and not fully formed plasma jet.

Figure 1 shows the variant of the device for implementation of the described method.

The output electrode of the device, in which the arc channel is placed, consists of two designing units, fixed together. Each characteristic region of the arc channel is located within its design unit and has an individual independent cooling system. The inlet area of the arc channel is characterized by a relatively low level of thermal losses [7]. Therefore, the unit in which it is located may have air cooling (natural or forced). Within the frames of the same unit, the angular transition of the inlet region of the arc channel to the initial region of the outlet arc channel is located and the powder line passes.

The end region of the outlet arc channel usually has water cooling. In order to rationally use the volume of material and increase the overall life of the output electrode, in the outlet part of the output electrode a number of channels are made, each of which, under certain conditions, can serve as the end region of the outlet arc channel. Under specific conditions, only one of the channels, in which the inlet hole coincides with the outlet hole of the initial region of the outlet arc channel, serves as the end region of the outlet arc channel. All other channels are reserve and sequentially involved in operation when the position of the outlet part of the output electrode relative to its inlet part changes.

The experimental studies of the mock-up of the plasma sprayer, created according to the proposed scheme, showed the technical serviceability of the design in the case of operation at current loads typical for plasma spraying and the use of plasma-generating mixtures of the N–O or N–O–C–H system. The study

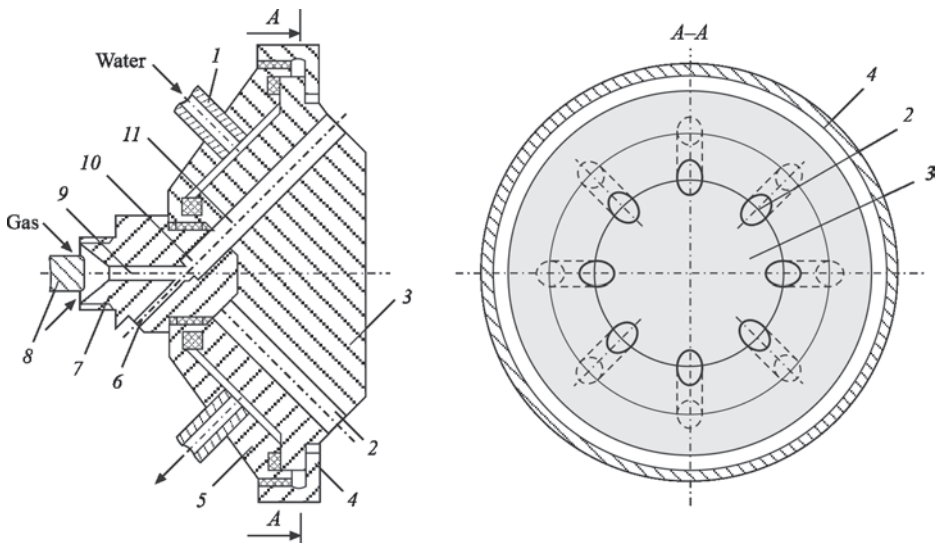

Figure 1. Plasmatron with assembled arc channel: *1* — fitting pipe; *2* — regions of arc channel; *3* — outlet part of the anode; *4* — captive nut; *5* — body part; *6* — powder feed channel; *7* — inlet part of the anode; *8* — cathode; *9* — inlet part of the arc channel; *10* — initial region of the outlet part of the arc channel; *11* — end region of the outlet part of the arc channel

of energy characteristics was carried out in the existing mock-up of the sprayer (Figure 2).

To power the plasmatron, a thyristor current source of APR-402 type was used which stabilizes the arc current in the range of 100–450 A when the operating voltage changes from 100 to 250 V.

The cathode unit and the outlet part of the arc channel within the anode had a direct water cooling, and the inlet part of the arc channel had a natural air cooling.

Variable operating parameters of the plasmatron were the consumption of plasma-generating air (gas pressure in front of the sprayer) and the arc current.

The main results of the experimental studies are shown in Figures 3–5.

The value of the arc voltage is determined by the arc current and the consumption (pressure) of the plasma-generating gas. As the gas flow increases, the arc lengthens and, accordingly, the integral value of the voltage drop on it increases. As the current increases, the arc shortens and the voltage drop becomes lower (Figure 3).

A characteristic feature of the investigated plasmatron is the fact that at a current above 170–180 A, a neutral region of the static volt-ampere characteristics (VACh) with a tendency of transition to a growing arc current above 220–230 A is observed.

Obviously, this is a consequence of fixing the length of the arc at the turn of the arc channel in a certain range of changes in the current and consumption of plasma-generating gas. The beginning of the process of stabilization of the arc length depends on the consumption of plasma-generating gas — the lower the consumption, the lower the threshold value of the current, at which the stabilization of the arc length begins.

Figure 2. Plasmatron with curvilinear arc channel

An increase in the current to the level of 270–300 A leads to the transition to an emergency mode of the plasma generator operation, which is characterized by a jump-like shortening of the arc with its pulling into the narrow part of the arc channel. This mode of the plasmatron operation is characterized by increased energy losses at the initial region of the arc channel. And taking into account that this region in the particular case has a natural air cooling, this will lead to overheating of the electrode material and a sharp acceleration of its erosion process.

Figure 4 shows the dependences of the losses into the anode unit of the plasmatron on the operational parameters of the device.

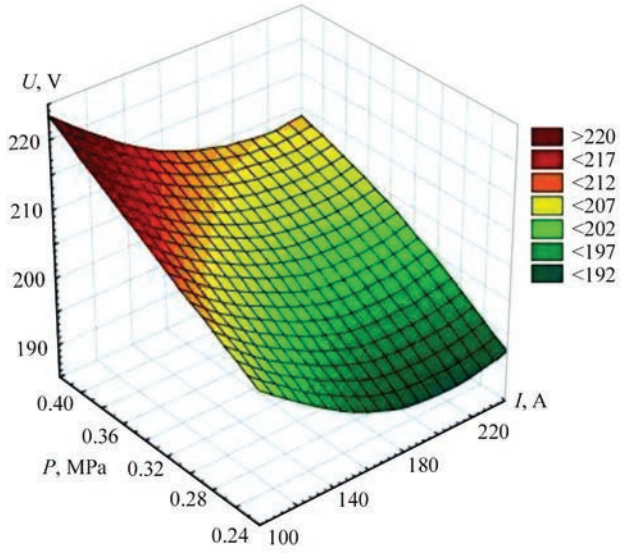

Figure 3. Volt-ampere characteristics of plasma sprayer

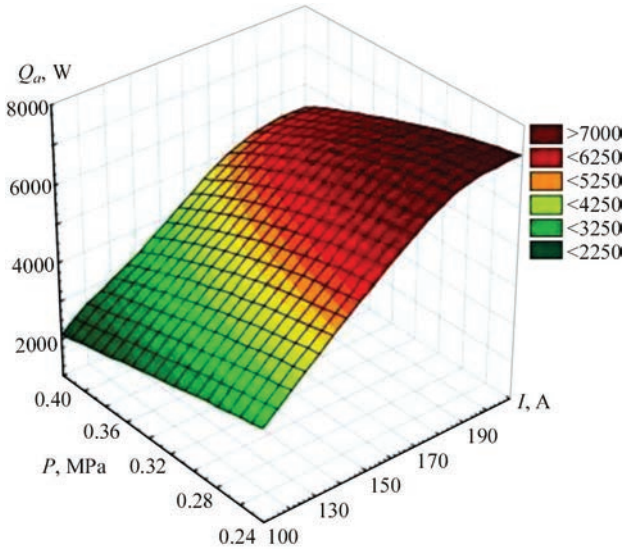

Figure 4. Dependence of energy losses into the anode unit of the plasma generator on arc current and pressure of plasma-generating gas

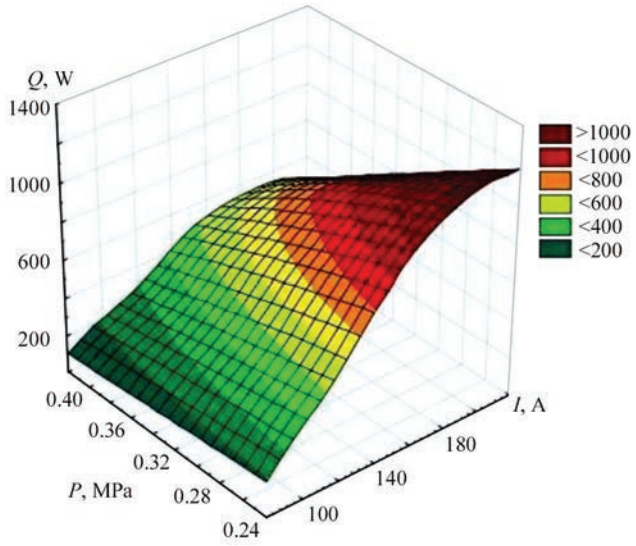

Figure 5. Dependence of energy losses into the cathode unit of the plasma generator on arc current and pressure of plasma-generating gas

Energy losses into the inlet part of the arc channel (region with a smaller diameter) during normal operating modes are practically determined by heat losses through arc radiation, therefore they decrease with a drop in current and an increase in the consumption of plasma-generating gas due to a decrease in the average mass temperature of the plasma.

The losses into the outlet part of the arc channel are mainly determined by the arc current. Simultaneously, with an increase in the consumption of plasma-generating gas, as a result of thickening of the cold gas interlayer between the arc and the wall of the arc channel and the reduction in the region of a developed turbulent flow of a high-temperature gas flow within the ranges of the arc channel, the total level of losses into the output electrode decreases slightly.

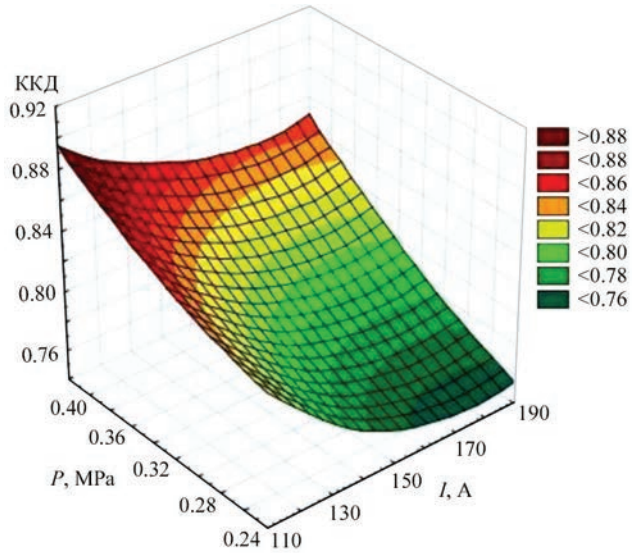

Figure 6. Dependence of the plasmatron efficiency on arc current at different pressure values of plasma-generating gas

The losses into the cathode unit increase as the arc current grows under the condition of a constant consumption of plasma-generating gas, and decrease slightly when its consumption increases (Figure 5). An increase in the consumption of cold plasma-generating gas intensifies the process of heat removal from the design elements of the cathode unit due to intensive blowing of the outer surface of the thermochemical cathode and its attachment unit. Under these conditions, recovery of a part of the energy of the electric arc occurs, which is not lost, but is used for preheating of the plasma-generating gas.

The thermal efficiency of the plasmatron, calculated from the measured energy losses, in this particular case has quite high values in the entire range of arc current changes. Although it should be taken into account that the presence of a region with natural air cooling in the output electrode, the losses into which are not taken into account in the calculations, gives slightly overestimated values of the calculated efficiency (Figure 6).

As the arc current grows, there is a decrease in the efficiency value, but, starting from current values of 160–170 A, a slowdown in the rate of a decrease in the efficiency and its stabilization at the level of 0.76–0.8 is observed. It should be noted that high efficiency values of 0.8–0.86 are typical for the operation of a plasma generator with an increased consumption of plasma-generating gas. Such modes of operation are usually not typical for coating processes due to low values of the specific energy of the high-temperature gas flow.

In the case of using a plasmatron as a sprayer of dispersed material with the introduction of powder together with the transporting gas coaxially with the outlet region of the arc channel, a change in the burning conditions of the electric arc and the nature of the heat exchange with working gases should be expected. The transporting gas takes an active part in the formation of the plasma flow, because it is supplied to the area of the electric arc. The location of the arc binding spot in this case will also partially depend on the consumption and composition of the transporting gas. Whereas the shape and nature of the arc binding spot will depend in a certain way on the composition of the transporting gas with the potential possibility of transition to diffusive arc binding under certain conditions.

The presence of the arc channel region with air cooling in the plasmatron makes it possible to lay the powder line through the anode unit without crossing its cooling jackets (see Figure 1). However, only two variants for feeding components of the composite material remain practically real: at the place of bend-

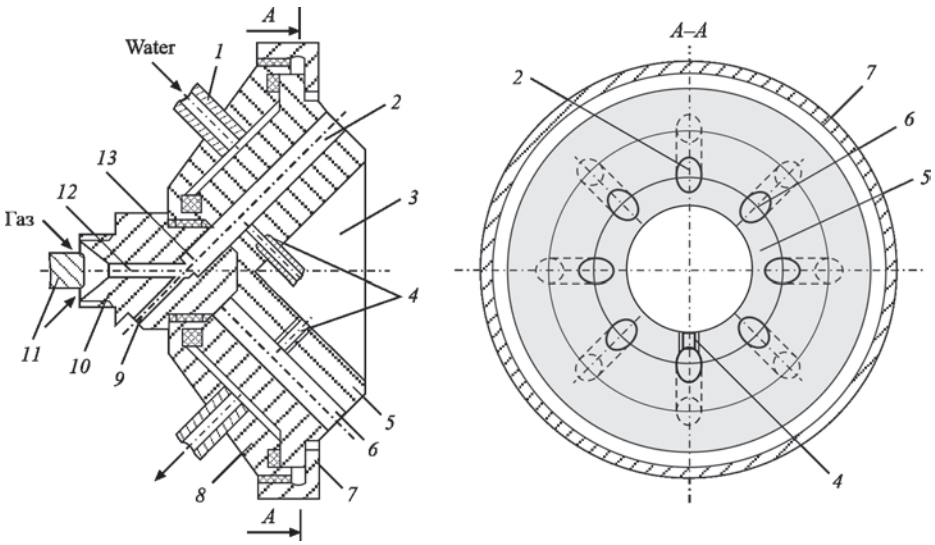

Figure 7. Design of plasma generator for deposition of multicomponent coatings: *1* — fitting pipe; *2* — end region of the outlet part of the arc channel; *3* — cavity; *4*, *9* — powder feed channels; *5*—— outlet part of the anode; *6* — regions of the arc channel; *7* — captive nut; *8* — body part; *10* — inlet part of the anode; *11* — cathode; *12* — inlet part of the arc channel; *13* — initial region of the outlet part of the arc channel

ing the arc channel (under condition that air cooling is used) and outside the arc channel at the section of the sprayer nozzle. All other require crossing of the electrode cooling jackets and the corresponding complication of the design with the loss of the device reliability. This in a certain way limits the possibilities of technology optimization by changing the place of introduction of individual components of the source material into the high-temperature gas flow in order to take into account their physical and geometric characteristics.

The further improvement in the design of the studied plasma generator largely solves the mentioned problem and allows creating a specialized plasma device with wide functional capabilities for applying multilayer and gradient coatings (Figure 7). For this purpose, in the output electrode (anode), a cone-shaped cavity is created, on the surface of which the inlets of the channels for feeding dispersed material are located. The channels are connected with the corresponding end regions of the arc channel. In this case, the location of each channel and the place of its connection with the arc channel are determined by a difficulty in melting of the used material and may be different for the available end regions of the outlet arc channel (in the specific case, there are 8 such sections).

The device shown in Figure for deposition of a multilayer composite coating consists of three structural units fixed to each other. Each characteristic region of the arc channel is located within its designing unit and has an individual independent cooling system. The inlet region of the arc channel is characterized by a low level of heat losses. Therefore, the unit in which it is placed, can have (under certain conditions) air cooling (natural or forced). Within the same unit, the angular transition of the inlet region of the arc channel to the initial region of the outlet arc channel is located and the powder line passes. Usually, the end region of the outlet arc channel has water cooling and is placed at an angle to the longitudinal axis of the outlet part of the output electrode. For the rational use of the material volume and to increase the overall life of the output electrode, a whole number of channels was made in the outlet part of the output electrode, each of which, under certain conditions, can serve as the end region of the outlet arc channel. In a specific case, only one of the channels, in which the inlet hole coincides with the outlet hole of the initial region of the outlet arc channel, serves as the end region of the outlet arc channel. All other channels are reserved and are sequentially involved in operation when the position of the outlet part of the output electrode changes relative to its inlet part of the output electrode. A possible number of channels is determined based on the design, taking into account the mandatory presence of a wall of a certain thickness between adjacent channels, necessary for effective heat removal deep into the output electrode. At the end of the output electrode, a cone-shaped cavity is made, on the surface of which the holes are located. The holes are connected with the outlet regions of the arc channel. The inlet place of the holes into the outlet regions of the arc channel is determined taking into account the melting point of a specific component of the composite material from which the coating is formed. A refractory component of the composite material can be introduced in the transition area from the inlet region

of the arc channel to the initial region of the outlet arc channel. The direction of the initial movement of the powder particles and the plasma flow coincide, so a refractory component will not have a radial component of velocity (relative to the longitudinal axis of the arc channel) and will be in the high-temperature zone for the maximum possible time. All other components of the coating material can be introduced through the holes placed at different distances from the section of the nozzle of the plasma device. The choice of the working channel from the entire set of the channels is made based on the melting point and dimensions of the second component of the composite material. These criteria determine the location of joining the powder line with the arc channel of the plasma device and, accordingly, the choice of one or another reserve region.

The arrangement of channels for feeding powder on the surface of the inner central conical cavity does not require crossing the cooling jacket of the output electrode, because the water cooling of the electrode occurs only on the side of its outer surface.

In case of transition to spraying of another composition of materials, it is possible to replace the channel with one of the reserve ones, which is more suitable for feeding new component of the composite material. In the case of a long-term spraying of one composition, the reserve channels are made identical from the point of view of the place of the powder line location. In this case, the presence of reserve channels allows stabilizing the quality of the coating and increasing the overall life of the device. In order to prevent the deterioration of the quality of the coating and the efficiency of the spraying process when the geometric dimensions and configuration of the arc channel change due to the erosion of the electrode material, the outlet regions of the arc channel are periodically replaced.

CONCLUSIONS

1. The use of plasma generators with a curvilinear arc channel is rational in the case of creating multilayer composite coatings with components that differ sharply in their physical and mechanical characteristics.

2. The complex configuration of the arc channel somewhat limits the range of steady operation of the plasma generator in terms of the arc current and consumption of the plasma-generating gas mixture.

3. The general nature of dependences of the energy characteristics of a plasmatron with a curvilinear arc channel on the basic mode parameters is identical to similar dependencies for traditional plasma generators with a rectilinear arc channel.

4. The influence of operating modes of plasma generators with a curvilinear arc channel on their life characteristics requires further studies in order to establish rational operating modes.

REFERENCES

1. Som, A.I., Galaguz, B.A. (2020) Plasma transferred arc surfacing of composite alloys with separate feed of tungsten carbides and matrix alloy. *The Paton Welding J.*, **12**, 34–39. DOI: https://doi.org/10.37434/tpwj2020.12.05
2. Borisov, Yu.S., Borisova, A.L., Grishchenko, A.P. et al. (2019) Structure and phase composition of ZrB_2–SiC–AlN plasma coatings on the surface of C/C–SiC. *The Paton Welding J.*, **5**, 18–27. DOI: http://dx.doi.org/10.15407/tpwj2019.05.03
3. Matskerle, Yu. (1987) *Modern economy car*. Ed. by A.R. Benediktov. Moscow, Mashinostroenie [in Russian].
4. Borisova, A.L., Borisov, Yu.S., Astakhov, E.A. et al. (2012) Heat-protecting properties of thermal spray coatings containing quasi-crystalline alloy of the Al–Cu–Fe system. *The Paton Welding J.*, **4**, 31–36.
5. Matsuka, N.P., Gromyka, G.F., Shevtsov, A.I., Iliyushchenko, A.F. (2019) *Modeling of nonstationary thermal processes in formation of gradient thermal coatings based on self-fluxing alloy modified with solid refractory compounds under pulsed high-energy action*. Minsk, Erugiskie Chteniya-2019, 88–89 [in Russian].
6. Zajtsev, O.V. (2008) *Development of materials for protection of aircraft engine parts from high-temperature erosion*: Syn. of Thesis for Cand. of Tech. Sci. Degree, Dnipropetrovsk [in Ukrainian].
7. Pashchenko, V.M. (2018) *Arc generators in surface engineering technologies.* Kharkiv, Machulin [in Ukrainian].
8. (2009) *Device for formation of gas-powder flow in plasma spraying.* Pat. Ukraine 42589. Int. Cl. B05B 7/00, H05H 1/00 No. 200901606; Fill. 24.02.2009; Publ. 10.07.2009 [in Ukrainian].

ORCID

V.M. Pashchenko: 0000-0003-3742-6913

CORRESPONDING AUTHOR

V.M. Pashchenko
National Technical University of Ukraine “Igor Sikorsky Kyiv Polytechnic Institute”
37 Peremohy Prosp., 03056, Kyiv, Ukraine.
E-mail: vn.paschenko@ukr.net

SUGGESTED CITATION

V.M. Pashchenko (2022) Specialized plasma devices for producing gradient coatings by plasma-powder spraying. *The Paton Welding J.*, **10**, 42–48.

JOURNAL HOME PAGE

https://pwj.com.ua/en

Received: 31.08.2022
Accepted: 01.12.2022

DOI: https://doi.org/10.37434/tpwj2022.10.08

PLASMA-CHEMICAL PROCESS OF OBTAINING NANOSILICON FOR LITHIUM-ION BATTERIES

S.V. Petrov[1], **S.G. Bondarenko**[2], **Sato Koichi**[3]

[1]The Gas Institute of the NASU
39 Degtyarivska Str., Kyiv, Ukraine, 03113
[2]National Technical University of Ukraine «Igor Sikorsky Kyiv Polytechnic Institute»
37 Peremohy Prosp., 03056, Kyiv, Ukraine
[3]Kankyo Techno Co. LTD Japan. 959-2633 Niigata pref. Tainai city Sekizawa 69-5

ABSTRACT

The process of complete plasma evaporation of the initial solid material for the synthesis of Si nanoparticles as applied to lithium-ion batteries and energy storage devices was studied in this work. The use of numerical modeling methods made it possible to determine the flow parameters of a two-phase high-temperature flow — temperature fields, velocities and concentrations. To study the processes of evaporation and subsequent synthesis of nanopowders, a plasma reactor with an electric arc plasmatron with a linear circuit and using an argon-hydrogen mixture as a plasma-forming gas was developed. The influence of the external magnetic field on control of the plasma jet parameters was studied in a series of experiments using an electric arc plasmatron in plasma laboratory installations of 30 and 150 kW power. The influence of the magnetic field on the configuration, geometric dimensions and structure of the initial section of the plasma jet was determined. The initial dispersed material — silicon powder was fed to the section of the plasmatron nozzle in a radial pattern. Experimental confirmation of the phenomenon of elongation of the high-temperature initial section of the plasma jet in an axial magnetic field was obtained. It was experimentally established that the creation of a peripheral gas curtain significantly improves the characteristics of heat and mass transfer in the reactor. The influence of two-phase flow, heat exchange and mass flow of nanoparticles, including on the surface of a plasma reactor with a limited jet flow, in the processes of obtaining silicon nanopowders was studied. The obtained regularities can be used to develop and put into operation a pilot plant for high-performance production of nanosilicon powders.

KEYWORDS: plasma-chemical synthesis; arc reactor; plasma jet; nanosilicon; lithium-ion battery; numerical modeling

INTRODUCTION

Rapid growth of sales of electrocars outlines the problem of increase of batteries manufacture. The most powerful source of autonomous electric supply is the batteries based on lithium-ion technologies. Theoretical boundaries of a battery efficiency are always limited by key components, i.e. anode, cathode, electrolyte and separator. Modern anode-electrodes of lithium-ion batteries (LIB) based on graphite materials have capacity around 372 mA·h/g. Theoretically replacement of the standard carbon anodes by silicon-based materials increases anode capacity almost by order to 3579 mA·h/g [1]. It is expected that in the nearest future the silicon anodes will lead to the most significant lithium-ion breakthrough, since graphite is a weak link in the battery, which takes more space than any other component. Appearance of silicon (Si) anodes of ultra high capacity, which can completely replace graphite, increases energy density of ion-lithium elements and can dramatically reduce cost of lithium-ion batteries, in particular in energy sector [2]. It is proved on practice that application of silicon instead of graphite as a negative electrode in the lithium batteries allows rising battery capacity as minimum in three times. The battery of the same size and weight could be able to provide several times more capacity or vice versa at the same capacity reduction of the battery size ensure several times. The main disadvantage of silicon is its swelling in saturation with lithium at recharging with concurrent increase of mechanical stresses in the volume of electrode layer, which promote loss of electric contact of active material with current supply and increase of corrosion. This results in low stability of cycling of electrodes. In order to increase the specific indices of power and capacity of LIB the main efforts of the researchers are directed on development of silicon nanomaterials [3]. In general silicon is one of the most perspective elements for the next generation of electrode materials in lithium-ion batteries due to its high theoretical specific power.

Up to the moment scientific community dramatically succeeded in development of silicon-containing anodes, which can provide significant improvement of energy density. The crucial moment is regulation of the volumetric expansion of silicon, i.e. necessity in nanoparticles application.

The most promising proposals in literature are related with application of nanostructuring in connection with the structures which can adjust to the change of volume during lithiumization such as yolk-shell or porous structures [4]. The final electrode materi-

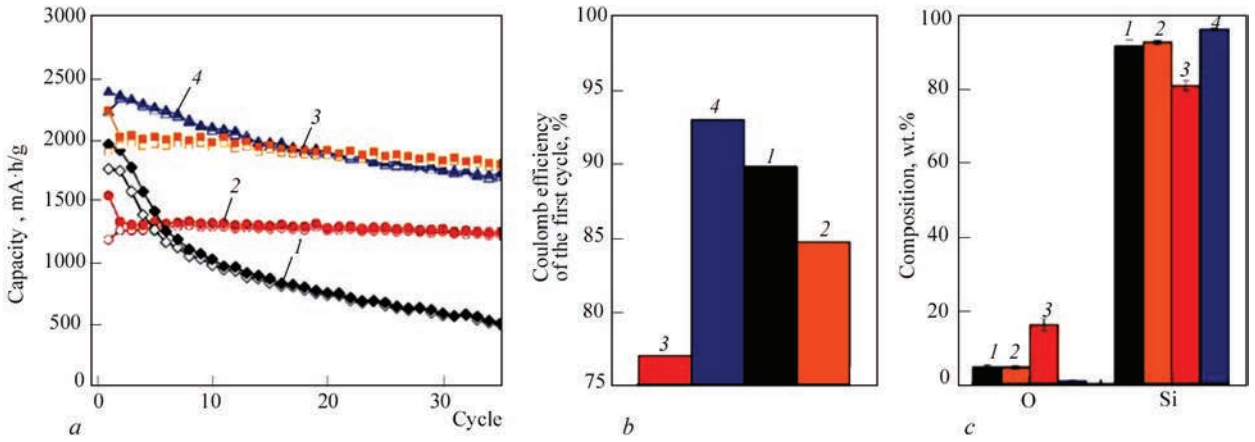

Figure 1. Characteristics of anode material for different commercially available companies (Tekna (*1*), Nano Amor (*2*), Sigma (*3*), GNM (*4*)) manufacturers of silicon nanoparticles [5]: *a* — comparison of stability during cycling between commercially available silicon nanoparticles; *b* — Coulomb efficiency of the first cycle for four considered powders; *c* — element analysis of tested commercially available powders

al consists of agglomerated silicon nanoparticles of 5 nm size, encapsulated inside hollow carbon structures of microsize. At that high specific capacity of the electrode is provided, namely 1570 mA·h/g, with preservation of 65 % capacity after 250 cycles of deep discharge.

The work [1] states that even at solution of the problem of optimum nanomaterials for LIB their commercialization is still not satisfactory because of two reasons. The first one is a complex and expensive methods of manufacture of nanomaterials, in particular of complex morphology. The second one is non-commercial standards, which are used for testing of novel nanostructures. Any proposed solutions finally have to stand commercialization test. For this it is necessary to take into account the issue of scaling at early stage of technology development. Cost and quality of silicon powders are the main problems, which require attention at further investigations. At that it is proposed to make more efforts in development of a system of nanoparticles manufacture, which can provide a set distribution by size as well as compatibility with processing scales, i.e. tones per year. Figure 1 shows characteristics of anode material for different currently commercially available companies–manufacturers of silicon nanoparticles.

For indices on Figure 1, *a* testing was carried out in the semi-centers with different output powders under similar conditions.

Nanopowders of elements and their inorganic compounds can be synthesized by different methods in gas-phase, liquid-phase and solid-phase processes that include physical and chemical deposition from gas phase (so called aerosol methods), solution deposition, mechanical chipping and others. Production of nanoparticles in thermal plasma of electric discharges (arc, high-frequency (HF) and ultra high frequency) is one of the leading directions of researches and developments on creation of basics of the new plasma technologies. Plasma-jet processes [6] are acceptable in all aspects for large-scale production of nanosilicon powders of different shape.

The silicon nanoparticles with carbon coating are considered as a perspective anode material for lithium-ion batteries of the next generation (Figure 2, *a*, *b*) [3]. At the same time development of economic and eco-friendly method of their high-efficient synthesis is still complicated that prevents practical realizing. Such investigations are important for deep understanding of the processes of plasma synthesis (Figure 2, *c*) and development of batteries with perfect characteristics [7].

It is believed that the technology of gas-phase plasma-chemical synthesis is of great potential for production of silicon nanoparticles. In comparison with other methods of synthesis the gas-phase plasma-chemical process has unique advantages. This is a one-stage production with possibility of high efficiency of synthesis with application of output material in any desirable shape (solid, liquid or gas phase). Besides, application of the plasma parameters provides regulation of material modification, product morphology and surface chemistry. Thus, these methods, when developed, can be considered a step ahead for promotion of large-scale production.

The problem of LIB development is determined in general [2]. As for technological peculiarities of plasma the work [8] provides a 3D modeling using a calculation method depending on time of plasma jet. It is shown that superposition of a uniform magnetic field due to Lorentz force and Joule heating promotes laminarization of flow, extension of plasma jet and temperature profile becomes more filled. This results in more effective heating of powder

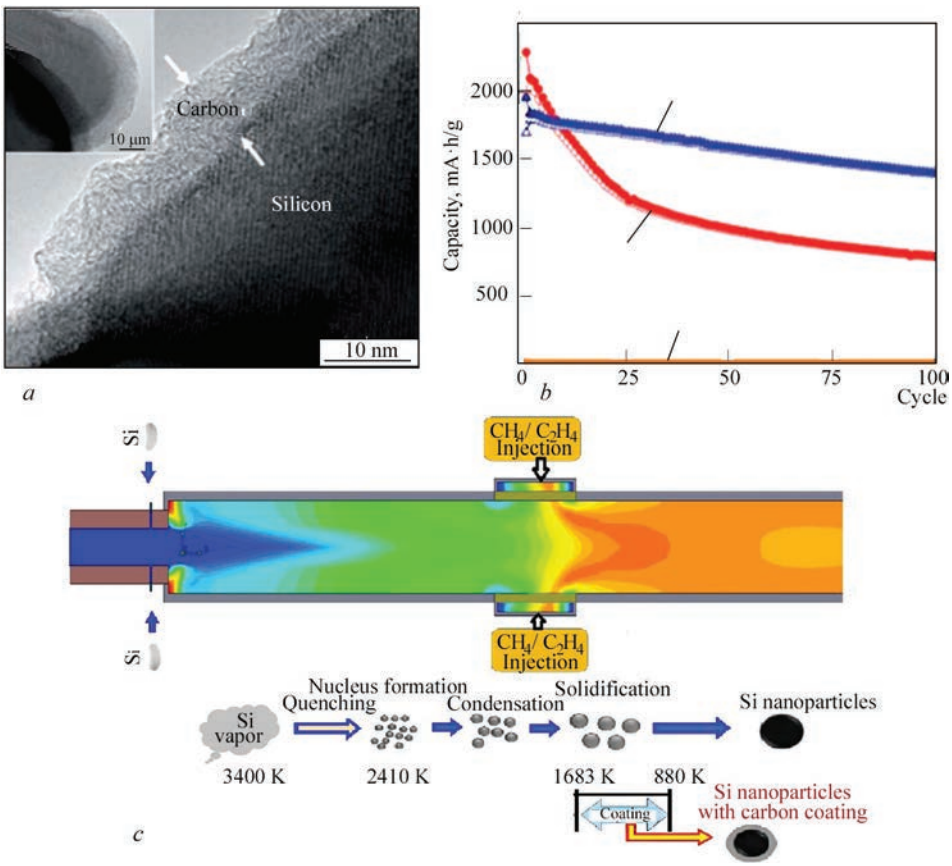

Figure 2. Properties and synthesis of nanosilicon particles with carbon coating produced in thermal plasma per one pass: *a* — TEM image of silicon nanoparticle in carbon coating; *b* — comparison of cyclic loss of LIB capacity with different silicon nanoparticles on anode (*1* — silicon nanoparticles; *2* — silicon nanoparticles with amorphous carbon; *3* — silicon nanoparticles with graphitized coating); *c* — process of obtaining of plasma synthesis of nanoparticles in carbon coating

particles and suppression of turbulent diffusion of silicon vapors and nanoparticles by vortexes that in turn affects their shape. In scope of the first task it is necessary to perform experimental check of efficiency of theoretically described phenomenon with application of hydrogen plasmatron of 30 [9] and 150 kW [10] power.

It is necessary to consider that without special measures deposition of the nanoparticles on a wall in a reactor will take place in the plasma process of production of nanopowders at gas-dispersed flow passing. Generation of a layer of sintered material results in overlaying of reactor section and complete violation of technological mode of the process [11].

The aim of the research is derived from the fact that there are problems to be solved on a way of creation of a large-scale production of nanosilicon for lithium-ion batteries.

AIM AND TASKS OF THE RESEARCH

The aim of this research lies in overcoming the issue of high productive manufacture of cheap silicon nanostructures for LIB including process scales. The next tasks are to be fulfilled in order to reach the set aim, namely increase the efficiency of evaporation/dissociation of a precursor material of silicon nanopowders in the area of high-temperature initial section of a plasma jet; provide the conditions for continuous removal of synthesized nanoparticles from a reactor working zone.

RESEARCH METHODS

In order to realize the tasks set there was developed a plasma reactor using electric arc plasmatron of linear scheme with application of argon-hydrogen mixture as a plasma-forming gas.

Using a system of electromagnet control the possibility is provided for change of magnetic induction by set law. The researches on effect of the magnetic field on the processes of formation and evaporation of a gas-powder flow in a plasma jet were carried out by means of determination of configuration, geometry sizes and structure of the initial jet section. The dispersed material is the silicon powder being fed to plasmatron nozzle section on a radial scheme.

A series of experiments using electric arc plasmatron on laboratory plasma units of 30 and 150 kW power (Figure 3) was carried out for analysis of the effect of external magnetic field on regulation of plasma jet parameters.

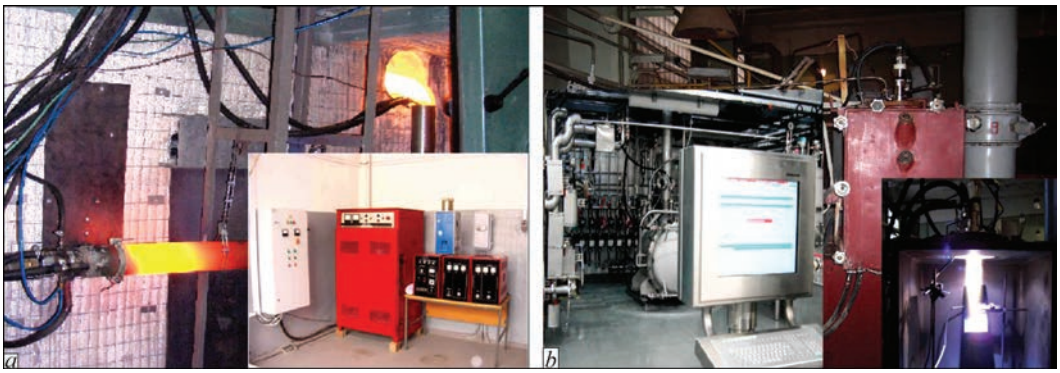

Figure 3. General view of the laboratory plasma units for nanosilicon synthesis of power, kW: *a* — 30; *b* — 150

Numerical modeling was used as a tool in designing the process and reactor for the nanopowders synthesis. It provided the information on temperature fields, velocities and concentrations.

RESEARCH RESULTS AND THEIR DISCUSSION

A series of the experiments using the electric arc linear scheme plasmatron [9] was carried out for detection of the effect of external magnetic field on regulation of the plasma jet parameters. The plasmatron is oriented on application of argon-hydrogen mixture as a plasma-forming gas. The electromagnet is fixed in relation to the plasmatron nozzle system in such a way that a part of arc column, its area with connection spot to the electrode, initial area of plasma-forming jet and nozzle part of arc channel were located in a zone of effect of magnetic field.

A value of magnetic induction is determined by the current value in a coil and can be changed by set law using the electromagnet regulation system. The result of directed orientation of the column part and arc end area is rebuilding of the temperature profile and velocities of plasma jet, which is formed in the nozzle part of arc channel. It is well represented on Figure 4, where appearance of the plasma jet with and without magnetic field at the same operation mode is shown.

Regulation of the parameters of plasma jet is particularly relevant on the stage of evaporation/dissociation of the precursor (in form of powder or gas) in the process of nanoparticles synthesis.

It is known that in general case the channels of transfer of gas and solid phases in two-phase flows of such type do not match. This results in coming of part of the material being processed in the area of relatively low temperatures and velocities of working medium. Instead the consequence of difference in the conditions of heating and acceleration of the particles is a decrease of a coefficient of raw material use. Correction of mutual position of phases of the two-phase flow will allow to some extent improving this index of the process efficiency. The investigations of effect of the magnetic field on the process of formation and evaporation of gas-powder flow in the plasma jet was carried out by means of determination of configuration, geometry and structure of the initial jet section. Dispersed material (silicon powder) was fed on the nozzle end section of plasmatron by radial scheme.

Electric power of the plasmatron is 30 and useful one is 22 kW. Consumption of the components of plasma-forming gas: $G_{Ar} = 3.3$; $G_{H_2} = 0.7$ m^3/h. Based on obtained estimations the specific efficiency of evaporation of 5–20 μm size particles of silicon powder in argon-hydrogen electric-arc plasma jet makes up to

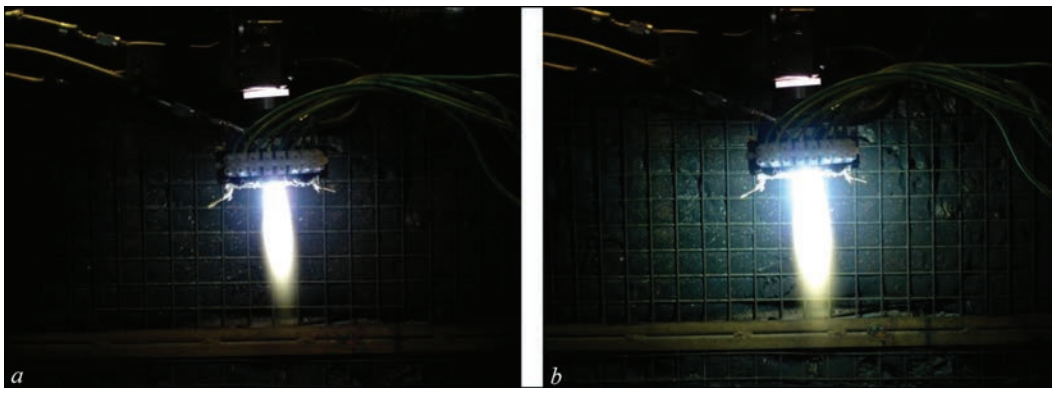

Figure 4. Appearance of plasma jet*: *a* — without external magnetic field; *b* — with external magnetic field

*Photo is provided by Dr. of Tech. Sci. Pashchenko V.M.

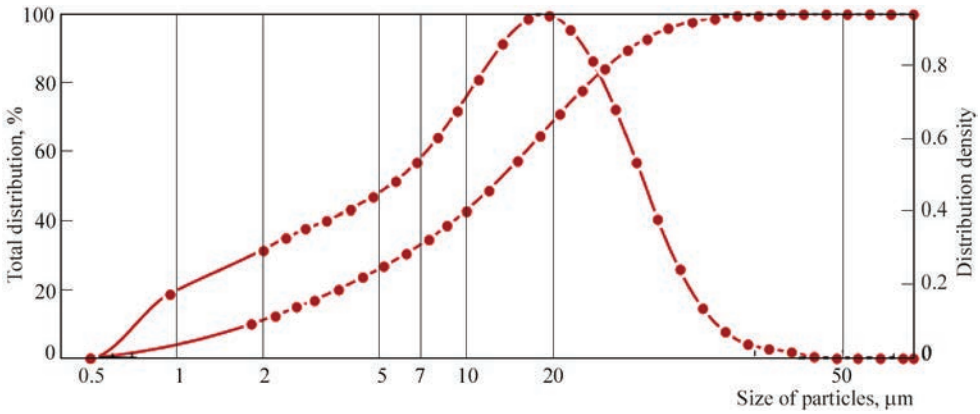

Figure 5. Size of the particles of raw silicon powder

10 kW per 1 kg. Silicon powder with consumption of G_{Si} = 2.0 kg/h (Figure 5) was used in the experiments. Consumption of a transporting gas argon was optimized for 2 kg/h efficiency for the purpose of blowing of the powder on the axis of plasma jet and it was kept constant. The final aim of the experiments was to provide stable evaporation of all powder without presence of tracks of melted particles shining at the output of initial section of the plasma jet (Figure 6).

Also the work was directed on the examination of two-phase flow, heat exchange and mass flow of nanoparticles, including on a wall of plasma reactor with limited jet flow in the processes of silicon nanopowders production. These dependencies are important for optimizing the technological parameters and design of the processes of plasma synthesis of nanopowders.

The reactor is a stationary working flow-through device at atmospheric pressure (Figure 7). It includes a zone of discharge of plasmatron of indirect action, assembly for raw material supply into a high-temperature flow, reactive volume, quenching device, imbedded heat-exchanger and filter for release of condensed products from gas-dispersed flow.

Current production methods of nanopowders of metallic silicon are expensive and make 30 000 US dollars per 1 kg. The most powerful unit (to 200 kW) Teknano-200 Plasma Nanopowder Synthesis of Canadian Company Tekna based on induction plasma technology with working gases (Ar, O_2, N_2, H_2, He and etc.) provides efficiency up to several kg/h of nanomaterials depending on their properties [12].

Following from this, the present work is an attempt to demonstrate the possibility of high-productive manufacture of nanosilicon for LIB from cheap and available raw material, namely silicon powder of metallurgical property with grain-size composition (Figure 5). The electric-arc reactor is made on traditional scheme (Figure 7). Issues of movement of dispersed phase, its heating, melting, evaporation and further condensing into nanoparticles in a plasma jet are sufficiently studied and have many years of history [6, 9, 11]. On practice realization of this condition lies in providing the sufficient time for staying of polydispersed powder flow in the high-temperature jet till complete evaporation. The reactor realizes the limited jet flow with abrupt channel expansion. A channel zone, located behind abrupt expansion (section of flow detachment and to section of flow attachment), is a zone of flow recirculation formed by vortexes. The vortexes are also formed in the plasmatron channel below the flow from powder input, which is transported by gas, into the plasma jet. These vortexes and the next turbulent dissipation down the flow are the most critical source of heat- and mass exchange of dusty plasma with the reactor walls. This as a result leads to deposition of the particles on the reactor walls and forced stop of the process. Removal of these phenomena will provide stable continuous work of the reactor.

Numerical modeling was used as a tool in design of the process and reactor for nanopowders synthesis. It provided the information on temperature fields, velocities and concentrations. Figure 8 shows typi-

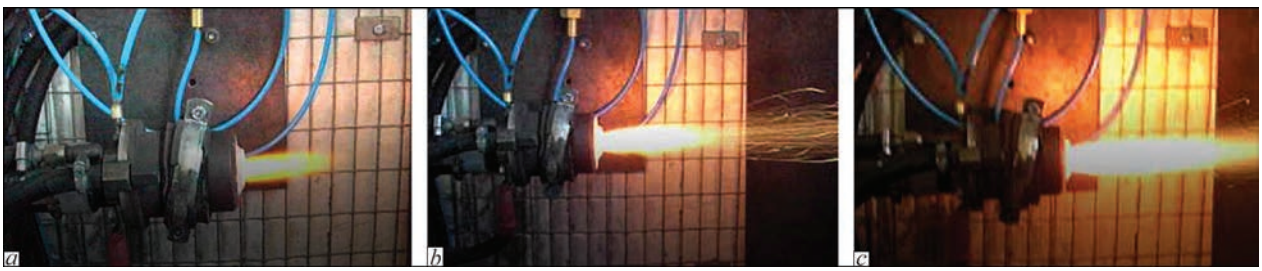

Figure 6. Appearance of plasma jet: *a* — at absence of powder feed without magnetic field; *b* — powder feed without magnetic field; *c* — powder feed with magnetic field

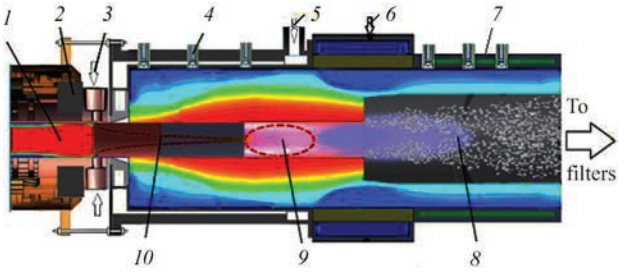

Figure 7. Electric arc reactor for plasma chemical synthesis of nanopowders: *1* — zone of attachment of arc anode spot; *2* — magnet; *3* — powder + transporting gas; *4* — heat flow and dust deposition probe; *5* — concurrent blow in, gas shield; *6* — granulating gas; *7* — water cooling; *8* — zone of nanoparticles growth; *9* — zone of powder particles evaporation; *10* — zone of heating and melting of powder particles

cal results of modeling of the plasma reactor in zone of powder injection into a flame jet and behind the abrupt channel expansion of outlet of plasmatron anode nozzle and reactor inlet.

Based on modeling results the protection was put for the wall in a zone of recirculation flow behind the abrupt channel expansion of reactor and behind quenching device from the effect of high-enthalpy two-phase flow using wall mounted gas shields. There is a twist of a peripheral flow in the reactor (Figure 7) or blowing in through porous wall. Down the flow efficiency of the shield is reduced, however, it should protect the surface of the reactor wall until the quenching device.

Based on preliminary estimations the specific efficiency for target product makes around 10 kW·h/kg, at which complete evaporation of the silicon powder in argon-hydrogen plasma jet is achieved. Using the plasmatron with electric power 150 kW (Figure 3, *b*)

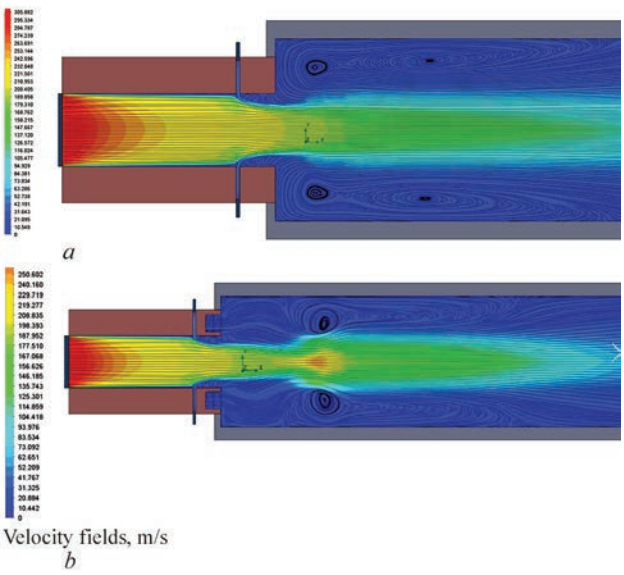

Figure 8. Vortex flows in nozzle channel of plasmatron anode behind the place of powder injection and abrupt expansion at reactor inlet: *a* — without shield; *b* — with gas shield through porous blow in

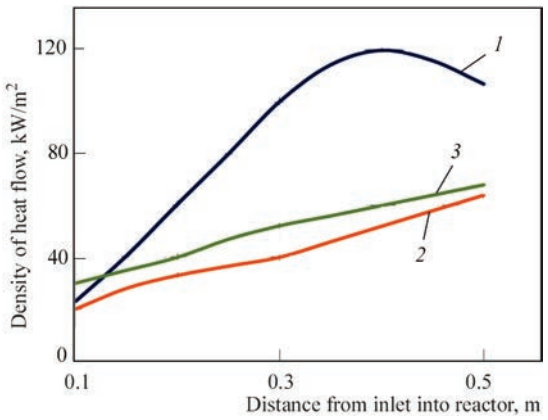

Figure 9. Distribution of density of heat flows on reactor wall under different working conditions: *1* — without gas shield; *2* — with gas shield; *3* — with gas shield and powder feed

and useful 100 kW the silicon powder was fed into the reactor through two injectors with 5 kg/h consumption (Figure 7). Diameter of the outlet nozzle of plasmatron anode made 20 mm. Plasma-forming gas is argon (75 %) + hydrogen (25 %) with 25 m^3/h consumption. Temperature of jet axis is 15000 K. Shielding gas is argon (75 %) + hydrogen (25 %) with 10 m^3/h consumption. Quenching gas is argon (75 %) + hydrogen (25 %) with 100 m^3/h consumption.

Inner reactor diameter is 200 mm, length of quenching device is 500 mm. Wall of the reactor is water-cooled with partial recuperative heat removal in shielding gas.

Formation of nanoparticles in the plasma reactors with limited jet flow takes place as a result of condensation from gas phase and usually accompanied by deposition of obtained nanoparticles on the reactor surfaces that limit high-temperature gas-dispersed flow. The issues of local heat and mass transfer in the plasma reactor are of high importance for performance of directed plasma synthesis of nanopowders with set properties. Due to this there was carried out

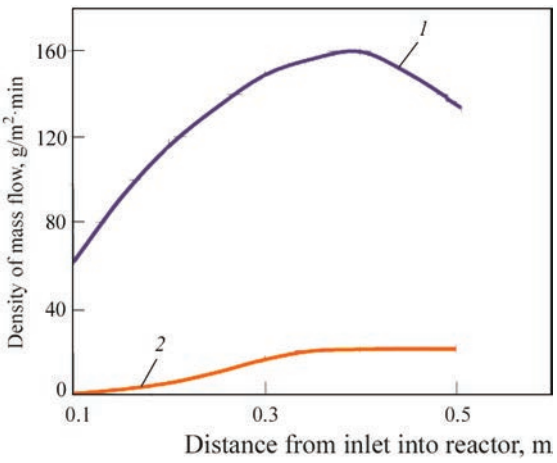

Figure 10. Distribution of density of mass flows on reactor wall in synthesis of silicon nanopowders: *1* — without gas shield; *2* — with gas shield

an experimental investigation of distribution of density of heat (Figure 9) and mass (Figure 10) flows of nanoparticles on the plasma reactor surface. Measurement of a value of heat flow on the reactor wall was carried out by means of registration of the values of loss of cooling water and variation of its temperature in the probes of heat flow installed on the reactor wall. The powder was collected separately from each probe and weighed after experiment for evaluation of distribution of density of mass flows on the reactor wall.

The first stage of the process is evaporation of the raw material at high temperature of high-enthalpy thermal arc plasma. Output particles of silicon move along the flow up to a tail of plasma jet, heat and evaporate. Temperature of plasma flow is quickly reduced transferring energy to the raw material. On the second stage a saturated vapor in the process of quenching undergoes homogeneous nucleation and heterogeneous condensation as a series of processes of nanoparticles production. Thermal arc plasma is a corresponding tool for silicon processing with its unique properties such as high conductivity in comparison with metallic materials, high latent heat of evaporation and high temperature of vapor formation. Besides, synthesis of silicon nanomaterials is affected by unique characteristics of electric arc plasma jet, namely sufficient heat emission from thermal plasma to silicon in the initial section and fast temperature drop beyond it that is favorable for the second stage of the process.

Phenomenon of extension of a high-temperature initial area of the plasma jet in longitudinal magnetic field was experimentally proved (see Figure 4). At that there is an improvement of heating of polydisperse phase with concurrent increase of efficiency and possibility of application of larger powder particles. Complete evaporation of such silicon raw material requires sufficiently long time of staying in a high-temperature zone. The external magnetic field suppresses turbulent vortexes and formation of coarser nanopowders is expected due to suppression of turbulent diffusion of silicon vapors and nanoparticles by the vortexes on the plasma periphery.

Distribution of density of heat flow along the reactor length is nonuniform. Without gas shield it has a maximum in the area of attachment of near-boundary layer of the jet to reactor wall. The value of heat flow density is determined by radiant and convective heat exchange and depends on plasma power. Distribution of heat flow density with gas shield and dusty flow is greatly varied.

Distribution density of mass flows on the reactor wall at silicon nanopowders synthesis without gas shield also has extreme nature with a maximum in the zone of attachment of near-boundary layer to the wall. Relative parts of mass flows on the reactor wall remained unchanged even at increase of duration of synthesis in the scope of up to 60 min under given consumption of the output raw material. Increase of thickness of deposited nanoparticles layer reduces heat flow on the reactor wall due to increase of layer thermal resistance. Moreover, increase of experiment duration to 60 min provides rise of the average size of nanoparticles, in particular in a zone of maximum heat flow.

A gas shield in a form of peripheral vortex flow was used for stabilizing the high-temperature zone of flow in the reactor (see Figure 7) and decrease of intensity of dissipation due to reduction of the turbulent pulsations of velocity (laminarization of flow) and, respectively, increase of time of reagents staying in this zone. Presence of the vortex flow created by swirler results in significant change of distribution of heat and mass flows to the reactor wall (Figures 9, 10) and decrease of their value. The results of the experiments show that creation of the peripheral vortex flow significantly change the characteristics of heat- and mass exchange in the reactor. It should be expected that optimizing can result in elimination of deposition of powder nanoparticles on the reactor wall and provide the conditions of continuous work.

CONCLUSIONS

1. An important result of the carried investigations is the experimental proof of the possibility of significant increase of efficiency of plasma-chemical reactor using electric-arc plasma. This was reached thanks to two conditions, namely possibility of maximum application of energy of plasma jet due to its laminarization in the magnetic field and multijet introduction of raw material; provision of nonequilibrium process when velocity of evaporation of the particles of source silicon in the plasma jet exceeds vapor diffusion with temperature equalizing. This provides efficiency of the process more than equilibrium.

The second important result of the investigation is positive application of the gas shield for provision of continuous process of synthesis of silicon nanoparticles.

2. The result of performed modeling and experimental check on the plasma units of 30 and 150 kW power showed that application of additional effects on the plasma jet by magnetic field at the outlet of nozzle-anode of the plasmatron and gas shield at the inlet of reactor provide complete evaporation of source silicon powder with specific energy consumption 10kW·h/kg.

3. Carried investigations showed that the vortex flow of gas shield results in significant change of distribution of heat and mass flows to the reactor wall

and 2 and 7 times decrease of their value in this performance, respectively. It is expected that optimizing can result in elimination of deposition of nanosilicon powder on the reactor wall and provide the conditions for continuous work.

Further development of the process based on this investigation should be performed in a direction of synthesis of nanosilicon particles with carbon coating in thermal plasma per one pass.

REFERENCES

1. Berdichevsky, G. (2020) The future of energy storage towards a perfect battery with global scale. September 2, 2020. https://www.silanano.com/uploads/Sila-_-The%-Future-of-Energy-Storage-White-Paper.pdf
2. Yuca, N., Taskin, O.S., Arici, E. (2020) An overview on efforts to enhance the Si electrode stability for lithium ion batteries. *Energy Storage*, 2(**1**). DOI: https://doi.org/10.1002/est2.94
3. Kuksenko, S.P., Tarasenko, Y.O., Kaleniuk, H.O., Kartel, M.T. (2020) Stable silicon electrodes with vinyliden fluoride polymer binder for lithium-ion batteries. *Khimiya, Fizyka ta Tekhnologiya Poverhni*, 11(**1**), 58–71 [in Ukrainian]. DOI: http://doi.org/10.15407/hftp11.01.058
4. Jaumann,T., Gerwig, M., Balach, J. et al. (2017) Dichlorosilane-derived nano-silicon inside hollow carbon spheres as a high-performance anode for Li-ion batteries. *J. of Materials Chemistry A*, **5**, 9262–9271. DOI: https://doi.org/10.1039/C7TA00188F
5. Schwan, J., Nava, G., Mangolini, L. (2020) Critical barriers to the large scale commercialization of silicon-containing batteries. *Nanoscale Adv.*, **2**, 4368–4389. DOI: https://doi.org/10.1039/D0NA00589D
6. Petrov, S.V. (2021) *Innovative plasma-spraying technologies*. LAMBERT Academic Publ. [in Russian].
7. Zhang, X., Wang, Y., Min, B. et al. (2021) A controllable and byproduct-free synthesis method of carbon-coated silicon nanoparticles by induction thermal plasma for lithium ion battery. *Advanced Powder Technology*, 32(**8**), 2828–2838. DOI: https://doi.org/10.1016/j.apt.2021.06.003.
8. Shigeta, M. (2018) Numerical study of axial magnetic effects on a turbulent thermal plasma jet for nanopowder production using 3D time-dependent simulation. *J. of Flow Control, Measurement & Visualization*, 6(**2**), 107–123. DOI: 10.4236/jfcmv.2018.62010
9. Petrov, S., Korzhyk, V. (2016) Plasma process of silicon production for photovoltaic power generation. *Engineering and Technology*, 3(**5**), 74–88.
10. Petrov, S.V. (2013) Plasmatron engineering. Stages of development. *Svarshchik*, 43(**3**), 26–31 [in Russian].
11. Astashov, A.G. (2016) *Distribution of density of heat and mass flows in plasma reactor with limited jet flow in process of producing nanopowders*. Moscow, IMET RAN [in Russian].
12. *Tekna Plasma Systems Inc*. http://tekna.com/

ORCID

S.V. Petrov: 0000-0003-0373-8003,
S.G. Bondarenko: 0000-0001-9590-4747,
Sato Koichi: 0000-0001-9590-4747

CONFLICT OF INTEREST

The Authors declare no conflict of interest

CORRESPONDING AUTHOR

S.V. Petrov
E.O. Paton Electric Welding Institute of the NASU
11 Kazymyr Malevych Str., 03150, Kyiv, Ukraine.
E-mail: svp_plazer@i.ua

SUGGESTED CITATION

S.V. Petrov, S.G. Bondarenko, Sato Koichi (2022) Plasma-chemical process of obtaining nanosilicon for lithium-ion batteries. *The Paton Welding J.*, **10**, 49–56.

JOURNAL HOME PAGE

https://pwj.com.ua/en

Received: 11.07.2022
Accepted: 01.12.2022